Dynamics and Model-Based Control of Electric Power Steering Systems

by

Naser Mehrabi

A thesis
presented to the University of Waterloo
in fulfillment of the
thesis requirement for the degree of
Doctor of Philosophy
in
Systems Design Engineering

Waterloo, Ontario, Canada, 2014

I hereby declare that I am the sole author of this thesis. This is a true copy of the thesis, including any required final revisions, as accepted by my examiners.

I understand that my thesis may be made electronically available to the public.

Abstract

Many automobile manufacturers are switching to Electric Power Steering (EPS) systems for their better performance and cost advantages over traditional Hydraulic Power Steering (HPS) systems. EPS compared to HPS offer lower energy consumption, lower total weight, and package flexibility at no cost penalty. Furthermore, since EPS systems can provide assistance to drivers independent of the vehicle driving conditions, new technologies can be implemented to improve the steering feel and safety, simultaneously.

In this thesis, a neuromusculoskeletal driver and a high-fidelity vehicle model are developed in MapleSim to provide realistic simulations to study the driver-vehicle interactions and EPS systems. The vehicle model consists of MacPherson and multilink suspensions at front and rear equipped with a column-type EPS system. The driver model is a fully neuromusculoskeletal model of a driver arm holding the steering wheel, controlled by the driver's central nervous system. A hierarchical approach is used to capture the complexity of the neuromuscular dynamics and the central nervous system in the coordination of the driver's upper extremity activities. The proposed motor control framework has three layers: the first layer, or the path-planning layer, plans a desired vehicle trajectory and the required steering angles to perform the desired trajectory, the second layer (or the force distribution controller) actuates the musculoskeletal arm, and the final layer is added to ensure the precision control and disturbance rejection of the motor control units.

The overall goal of this thesis is to study vehicle-driver interactions and to design a model-based EPS controller that considers the driver's characteristics. To design such an EPS controller, the high-fidelity driver-vehicle model is simplified to reduce the computational burden associated with the multibody and biomechanical systems. Then, four driver types are introduced based on the physical characteristics of drivers such as age and gender, and the corresponding parameters are incorporated in the model. Last but not least, a new model-based EPS controller is developed to provide appropriate assistance to each of the predefined driver types. To do this, the characteristic curves are tuned using a systematic optimization procedure to provide appropriate assistance to drivers with different physical strength, in order to have a similar road and steering feel. In this thesis,

it is recommended that muscle fatigue be used as a measure of steering feel. Then, based on the tuned EPS characteristic curves, an observer-based optimal disturbance rejection controller, consisting of a linear quadratic regulator controller and a Kalman filter observer augmented with a shaping filter, is developed to deliver the assistance while attenuating external disturbances. The results show that it is possible to develop a model-based EPS controller that is optimized for a given driver population.

Acknowledgments

I would like to express

My deep appreciation to my supervisor, Professor John McPhee for his continued support, valuable guidance, and the academic environment he provided during the course of research.

I would like to thank

My committee members, Dr. Jozsef Kovecses, Dr. Eihab Abdel-Rahman, Professor Steve Lambert, and Dr. Nasser Lashgarian Azad for their time to review and approve my thesis.

I am grateful to

My friends and colleagues at the Motion Research Group (MoRG) (Amir Taghavipour, Reza Sharif Razavian, Hadi Adibi Asl, Mohammad Sharif Shourijeh, Ramin Masoudi, Mahyar Vajedi, Maryeah Chehrehsaz, Borna Ghannadi, Andrew Hall, Adam Ing, Joydeep Banerjee, Dan Johnson, Valerie Norman-Gerum, Willem Petersen, Mike Boos, Aden Seaman, Shinhoon Kim and Tom Uchida) for providing a friendly and dynamic environment. I have had a great time working with you guys and hope that we keep in touch in the future.

Sincere thanks to

My sponsors, The Natural Sciences and Engineering Research Council of Canada (NSERC), Ontario Centres of Excellence (OCE), Toyota, and Maplesoft Company for their financial supports. The financial support from these organizations allowed me to focus on my research.

Finally and most importantly, I would like to acknowledge

My parents, Abolghasem Mehrabi and Shahla Hamrahi, for the unlimited love and support you provided me throughout all these years. Without your unconditional support, encouragement, understanding, and care, I would not have made it so far.

Thank You

Naser Mehrabi
August 2014

Table of Contents

List of Tables

List of Figures

1

Introduction

Realistic driver models and computer simulations can play an important role in designing and improving driver-assistance technologies by reducing cost and time associated with vehicle development. A realistic driver model that provides path planning predictions mimics the reality, because the the physiological limitations and attributes of a human driver have been considered. The overall goal of this research is to develop an integrated driver and vehicle model to study driver-vehicle interactions and to design an Electric Power Steering (EPS) system that considers a driver's physical characteristics. With the introduction of driver-assistance technologies such as torque or angle overlay systems, a capable driver model is required to study the performance of these technologies. In this thesis, this model is used to design and evaluate an Electric Power Steering controller that can account for a driver's physical characteristics and preferences.

1.1 Background

The steering system is an essential part of a vehicle, because not only does it steer the vehicle but it also conveys information about the road and vehicle to the driver. The well-established front-wheel drive preference results in a high weight concentration over the steered wheels, which significantly increases the effort to turn the steering wheel manually. Automobile manufacturers introduced power steering systems to reduce the physical effort of drivers. Based on the power source, these systems are divided into two categories: hydraulic and electric power steering systems. A Hydraulic Power Steering (HPS) system uses hydraulic pressure supplied from an engine driven pump to assist drives to turn the steering wheel. On the other hand, an Electric Power Steering (EPS) system generates steering assistance using an electric motor to make steering more comfortable for drivers. EPS systems compared to HPS systems offer lower energy consumption, lower total weight and package flexibility, at no cost penalty. In addition, with the increase of fuel prices, the fuel saving benefits of EPS systems make these products more economical than HPS systems. Consequently, it is expected that the share of EPS in the steering market will significantly grow, especially in small and medium sized vehicles [9]. Furthermore, EPS systems can generate assistance independent of the vehicle driving condition; therefore, new control strategies can be implemented to improve the steering feel and safety of the vehicle, simultaneously.

1.2 Motivations

When a vehicle is steered, a friction force is produced at the contact patch between the tire and road. This friction force is transferred back through the steering linkages to the steering wheel and produces a resistive torque that opposes the driver's steering input. Power steering systems are used to decrease this resistive torque to reduce the physical effort of drivers and to provide good steering feel. However, the term "good" is very subjective and is a function of many parameters such as the steering assist mechanism and the driver's characteristics and physical ability.

Currently, vehicle manufacturing companies use professional drivers to tune EPS systems to provide good steering feel. This group of drivers should represent all drivers with different physical characteristics and abilities. Drivers may have different steering stiffness and sensitivity preferences. Therefore, developing a unique and universal steering system that is tuned for all drivers at the same time seems impossible. A driver's characteristics and physical ability significantly affect that driver's desired steering feel. For example, an older driver with weaker muscles requires more assistance in steering than a young driver with stronger muscles. The young driver may prefer a more sporty steering setting and has stronger muscles to overcome the resistive torque. On the other hand, since EPS systems can generate assist torque independent of the vehicle driving condition, they can easily be programmed to implement sophisticated assist algorithms, or modify the control parameters at any time. Therefore, different assistance algorithms can be used to improve the steering feel based on the drivers' preference and physical characteristics.

Most of the literature on EPS control design is focused on the control structure design. In addition to the control structure, systematic studies on the control objectives such as steering feel and comfort are still needed for better understanding of driver-assist technologies. However, to the best of the author's knowledge, no research has been done on the systematic design of an EPS system that accounts for the physical abilities and characteristics of drivers.

A recent direction of driver-assist technologies has been development of a realistic driver model to be used in designing new technologies to aid drivers in their driving tasks. For example, an integrated driver-vehicle model can be conveniently used to design and evaluate driver-assist systems such as EPS. A suitable driver-vehicle simulation interface should consider the neuromuscular dynamics, physical capabilities and limitations of the driver. A human driver can be modeled as an adaptive feedback controller with various proprioceptive measurements, as shown in Fig. 1.1. Drivers use visual feedback to correct/plan the trajectory of the vehicle, and at the same time, they use the somatosensory/proprioceptive measurements to control the steering wheel position while the information from the kinaesthetic sensory system is used to adapt to different steering conditions. The human neuromuscular system, including the Central Nervous System (CNS) and Stabilizer, can

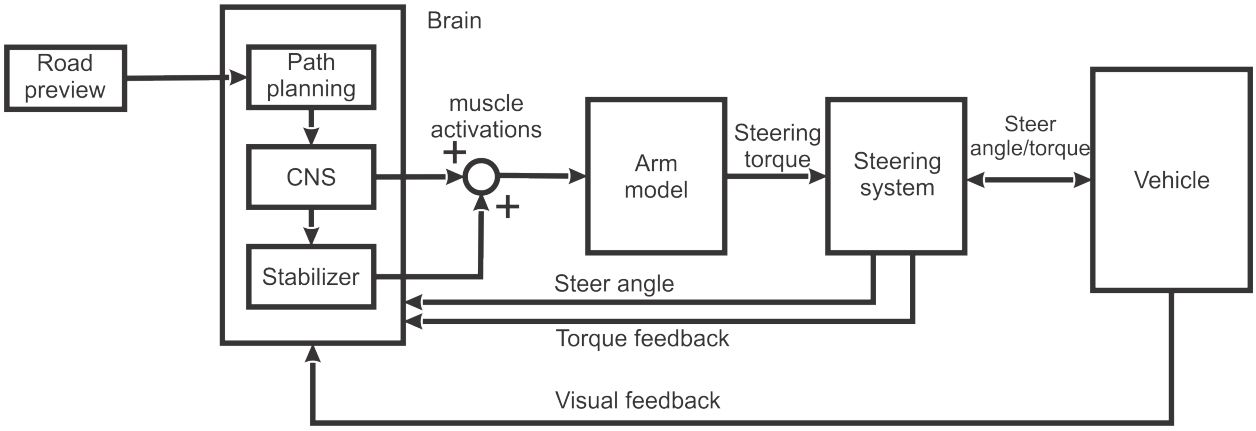

Figure 1.1: Neuromusculoskeletal structure of a driver

describe the driver's response and physical limits to the steering wheel force feedback by considering the muscle dynamics and reflexive response to the change in force and displacement.

The natural flow of human motion starts from the motor-neuron spikes, leading to the production of muscle twitches and finally a force pulling the bones to reach a desired position. A forward dynamics approach can properly capture this neuromuscular dynamics, since it also follows the same natural flow. Equations of motion are integrated forward in time to obtain the motion trajectories in response to neuromuscular inputs. In contrast, an inverse dynamics approach uses the information in the opposite direction; the measured joint trajectories/limb motion and external loads are the inputs and the joint torques are the outputs. While an inverse dynamics approach is useful for clinical decision making, it cannot explain the underlying cause-and-effect relationships between motor neuron-spikes and system kinematics and what-if simulations. Therefore, muscle-actuated forward dynamic simulations can be used to predict each muscle contribution on a specific movement.

In this research, a high-fidelity driver model is developed which includes a brain model in conjunction with a neuromusculoskeletal model of driver's arm. This model is human-centered, meaning that the physical capabilities, limitations and preferences of the driver were taken into account in the design process, which then can be used to tune steering

controllers for a specific driver or the general population. Developing a simple model which can quantify objective criteria such as feel and comfort for different types of people can be a breakthrough in future steering developments. This approach reduces the time and cost associated with the preliminary design of experiments, and at the same time reduces the human (professional drivers) error on the evaluation of steering systems. In this approach, the EPS system can be easily tuned based on a desired steering preference, or for a population with a similar physical characteristics and ability.

1.3 Challenges

There are some serious challenges in the development of an integrated driver-vehicle model and dynamical modeling and control of electric power steering systems:

1. Development of a realistic simulation environment to study EPS systems is very challenging. Vehicle and driver models, as two essential components in the steering simulation, should be developed together and in detail to provide a clear understanding of the plant behavior before the design process for the controller begins.

2. Performance criteria in EPS systems, such as driver comfort and feel, are subjective matters because they vary according to drivers and driving conditions. Although recent research and experimental work described a number of guidelines to satisfy such criteria, a standard solution has not been ratified yet.

3. The EPS system is a system in which humans and machines interact directly; from the safety perspective, the control system must be stable and robust. Closed-loop stability must be maintained in the presence of nonlinearities such as Coulomb friction and parameter variations in the various mechanical sub-systems.

4. Driver models of varying degrees of complexity have been developed over the last half century. A significant proportion of these models have focused solely on brain modeling for tracking the desired path (autonomous driving). However, the neuromuscular

system contributes to task performance, disturbance rejection, and metabolic energy consumption, all of which influence motor control behavior of muscles, and should be considered in the design process.

5. In the forward dynamic simulation, both modeling and control aspects should be carefully considered. The modeling aspect covers the dynamic representation of the limb geometry and inertia, joint kinematics and muscle force origins and insertions, and the control aspect covers the central nervous system responsibility to coordinate the human limbs.

A suitable integrated driver-vehicle model assists engineers to overcome these challenges, and guide them in the right direction. In this thesis, we use the naturally predictive forward dynamics approach to predict subject-specific simulations of human arm movements. As an application of this model, an EPS controller is designed which considers the driver preference for the stiffness level of the steering wheel.

1.4 Thesis Organization

Chapter two begins with a literature review of electric power steering systems addressing modeling challenges. A literature review on driver modeling and the interaction between driver and vehicle is presented, and finally the different control strategies of EPS systems are discussed. Chapter three presents the development of a high-fidelity vehicle model including a column-assist EPS system as well as two simplified model of vehicle, internal model and control-oriented model, which then will be used in the neuromusculoskeletal control of driver's arm and design of EPS controller, respectively. Chapter four elaborates on a high-fidelity driver model with three-dimensional musculoskeletal arm model as well as a two-dimensional arm model. The high-fidelity model will be used to verify the two-dimensional model and evaluate the proposed EPS controller. In chapter five, the architecture and principle of EPS is introduced in detail. EPS characteristic curves are tuned for four groups of people and implemented in a new optimal disturbance rejection

controller. This EPS controller is based on the model-based stochastic optimal control, and satisfies the assistance, driver feel, and road feel criteria. Last but not least, simulations to evaluate the proposed controller on the high-fidelity driver model is performed and effectiveness of the controller are presented. Conclusions are made in chapter seven and the directions of future work are drawn.

2

Literature Review

In this chapter, a review of the relevant published research studies on the driver and vehicle interaction is presented. This review is classified into three sections: vehicle dynamical modeling by looking at power steering, driver modeling, and Electric Power Steering (EPS) system design. The combination of the aforementioned sections are required to build a concrete background to study the interaction between the driver and steering system with tendency to design and develop new driver-assist steering technologies.

In the dynamical modeling category, different models of the vehicle and power steering with various levels of complexity are introduced and some examples for each level are presented. Then, different approaches to driver modeling are introduced, and application of the optimal control theory in the path-following controller as the supervisory/vision-

based part of the driver model is explained. Furthermore, neuromusculoskeletal (NMS) features, classified into stretch reflex and muscle intrinsic stiffness/co-contraction, and the relevant publications are presented.

Research and developments in power steering systems can be divided into two categories: control objectives and control strategies. In this thesis, control objectives are classified into assistance, and road feel; each category is briefly introduced and some examples for each category are presented. Finally, EPS control strategies including classical and model-based control strategies, along with their advantages and disadvantages are discussed.

2.1 Vehicle Modeling

The first step in the design process of a controller is to understand the dynamics of the plant. A detailed high-fidelity dynamical model of a system can give in-depth insight into the system behavior. A high-fidelity model not only can be used to study the system's dynamics, but can also be used as a real plant to validate the designed controller. However, the high-fidelity model requires significant computational time in comparison to a simplified reduced-order model. Literature shows that there are many research studies on modeling different power steering systems with various levels of complexity for both hydraulic and electric power steering systems.

Liao et al. [77] developed a high-fidelity multibody dynamic model of vehicle including a column-assist EPS in *ADAMS*[1]. The full vehicle model has demonstrated good correlation with experimental results. This model has 347 degrees of freedom and includes non-linear elastic elements (bushing) in front and rear suspensions. Lower-order models also exist which consider a steering model with a simplified vehicle model (such as a lumped spring and damper [140] or a bicycle model of vehicle [166]). Badaway [8] developed a high-order model of a column-assisted EPS system, then a model reduction method is used to develop

[1]ADAMS is a registered trademark of MSC. Software

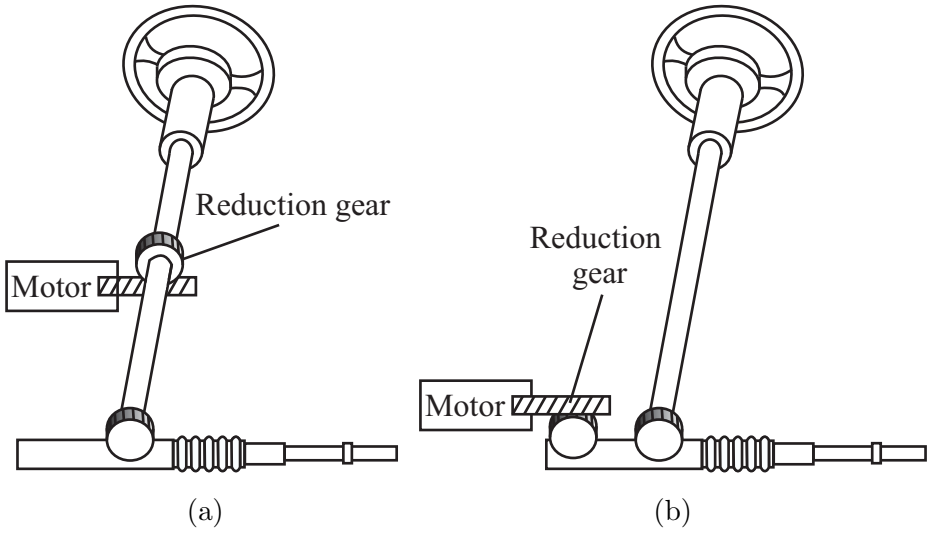

Figure 2.1: Types of Electric Power Steering (EPS) systems (a) Column-assist, (b) Rack-assist

a reduced-order model such that important dynamic distinctions such as stability, torque performance, disturbance rejections, and road feel are preserved.

Mohammadi and Kazemi [52] introduced the different types of EPS systems, and investigated the effect of assistance torque location on the performance of the EPS. The authors demonstrated that changing the location of the applied assist torque from the steering wheel to the wheels improves the steering sensitivity and efficiency. Other articles [33, 143] studied the possibility of using different electric actuators such as DC and AC motors in EPS systems. Tsuji et al. [143] investigated the effect of the EPS system on battery voltage and current.

Analyses of the stability of EPS systems have been reported for several types of EPS products. A stability condition for a double-pinion EPS is derived by Zaremba and Davis [163]. The authors derived an analytical approximation of the stability boundary condition, which gives the maximum assist torque that can be generated by the EPS system, while the closed-loop system is stable.

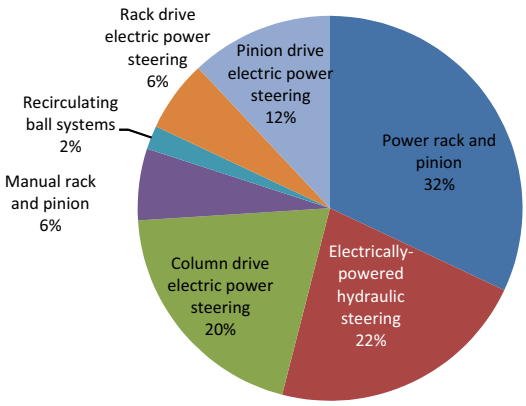

Figure 2.2: Proportion of EPS steering systems fitted to passenger cars and light trucks, divided by product type, Europe 2008 (% of volume)[9]

2.2 Types of Electric Power Steering (EPS) Systems

EPS systems can be categorized into different types depending on the location of the electric motor in the steering system as shown in Fig. 2.1. The most popular types of EPS systems are:

1. Column-assist type: the assist motor is attached to the steering column.
2. Pinion-assist type: the assist motor is attached to the steering gear's pinion shaft.
3. Rack-assist type: the assist motor is attached directly to the steering rack forming a single package.
4. Double pinion-assist type: the assist motor is attached to the steering rack via a separate pinion gear assembly.

Electric power steering systems were first used in mini-sized vehicles in 1988. Subsequent development of new electric motors with higher output power made it feasible for car manufacturers to equip bigger cars such as SUVs with EPS products. In 2004, the share of EPS in the steering market in Europe was 45%, and was predicted to reach 63%

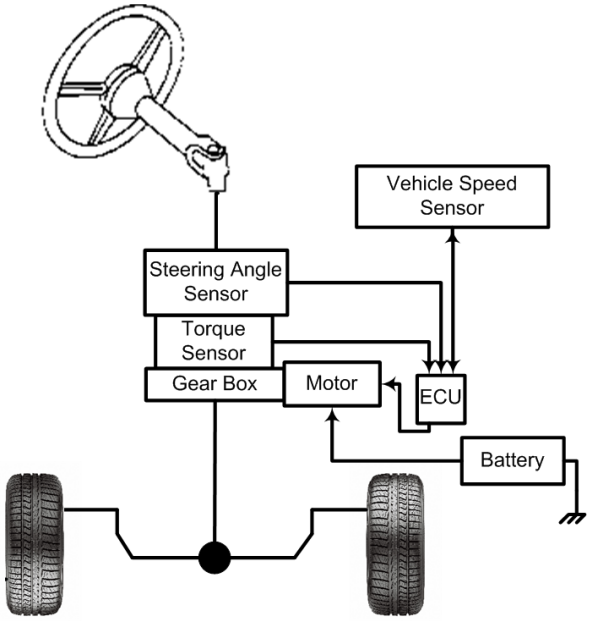

Figure 2.3: Architecture of a column-type EPS system

of the steering market by 2009 [9]. Fig. 2.2 shows the forecast of the global market trend of steering systems.

An EPS system typically consists of a vehicle speed sensor, a torque sensor, a steering angle sensor, an Electronic Control Unit (ECU) and a motor as shown in Fig. 2.3. When a vehicle with an EPS system turns, the column torque (measured by the torque sensor) and the steering angle are detected and sent to the ECU. The ECU defines target motor current based on the pre-established characteristic curves (see Chapter 5), steering direction, and vehicle speed. Then, it regulates the voltage of the electric motor to produce a desired current. A gear is used to decrease the motor speed to amplify the assist torque, and finally the loop is closed by applying the magnified torque to the steering column.

2.3 Driver Modeling

To reduce the design and development time of new automotive products, especially the parts that interact with drivers such as steering, a reliable driver model is required. Hence, understanding and anticipating the driver behavior has attracted many researchers from different disciplines. Driver models, based on their distinctive demands and applications, can be divided into vehicle-based and human-based driver models. The major concern of a vehicle-based driver model is the design and tuning of the vehicle components; it finds the required steering angle/torque to perform a given maneuver, but it does not consider how this torque is produced, or if the produced torque is physiologically possible. In contrast, a human-based driver model is focused on the understanding of the driver's limitation and preferences. Such a model essentially requires a path-following controller (similar to vehicle-based driver), along with a neuromusculoskeletal (NMS) model of the driver.

The following sections review the required tools to develop a human-based driver model, i.e. path-following controller and driver's neuromusculoskeletal system.

2.4 Path-following Controller

A path-following controller usually uses a mathematical expression of the vehicle dynamics and a control logic, and navigates the vehicle in a desired trajectory by manipulating the steering wheel, brake and throttle pedals. However, the scope of this research is limited to navigating only with the use of steering wheel. This group can be classified under two subcategories based on their objectives: compensatory control and preview (pursuit) control.

2.4.1 Compensatory Control

Driver models in this subcategory are closed-loop feedback controllers that follow a desired trajectory. The output of these controllers is usually the steering wheel angle, and the

input is the desired trajectory, while feedback information such as lateral displacement of the vehicle in local or global coordinates, heading angles, etc. are provided for corrections. There is no preview information provided to these controllers. These models can be appropriately used in the compensatory steering task. For example, when the driver is driving in the straight line, and an unknown disturbance such as side wind or road irregularity acts on the vehicle, the compensatory driver model compensates for the disturbance and heads back to the desired path.

The most famous compensatory driver model is the Crossover driver model [150] that considers human adaptive behavior. McRuer suggests that a human operator interacting with a physical device form a closed-loop compensatory control to the visually perceived errors. The experiments on different devices show that the response of a human driver can be fitted in the following transfer function:

$$G = K_P \frac{T_L j\omega + 1}{T_I j\omega + 1} e^{-j\omega(\tau + T_N)} \tag{2.1}$$

where τ and T_N are the cognitive and neuromuscular time delays, respectively, and K_P, T_L and T_I are the three parameters that operator adjust to ensure the stability of the closed-loop system.

Crossover models were first developed for pilot-aircraft systems, but in 1960 the idea was applied to driver-vehicle systems as well. A single loop feedback on the lateral position of the vehicle showed poor performance and low bandwidth. Therefore, a multi-loop feedback was developed in [150] to improve the vehicle response. In this model, an outer-loop on the lateral displacement of vehicle is enhanced by an inner loop on the heading angle to improve vehicle stability.

2.4.2 Preview (Pursuit) Control

Human drivers plan proper steering actions by considering the path ahead of the vehicle and their prediction on the vehicle response. For example, in an obstacle avoidance maneuver, the driver begins to steer before hitting the obstacle! Therefore, in this case, the crossover

models are not suitable, since they do not consider the predictive ability of human drivers.

Kondo in 1953 [70] presented a driver model which steers the vehicle in such a way that a predicted vehicle's position at a certain distance ahead of the vehicle coincides with the previewed path at that point. Kondo model [69], inspired by riding a bicycle in narrow roads, is used to counterbalance for external disturbances, such as wind, to maintain the steering wheel at the desired position. Later, McRuer and Weir [150] adopted a similar approach to Kondo's approach for pursuit component of their general STI (Systems Technology Inc.) driver model. The STI driver model consists of precognitive, compensatory, and pursuit control of crossover model with a single preview point.

With advances in optimal control theories, multi-point preview control has received more attention. Optimal control theory is widely used in path-following driver models. For example, MacAdam in 1981 [83] utilized an Linear Quadratic Regulator (LQR) control strategy with a prediction horizon to calculate the steering angle based on the previewed path information and predicted vehicle path. The driver time lag associated with neuromuscular and cognition delays have been added to the vehicle model, but not in the controller. Later, he added heading angle error compensation to the controller to take advantage of this model on curved roads [84].

Peng and Tomizuka [110] extended MacAdam's work and assumed that the road lateral curvature and elevation information is perfectly known in a certain preview horizon, and after that only statistical information is available. The authors also added the lateral acceleration as a ride comfort criteria to the objective function. The resultant optimal control has two preview parts, one corresponding to the known previewed horizon, and the other corresponding to the road ahead of the previewed section, which is represented by an exponential decay.

Casanova's driver model [130] uses the linear discrete-time preview (DLQRP) control approach; the authors, based on the fact that in DLQRP each element of the preview gain only affects the corresponding preview error element in the sequence, defined eight unevenly distributed preview points ahead of the driver with a smooth and decaying gain sequence. The tire saturation has been considered in the gain selecting process, and therefore, this

model has good performance in the near-limit conditions. A formal formulation of DLQRP with infinite prediction horizon and a random road disturbance has been derived by Sharp and Valtetsiotis [131]. The authors show the preview gains will converge to zero and become negligible when the full preview is presumed, and concluded that the driver model with 1 to 1.5 seconds preview can perform at full performance for slow speeds; this period should be increased for higher speeds.

Drivers use a representation of the vehicle response to steering input, a so-called path-following controller's internal model, to predict the vehicle path. An on-line parameter identification approach is used in [145] to identify the linear internal model dynamics in a rich excitation period and to make the control suitable for a longer range of operating conditions.

In [23], the model predictive control (MPC) approach is applied to the driver-steering system. The authors have shown that similar gains to LQR with infinite preview horizon can be found from the unconstrained MPC controller when they have similar objective functions. In this case, the MPC has the same length of prediction and control horizon and they are sufficient for full preview. Cole et al. in [23] compared the predictive (unconstrained MPC), receding horizon linear quadratic (LQ) and infinite-horizon LQ (LQR) methods of path-following controller. They showed that all controllers are identical when there are long enough preview and control horizons, and discussed the differences with different combination of prediction and control horizons. For the special case of long prediction horizon and short control horizon (single interval control horizon with 0.02 s) the predictive controller is the equivalent of the MacAdam [84] controller.

An MPC with multiple internal models has been developed in [63, 64] to replicate a highly skilled driver, who has knowledge of the vehicle nonlinearities such as tire saturations, to cover the entire range of vehicle dynamics. In this approach, a linear dynamical model of driver neuromuscular system and non-linear tire models are used to develop the internal model. Then, this model is linearized at evenly spaced linearization points, to form a family of linearized internal models.

2.5 Neuromusculoskeletal Dynamics

Computer simulations of biomechanical systems can provide in-depth insight about the system's dynamics, which then enables researchers to develop new human-based designs.

The majority of research on driver modeling is concentrated only on the driver as a path-following controller, as discussed above. However, a minority of research papers have followed a different approach and focused on the human neuromusculoskeletal (NMS) system, which gives insight into task performance, and driver's preferences and limitations. The NMS system is a complex system including chemical, electrical and mechanical components. Skeletal muscles involve all aforementioned components; moreover, the activation dynamics are an electrochemical process where the contraction dynamics is a highly nonlinear procedure.

Driver models with the NMS representation of the human enable a force interface between the driver and vehicle, and it can be used to develop driver assistance systems such as the haptic gas pedal, lane keeping, and artificial steering wheel torque feedback. The developments in these areas have shown promising results [2]. In the future, a steering system can be developed to identify the driver characteristics and environment conditions in real-time and change the steering system parameters accordingly.

2.5.1 Muscle Indeterminacy Problem

The control aspect of the NMS system manages the muscle force magnitudes, replicating the role of the motor control system in the Central Nervous System (CNS). The CNS receives information from the sensory organs and coordinates the motion of all body parts. The well-known indeterminacy of muscle force distribution and the nonlinearity of the system itself results in a challenging coordination problem. The indeterminacy refers to the number of muscles wrapping around a joint exceeding the number of degrees of freedom (DoF) of that joint, which can result in infinite muscle force patterns for a desired trajectory. However, it is observed that humans tend to produce similar activation patterns for

similar tasks [146]. In this thesis, it is assumed that the CNS controls the human movements in such a way that a psychologically motivated exertion is minimized. A driver's arm is an example of an indeterminate NMS system; therefore, it requires an extra criterion to reach a unique solution, where the exertion could be quantified as metabolic energy [144], or muscle fatigue [26, 6].

The minimization procedure can be performed in two ways. It can be carried out over the whole period of the simulation in a forward dynamic simulation setup (the so called Dynamic Optimization (DO) method). The common way of performing DO is to discretize the control inputs over time and search the acceptable space to find the optimal control sequence [28, 159, 105, 62, 6]. The other approach is an inverse dynamic approach or the so-called Static Optimization (SO) method [5]; in this approach the optimization is carried out at each time step independent of time history. The SO approach takes advantage of known joint trajectories and external loads to scale down the optimization problem. In the SO approach, the number of unknown variables is reduced to the number of muscles; they are not function of time, which results in shorter simulation time. However, the accuracy of this method heavily depends on experimental or desired trajectories. Furthermore, the time-independent nature of SO makes it difficult to incorporate time-dependent physiological performance criterion such as metabolic energy consumption [5]. Moreover, since the values predicted by SO at an instance are independent of the previous step, SO can result in unphysiological sharp discontinuities in the prediction of control signals; in other words SO is memory-less [28]. On the other hand, time-dependent objective functions can be easily included in DO, and the objective can be formulated independent of experimental/desired trajectories, and only is a function of final position. However, DO typically requires thousands of integrations of model states to converge to a unique solution [5, 104], which then results in very long simulation times.

Alternatively, the DO optimization can be performed at a shorter horizon instead of full period in a receding horizon approach. A nonlinear model predictive control (NMPC) can be used to suit this idea. Forward static optimization (FSO) is the special case of this approach with a single-step prediction and control horizon [129]. Depending on the prediction horizon length of NMPC, the results can be as reliable as DO simulations or

the simulation time can be as fast as SO simulations. Therefore, this method can manage the trade-off between the simulation time and accuracy. NMPC, by considering a proper prediction horizon, can use a more appropriate physiological cost function such as fatigue or metabolic energy consumption in the optimization, which can lead to more realistic simulation results.

Three other approaches have been developed to use the benefits of SO in reducing the computational loads demanded by DO approaches. Yamaguchi used a pseudo-inverse method to find muscle forces to track the desired joint acceleration [158]. This method does not consider dynamic properties of muscle and requires a specific optimization approach. Thelen et al. developed the Computed Muscle Control (CMC) method [139], considering a feedforward and feedback control to track the desired kinematics which should be known (i.e. not a predictive simulation). The feedforward controller computes the steady state value of muscle activation, and the feedback controller find the muscle excitation to track the steady-state muscle activation. However, CMC cannot account for muscle activation delay and muscle-tendon contraction dynamics, and may require residual forces to find a unique solution. Later, the authors modified the CMC approach [138] to explicitly account for the delays between muscle excitation and active force production.

2.5.2 Mechanical Dynamics of Muscle

Many dynamical muscle models are developed to describe different aspects of human muscles and to describe why a human muscle behaves in a particular way. In this thesis, a dynamical model is defined as the relation between the neural activation and the resulting muscle force/length. There are two well-known approaches for muscle modeling: the Hill-type muscle model [51] explains the muscle behavior at a macroscopic level, and is based on empirical relations; on the other hand, the cross-bridge (Huxley) [55] model can explain the microscopic behavior of the muscle. In this thesis, a simplified Hill-type muscle has been used to simulate the muscle dynamics. Since the Hill muscle model is based on empirical relations, it is computationally less demanding than Huxley's molecular approach, and is computationally manageable for a system with several muscles. Furthermore, the Hill

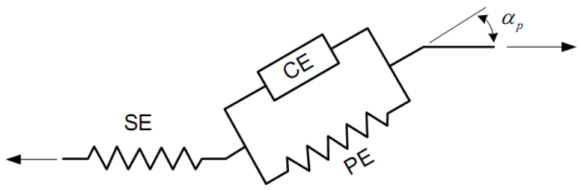

Figure 2.4: Schematic of Hill-type muscle model [51]

muscle model parameters can be easily adjusted to represent the age and gender-related changes in muscle mechanical properties.

The three-element Hill-type muscle model as shown in Fig. 2.4 consists of a large sarcomere[2] (Contractile Element, CE), with some additional visco-elastic properties to contribute for the tendon and aponeurosis (series element, SE) and connective tissues epimysium, perimysium and endomysium (parallel element, PE). However, the mathematical representation of this model results in stiff ordinary differential equation. Therefore, different versions of this muscle model are used in the literature to overcome this issue. For example, a simple model incorporating a contractile element in series with the tendon (SE) is used in [151, 161]. Similarly, a contractile element in parallel with a parallel element (PE) has also been used in literature ([1], Voigt configuration).

Pick and Cole reported the passive dynamics of arm for two conditions [113], based on the measurement of steering torque and angle in response to a filtered pseudo-random binary-sequence excitation. The first condition involves minimal gripping of the steering wheel, while avoiding sliding of hands relative to wheel (relaxed muscle); the second condition involves resisting the motion of steering wheel by co-contracting and stiffening the muscles. It is shown that the measurements can be represented by a system lumped at the steering wheel and can easily fit to a second order transfer function of inertia, damping and stiffness. It is also shown that in the stiffened muscle condition in comparison to the relaxed condition, the damping parameter is slightly and stiffness parameter is significantly increased while the change in inertia is negligible. Later, they used an electromyography

[2]the smallest anatomical unit that contracts like a muscle

approach [114, 117] to investigate the key muscles involved to generate the steering torque while performing an isometric and a dynamical steering maneuvers on a driving simulator, and later for a lane change maneuver [115].

2.5.3 Stretch Reflex

Each muscle is stimulated by the release of chemical materials from a somatic motor neuron. Motor neurons (nerve cell) originate from the spinal cords, and carry the impulse-shape signals (action potential) to the muscle fibers. Motor neurons (alpha and gamma motor neurons) entering a muscle (interafusally and extrafusally) branch and form synapses with a number of muscle fibers as shown in Fig. 2.5. The motor neuron and all muscle fibers that it innervate are called a motor unit. Often a group of motor units (so called motor pool) work together to coordinate a muscle contraction. The size of a motor unit may vary significantly from a few synapses (for eye muscles) to thousands of synapses (for big leg muscles).

To coordinate the muscle properly, the sensory information about the muscle length and tension is required. Golgi tendon organ and muscle spindle afferents are two important sensory receptors of the muscle, providing sensory information about muscle tension and muscle length and contraction velocity, respectively. The muscle length and velocity information (primary muscle spindle afferent, Ia) is used by reflex mechanisms to control the muscle length against the unwanted disturbances, and the Golgi organ (Ib afferent) is used to regulated the muscle force.

Alpha motor neurons are activated from motor cortex or higher centers, while gamma motor neurons are activated from brain stem or cerebellum. The direct command of limb movement is going through alpha motor neurons to the muscles motor units while the gamma motor neurons adjusts the sensitivity of the muscle spindles. The simultaneous activation of alpha and gamma motor neurons are required for a movement. For example, during a voluntary muscle shortening, its spindles have to shorten too, to retain the same level of intrafusal fiber tension. This is called alpha-gamma co-activation, which can be represented by the feedforward and feedback control of the muscle. The stretch reflex (my-

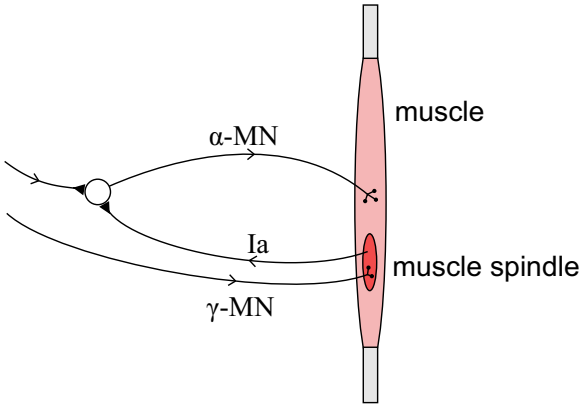

Figure 2.5: The schematics view of stretch reflex mechanism including α and γ motor neurons

otatic reflex) is a muscle contraction in response to stretching within the muscle. In the presence of disturbance (involuntary muscle stretch), the primary muscle spindle (Ia) registers a different muscle length from the desired muscle length set by gamma motoneuons. This difference excites the alpha-motor neurons (using M1 pathways) to increase the firing rate, which then increases the muscle force to oppose the unwanted stretch. The communication between the peripheral and central nervous system runs through the pathways in the spinal cords. Spinal mono-synaptic feedback (M1) pathway is the fastest feedback pathway, which takes about 20-30 ms for arm muscles [29], and has the major role in maintaining of posture. Mono-synaptic spinal reflex is one mechanism for automatic regulation of skeletal muscle length; different pathways are also known to reduce the activity of antagonist muscles.

Merton [71] constructed a reflex loop consisting of spindles and alpha motor neurons forming a feedback-loop on the muscle length; a similar approach has been employed by [86, 24].

The co-activation of α and γ motoneuons in the steering tasks has been considered in [21, 22, 53]; these signals are generated by a cognitive controller as the feedforward, and a corrector as the feedback. These signals show the relationship between the steering wheel torque and angle, and not in the muscle activation level. It is shown in the occurrence of

steering angle overlay, the driver NMS system interacts with steering system soon after the fault; the stretch reflex attempts to return the steering wheel to the zero position, and then after the cognition delay, the path-following response dominates the steering response.

2.5.4 Intrinsic Stiffness

The Central Nervous System (CNS) uses two mechanisms to maintain the limb position in the presence of external disturbances: by using the stretch reflex system (mentioned above) and by increasing the intrinsic stiffness of skeletal joints. The intrinsic muscle stiffness has no time delay, whereas the stretch reflex is more energy-efficient.

It is known that by co-contraction of agonist and antagonist muscles, the joint stiffness and damping can be modulated without altering the net joint torque. Muscle co-contraction is known to stabilize limb movements [97, 96, 162, 72] and this feature is used in many motor control models [37, 142]. Winters and Stark [152, 154] could accurately predict the limb stiffness by employing an eighth-order agonist and antagonist Hill-type muscle. The series element (SE) in the Hill-type muscle model, which simulates passive elasticity of muscle tissue and tendon, play an important role in the joint impedance. In the presence of antagonist co-contraction, the series elastic stiffness increases non-linearly, which increases the joint stiffness [153, 154].

By performing EMG experiments on a driver's arm performing a lane change maneuver on a driving simulator, Pick and Cole in [115, 116] reported that increase in the muscle co-contraction improves the path-following accuracy. However, in this experiment, the stretch reflex and muscle co-contraction are considered as the only means of stabilizing the steering, and the feedforward/active/voluntary control is neglected. The co-contraction stiffness is implemented by a linear spring acting on the steering wheel angle, where stiffness is proportional to the co-contraction parameter. The co-contraction parameter is defined by:

$$I_c(t) = (M_{+ve} - M_{-ve}) - |M_z| \tag{2.2}$$

where M_{+ve} is the steering torque generated by the positive muscles, M_{-ve} is the steering

torque generated by the negative muscles and $M_z = M_{+ve} + M_{-ve}$ is the resultant steering torque generated by the arms. The authors identified the torque-generating muscles in a steering maneuver by measuring the muscle EMG [114]. The co-contraction phenomenon during the steering maneuver was observed to increase limb stiffness, and thus the bandwidth for the control loop, which allowed smaller path-following errors. It can be shown that during normal driving conditions, elevation of the co-contraction level is mainly because inexperienced drivers attempt to compensate for their own control imperfections or internal noise [64]. However, even experienced drivers employ co-contraction in order to be more robust to disturbances, and to compensate for their own inaccurate control actions.

2.6 Control Objectives for EPS Systems

In contrast to that of conventional feedback systems, in the design of an EPS controller, or in general an active steering controller, there are no well-defined measurements for the driver steering feel and comfort. Steering feel and comfort are subjective matters, because they vary according to drivers and driving conditions, and cannot be evaluated by physical measurements. Several studies have been conducted to identify the correlations between what drivers feel and vehicle handling measurements [121, 123, 122, 25, 169]; however, they can only be used as guidelines to satisfy such criteria.

Some drivers complain about loose or heavy steering, and also unpleasant oscillations at the steering wheel of the cars equipped with EPS systems. For example in 2009, there were some complaints about the Toyota Corolla's EPS system; some drivers said it had a wobbly and off-center steering feel. Accordingly, the National Highway Traffic Safety Administration (*NHTSA*) opened an investigation into Corolla's EPS system following 168 complaints, but the *NHTSA* concluded there was no actual defect in the cars themselves. In fact, the *NHTSA* reported that "the alleged defect is a driver-related preference for a less sensitive on-center steering feel" [106].

Several studies have been devoted to steering feel issues. Norman [107] studied the interaction between drivers and vehicles. Norman's study led to a technique to dynam-

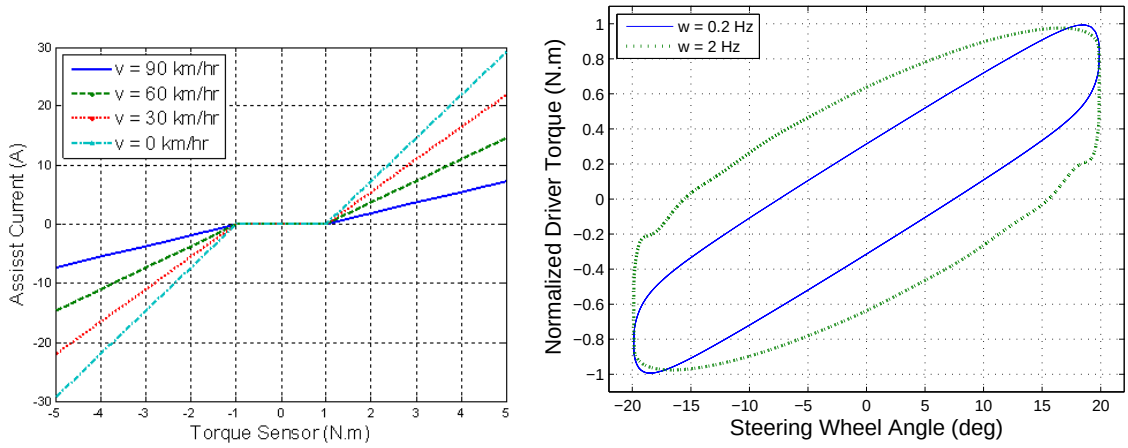

(a) (b)

Figure 2.6: (a) Typical characteristic curves of an EPS system, (b) Lissajous curve of a typical EPS with high and low frequency inputs

ically measure and characterize the non-linear behavior of a power steering system for on-center handling. Later, Farrer [36] introduced new characteristics including steering activity, steering feel, and vehicle response for handling quality. Morita et al. [99, 100, 101] introduced driver feel criteria for an EPS based on a variable gear transmission steering system, and determined that the unpleasant reaction force at the steering wheel may be caused by a combination of external disturbances, mechanical flexibility and friction non-linearity. The authors used the phase shift and oscillation characteristics of the Lissajous curves between driver torque and steering wheel angle to compare the steering feels. For example, Fig. 2.6b shows the Lissajous curves of a typical EPS system with high and low frequency inputs (steering speeds). In this figure, both oscillation and phase shift can be observed in the high frequency input.

The main responsibility of EPS systems is to reduce the driver physical effort. Therefore, the assistance torque should compensate for most of the resistance torque at the steering wheel. As a result, almost all power steering systems have a component in their logic to generate an assist torque proportional to the driver torque. This relation is typically presented in so-called characteristic curves [17]. The shape and dynamics of these curves were

studied in the literature to provide better assistance and feel for drivers [168, 167, 74, 157]. Typically, the steering characteristic curves are a bi-linear or multi-linear function of the driver steering torque. For example, Fig. 2.6a shows a steering characteristic curve which is a bi-linear function of the column torque, where the rate of assistance varies with the vehicle speed. This characteristic curve consists of an unassisted zone to avoid the off-center feeling and a linear steering assistance zone. A similar characteristic curve is utilized in the EPS controllers.

Adams [4] studied the problem of power steering road feel. The road feel objective deals with the level of permissible resistive torque in various road surface conditions and vehicle speeds that the driver perceives. It was shown that eliminating certain high-frequency components of the resistance forces improves the steering feel [4]. Some authors utilized disturbance observers to estimate the road/tire interaction force, specifically the feedback to the steering wheel from the low-frequency portion of the road-tire forces [14, 140, 16]. A road/tire force estimator developed by Lawson and Chen [73] was used to design a torque sensor fault-detection control for EPS systems, in which the total motor load/disturbance torque was estimated using a Luenberger disturbance observer. Alternatively, Marouf [85] developed a sliding mode observer to estimate the driver torque and the reaction force using only the steering wheel angle and the assist motor angle measurements without the need for a torque sensor and a vehicle lateral speed sensor.

In the investigations by Zaremba and Davis [163], analytical expressions of assist force, driver feel, and steering response to driver inputs, as well as assist forces in the form of transfer functions are defined for a double-pinion EPS system. The authors defined the measure of driver feel of the road as:

$$J_F = (\frac{1}{2\pi\omega_0}\int_0^{\omega_0} |H_F j\omega|^2 d\omega)^{1/2} \tag{2.3}$$

where ω_0 is the frequency range of interest and H_F is given as follows:

$$H_F(j\omega) = \frac{T_d(j\omega)}{F_R(j\omega)} \tag{2.4}$$

where T_d and F_R are driver torque and rack force, respectively.

2.7 Control Approaches

Designing an EPS system requires solving a tracking control problem under the existence of disturbance and uncertainty. A wide range of control strategies have been reported in the literature including classical, model-based, and black-box control methods for the EPS controller. This section is followed by a review of the classical and model-based EPS control design strategies. The black-box control methods have been left out since they are not in the scope of this thesis.

2.7.1 Classical Control Methods

Proportional Integral Derivative (PID) controllers with compensators have been extensively and successfully implemented in EPS systems [149, 164, 20]. The advantages of compensators and PID control algorithms over other control methods are their simple structure and low implementation cost. However, these controllers have poor transient performance in the presence of external disturbances or uncertainties. Badawy et al. [8] implemented a "Return Algorithm" and "Damping Algorithm" components with which the EPS tracking controller logic was implemented. These two algorithms use the steering wheel position and velocity information to guarantee the return of the steering wheel to the exact center position upon release. The root locus controller design method was used in [38] for a hydraulic power steering system, in which zeros and poles are added to the system to force the desired behavior of the closed loop system.

2.7.2 Model-Based Control Methods

The robust control approach has been regularly used in the EPS control design to improve robustness and performance of the system [14, 15, 27]. H_∞ synthesis is used in [13, 140, 12] to provide assistance, while simultaneously minimizing the effect of disturbances on the outputs. Zhao and Wang [166] designed a mixed H_2/H_∞ controller to obtain better system performance, and to improve steering sensitivity and stability by adding these objectives

to the previous objective function. A similar approach has been used in [34, 35], where the passivity constraint of the human drivers is considered in the design to ensure the closed-loop stability. Li [15] developed a two-stage controller for a column-type EPS system. The first stage is a PI controller to improve motor reaction response, while the second stage is an H_∞ controller which defines the desired assist torque based on the road feel performance requirements. In [16], model reduction for a similarly structured controller was discussed and implemented to reduce the computational resources. In comparison to the original controller, the reduced-order controller performs like the original one in a normal situation as opposed to its decreased performance in the presence of random disturbances.

The Linear Quadratic Gaussian (LQG) control method also has been used in designing EPS controllers. Parmar et al. [108] designed an LQG controller consisting of a Linear Quadratic Regulator (LQR) in conjunction with a Kalman filter for a double-pinion type EPS system. The LQR was designed to provide assistance proportional to the steering column torque. Then, the Kalman filter was utilized to estimate the dynamics of the system's states in the presence of measurement noise. Later in [109], the authors expanded the LQG controller for a bi-linear characteristic curve. LQG control is used to reduce the number of required sensors and to provide assistance in the presence of external disturbance and measurement noise [108, 109, 18]. To the best of author's knowledge, the Model Predictive Control (MPC) theory has not been used in the EPS systems.

Relatively less effort has been made in designing friction compensation and disturbance observer controllers for EPS systems. A friction compensation control is developed in [136] by considering an equivalent friction model of the worm gear. Then, the prediction of this model is used to compensate for the friction through motor torque. Dannöhl et al. [27] developed a modified H_∞ controller for a rack-assisted EPS by considering separate unknown external forces to model friction at the steering wheel, rack and motor. The modified controller enhanced the performance of the system in comparison with the original H_∞ controller. To suppress periodic disturbances (shimmy) at the steering column, disturbance compensation controllers have been developed. In these controllers, the periodic disturbance is extracted from the measured steering torque using an analytical approach [44] or by use of a non-linear low-pass filter [75], and then compensated through the actu-

ator. A disturbance observer also has been developed to estimate the steering torque load and driver steering torque using an extended state observer [31], or Kalman filter [91] or sliding mode observer [76]; this estimation is then used to produce a desired assistance in the presence of external disturbances.

2.8 Chapter Summary

In this chapter, different approaches for modeling of the electric power steering systems as well as different EPS control strategies have been introduced. It can be noted that there is no clear and well established objective function in the designing of EPS controllers to improve driver's steering feel. The traditional performance criteria used in EPS systems such as comfort and feel are subjective matters and vary according to drivers and driving conditions. One way to improve the traditional design of steering systems is to consider the driver's characteristics and preferences in the design process. However, developing driver-based technologies requires proper understanding of the driver itself. Therefore, in this chapter, the relevant passive and active properties related to the neuromusculoskeletal dynamics of driver's arm is briefly explored.

With such understanding, one possible solution might be using this knowledge to tune or design a steering system to provide improved steering response and better steering feel. However, how steering response and steering feel can be measured or even defined is the subject of ongoing research and debate. One important tool for designing new steering products is to develop a realistic driver model to reduce the time-consuming trial and error process of designing products, and eventually reduce the vehicle's development time and cost. Some research studies investigated the passive dynamics of the neuromuscular system of the driver arm to understand the driver dynamics. However, the effect of the force generating part of muscle on the steering dynamics as well as the effect of physical ability, gender and age has not been studied.

Mechanics is the paradise of the mathematical sciences because by means of it one comes to the fruits of mathematics.

Leonardo da Vinci (1452 – 1519)

3

Electric Power Steering (EPS) System Modeling

A clear understanding of the dynamics of a system is crucial in designing control systems, since not only does it strengthen our knowledge of the system but also it reduces development time and cost. Therefore, in this thesis, a full vehicle model including a column-assisted EPS system is developed in *MapleSim*[1] using a multibody dynamics approach. This model is used to design and evaluate an EPS controller. Although the high-fidelity model is suitable to study the system's dynamics, it is not suitable to be used within a model-based controller due to its non-linearities and complexities. Low-order linear models

[1]MapleSim is a registered trademark of Maplesoft

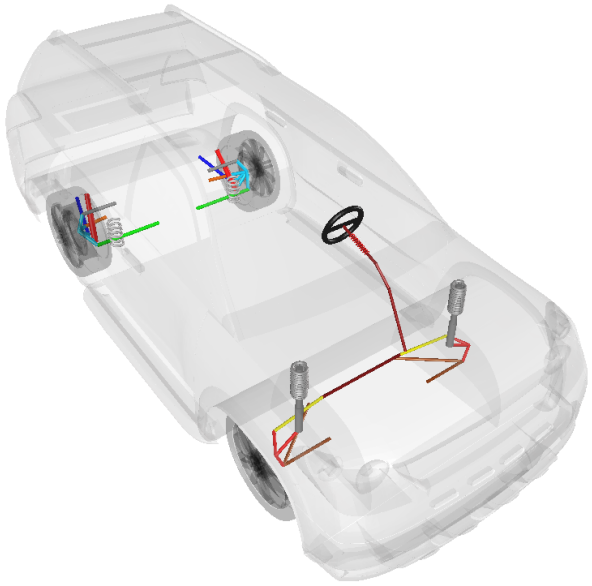

Figure 3.1: A view of the vehicle model in the MapleSim program

are more desirable than higher-order ones since they preserve the important dynamics of the system and simultaneously simplify the controller.

In this chapter, a high-fidelity multibody dynamical model of vehicle, a control-oriented model, and a simplified model of vehicle (internal model) are presented and the accuracy of the two latter models are verified against the high-fidelity model.

3.1 Full Vehicle Model in MapleSim

In this research, a vehicle model with a front MacPherson suspension and a rear multi-link/semi-trailing arm suspension typical in an SUV (Sport Utility Vehicle) is developed in MapleSim as shown in Fig. 3.1. The symbolic modeling engine of MapleSim is able to generate optimized C code describing the system's equations of motion. These symbolically generated equations can reduce the simulation time significantly and allow extensive manipulation of the system's equations. The developed model consists of 50 generalized coordinates coupled by 34 algebraic equations. This model in total has 16 degrees of freedom

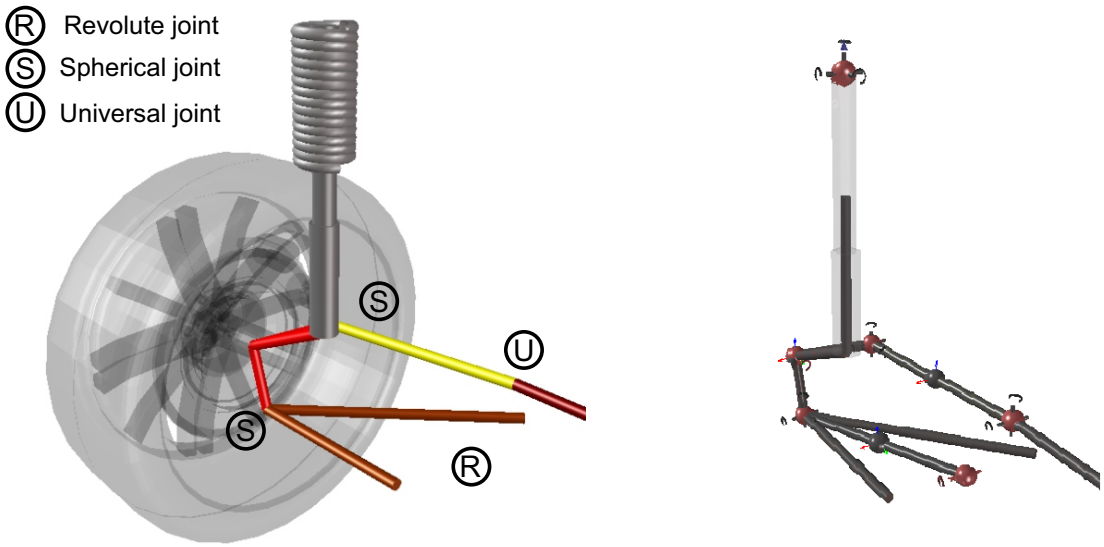

(a) (b)

Figure 3.2: (a) Rear multi-link muspension, (b) Rear multi-link suspension in MapleSim construction mode

(DOF). Six DOF are associated with the rigid body motion, four are related to the wheels' spin, four are related to the suspensions' vertical motion and two are associated with the steering motion. The simulation integration time for a sinusoidal steering maneuver is five times longer than real-time.

3.1.1 Chassis - Front and Rear Suspensions

Front Suspension

The MacPherson suspension topology is a popular choice for automobiles front suspension because of its low manufacturing cost and simplicity. A conventional MacPherson suspension consists of a lower control arm, spindle and strut as shown in Fig. 3.2. The lower control arm is connected to the chassis (with a revolute joint) and to the spindle (with a spherical joint) allowing vertical and lateral movements of the tire. The strut, including a

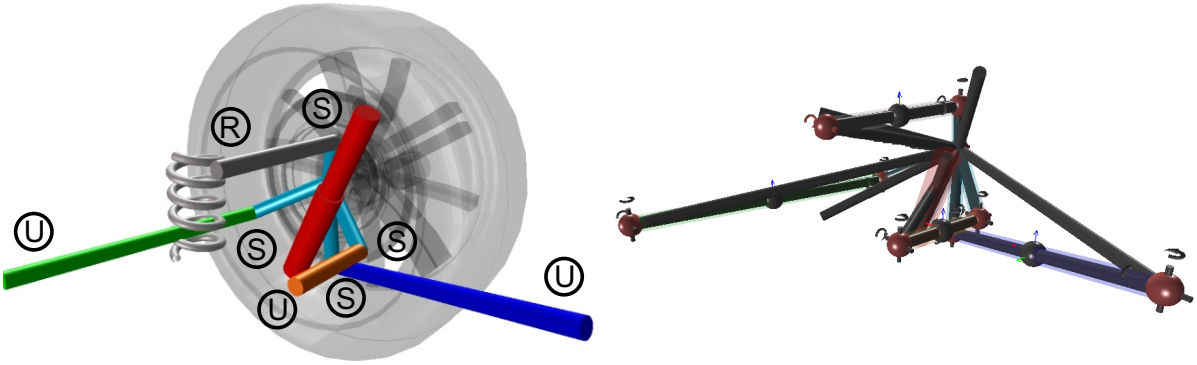

(a) (b)

Figure 3.3: (a) Rear Multi-link Suspension, (b) Rear Multi-link Suspension in MapleSim construction mode

co-linear spring and shock absorber, is mounted on the spindle to carry the vehicle weight and reduce the vibrations to the body. The MacPherson suspension has three rigid body components, which results in a one degree-of-freedom mechanism.

Rear Suspension

A multi-link/semi-trailing arm rear suspension, consisting of four arms connecting the spindle to the chassis, is developed in MapleSim. The arms are connected to the spindle by spherical joints, and to the body by spherical and revolute joints as shown in Fig. 3.3. A spring and a shock absorber is mounted separately on the arms to isolate the body from the road irregularities. A similar mechanism to that shown in [68] has been used to construct the multi-link rear suspension. The Multi-link suspension consists of five rigid bodies, four spherical joints, three universal joints and a revolute joint. This mechanism results in one degree of freedom in the vertical direction of wheel movement. The kinematics of the suspension systems are verified against an experimentally validated ADAMS model. More information about the high-fidelity vehicle model can be found in [46, 45].

Body

The vehicle center of mass location and mass and inertia reflects the SUV mass and inertia, as given in Table. 3.1. The positive x-axis of the vehicle coordinate system points in the direction of movement, the positive y-axis points to its left, and the positive z-axis points upward.

Table 3.1: List of parameters used in the body

Parameters	Description	Value	Unit
$Mass$	vehicle mass	2000	[kg]
$Inertia$	vehicle body moments of inertia $[x, y, z]$	[450,1600, 2000]	[kg.m^2]
CM	location of center of mass $[x, y, z]$	[2.57,0,0.8]	[m]

3.1.2 Fiala Tire Model

Tires are the key element in modeling vehicle dynamics because not only do they support the vehicle weight, but they also provide the necessary forces and moments for changing the speed and direction of the vehicle.

In this study, the Fiala tire model is used to simulate the tire/contact patch interaction [102, 39]. The Fiala tire in comparison with other more sophisticated tire models, such as Pacejka, has fewer parameters and is therefore simpler to construct. However, this simplification limits the accuracy of the model. The Fiala tire model does not consider the effect of inclination angle, the lateral and longitudinal stiffness are assumed constant during simulation, the overturning moment (M_x) is assumed zero and the tire's force and moment curves must go through the origin. Despite these limitations and assumptions, the Fiala tire model is a good candidate to study steering tasks. This is because the Fiala tire model can capture the fundamental behavior of the tire using only a few parameters and all of the tire parameters can be measured or estimated with reasonable accuracy. The

positive direction of local axes in the wheel are defined in the same direction of the center of mass coordinate system.

The Fiala tire model requires tire slip angle (α), longitudinal slip (S) and tire normal force (F_z) as inputs to calculate longitudinal and lateral forces and rolling resistance (M_y) and self-aligning moments (M_z) as follows:

$$S_{L\alpha} = \sqrt[2]{S^2 + tan^2(\alpha)} \tag{3.1}$$

$$\mu = \mu_0 - S_{L\alpha}(\mu_0 - \mu_1) \tag{3.2}$$

$$H = 1 - \frac{C_\alpha |tan(\alpha)|}{3\mu |F_z|} \tag{3.3}$$

$$F_x = \begin{cases} C_s S & \text{if } |S| < \left|\frac{\mu F_z}{2C_s}\right| \\ \text{sgn}(S)\left(\mu F_z - \left(\frac{\mu F_z}{4|S|C_s}\right)\right) & \text{otherwise} \end{cases} \tag{3.4}$$

$$F_y = \begin{cases} -\mu |F_z|(1 - H^3)\text{sgn}(\alpha) & \text{if } |\alpha| < \arctan\left(\frac{3\mu F_z}{C_\alpha}\right) \\ -\mu |F_z| \text{sgn}(\alpha) & \text{otherwise} \end{cases} \tag{3.5}$$

$$M_y = \begin{cases} C_r F_z & \text{if } \Omega < 0 \\ -C_r F_z & \text{otherwise} \end{cases} \tag{3.6}$$

$$M_z = \begin{cases} \mu F_z D_2 (1 - H) H^3 \text{sgn}(\alpha) & \text{if } |\alpha| < \arctan\left(\frac{3\mu F_z}{C_\alpha}\right) \\ 0 & \text{otherwise} \end{cases} \tag{3.7}$$

The cornering stiffness, longitudinal stiffness, rolling resistance, peak coefficient of friction, sliding coefficient of friction and the width of the tire are the additional parameters that are required for the Fiala tire model. The tire parameters used in the simulations are given in Table. 3.2. The same tire model is used for front and rear wheels.

Table 3.2: List of parameters used in the tire model

Parameters	Description	Value	Unit
μ_0	the peak coefficient of friction between tire and ground (the static coefficient of friction)	1	[-]
μ_1	the steady-state coefficient of friction between tire and ground (the sliding coefficient of friction)	0.9	[-]
C_α	tire cornering stiffness (the slope of the F_y vs α of the tire curve at $\alpha = 0$)	117000	[N/rad]
C_S	tire longitudinal stiffness (the slope of the F_x vs S of the tire curve at $S = 0$)	115000	[N/rad]
C_r	tire rolling resistance coefficient	0.01	[N/rad]
D_2	half of the tire width	0.1075	[m]

3.1.3 Steering System Model in MapleSim

Since the steering system is the focus of this research, the model construction is described in detail. A conventional rack and pinion steering system consists of two universal joints that connect the three steering column shafts to transmit the rotational motion of the steering wheel to the pinion (see Fig. 3.4). The steering wheel is connected to the steering column housing by a cylindrical joint allowing rotational and telescopic movements of steering column, and at the other end, a rack-and-pinion gear is used to transform the rotational motion of the lower steering shaft to the translational motion of the rack with a specified reduction ratio. As shown in Fig. 3.4b, the rack and pinion steering system is a one-degree of freedom mechanism, in which rotating the steering wheel results in a unique displacement of the rack and the wheel.

Universal (Hooke's) joints are used to transfer torque between inclined axes. One revolution of inbound shaft results one revolution of outbound shaft. However, depending on the articulation angle, the angular acceleration and deceleration may not be transmitted evenly. To avoid the non-uniformity, double universal joints with equal bending angles and 90 degree phase shift between input and output shafts can be used, as shown in Fig. 3.4b.

In electric power steering systems, the driver's steering torque should be known to

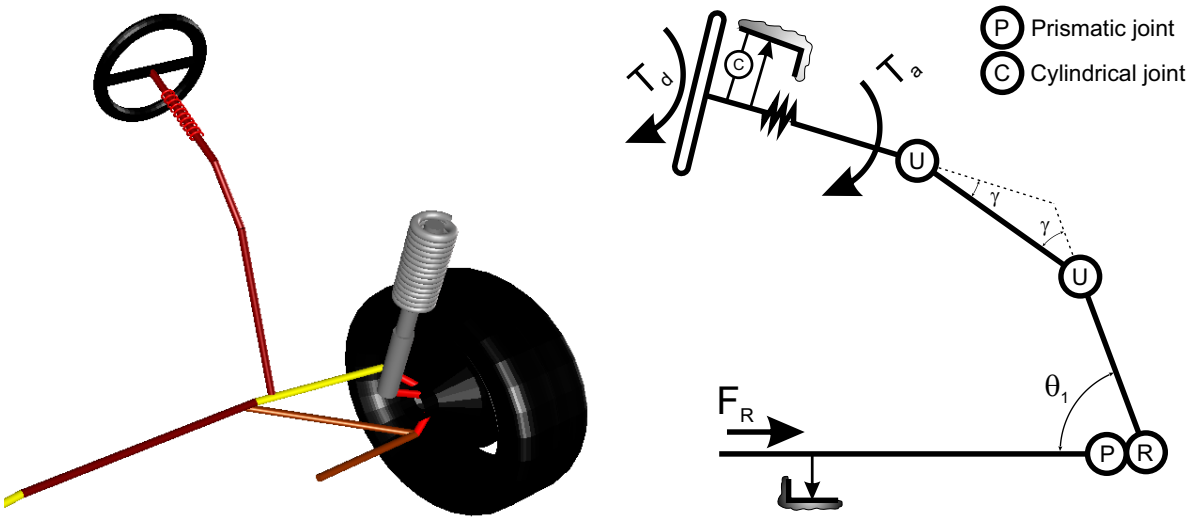

(a) (b)

Figure 3.4: (a) A view of the developed steering system in MapleSim, (b) Schematic view of steering system in MapleSim, including the location of driver torque (T_d), assist torque (T_a), disturbance torque ($T_r = F_r r_p$), and Coulomb frictions

the EPS controller to provide proper assistance, proportional to driver's intention. Strain gauges and twist angle measurements are common ways of measuring the steering torque. In both cases an intermediate compliant member in the steering shaft (usually a torsion bar) is required. Torsion bars (torque sensors) are an essential part of electric and hydraulic power steering systems and the major source of flexibility in the steering systems. In the high-fidelity model, a torsion bar is placed in the upper steering shaft by employing a linear spring and damper representing the shaft elasticity properties. By registering a differential (or relative) angular displacement between the two ends of the bar, and by considering the elastic behavior of shaft, it can measure the torque transferring through the shaft, as shown in equation Eq. (3.8).

$$T_{tb} = K_{tb}\Delta\theta_{tb} + C_{tb}\Delta\dot{\theta}_{tb} \tag{3.8}$$

where K_{tb} and C_{tb} are the stiffness and damping coefficients of the torsion bar, and $\Delta\theta_{tb}$ is

the torsion bar deflection. The torsional stiffness of universal joint, worm gear and pinion is at least 1000 times greater than the torsion bar stiffness. Therefore, flexibility of these components are neglected in the model.

Table 3.3: List of parameters used in the high-fidelity steering system

Parameters	Description	Value	Unit
$r_{unloaded}$	unloaded tire radius	0.45	[m]
K_{tb}	torsion bar stiffness	117	[N.m/rad]
C_{tb}	torsion bar damping	2.2	[N.m.s/rad]
θ_1	lower steering shaft angle	118.6	[degree]
γ	universal joint bending angles	22.3	[degree]
L_m	electric motor inductance coefficient	1.5 10^{-5}	[H]
R_m	electric motor resistance coefficient	0.15	[ohms]
K_e	electric motor back electromotive force (emf) coefficient	0.02	[V.s/rad]
a_{sw}, b_{sw}	viscous friction coefficients of the steering wheel	0,1	[-]
$T_{c,sw}, T_{s,sw}$	coulomb friction coefficients of the rack	141.9,130	[N.m]

Direct current (DC) electric motors connecting through a worm gear to the steering column are commonly used in EPS systems to provide the assist torque [137]. In this thesis, a first-order differential equation is used to simulate the DC electric motor dynamics. This model is given by:

$$\begin{aligned} L_m \frac{\mathrm{d}i}{\mathrm{d}t} + R_m i + K_e \dot{\theta}_m &= u_v \\ T_e &= K_e i \end{aligned} \tag{3.9}$$

where i and u_v are the current and terminal voltage of the DC motor, L_m, R_m, and K_e are the inductance, resistance and back electromotive force (emf) coefficients of the electric motor, and T_e and $\dot{\theta}_m$ are the motor torque and angular velocity of the motor shaft.

In the physical system, friction is generated at the mechanical connections between the steering wheel and its housing, the rack and its housing and in the worm gear [132]. In this thesis, a friction model representing the Coulomb and viscous part of the friction force as given in Eq. (3.10) has been used [7].

$$F_{fric}(t) = a\ v_{rel}^{b} + \tanh\left(\frac{v_{rel}}{v_0}\right)\left(f_c + (f_s - f_c)^{-|\frac{v_{rel}}{v_s}|^n}\right) \tag{3.10}$$

where a and b are the viscous damping coefficient and exponent and f_s and f_c are the Coulomb friction coefficients. v_{rel} is the relative velocity between the two components and v_s, v_0 and n are shaping factors. The numerical value of the parameters used in the steering system are shown in Table. 3.3.

3.2 Control-Oriented Model of EPS System

In this thesis, a simplified control-oriented model is developed for use in the EPS controller. Since the EPS controller has to perform in real-time, and since the amount of memory and process time allocated to steering control in the vehicle's Electronic Control Unit (ECU) are limited, a simplified control-oriented model is used to reduce the computational resources required.

Since the proposed control method is based on linear control theory, the control-oriented model should be linear. Therefore, a seventh-order linear model of a vehicle including a column-type EPS system is presented as the control-oriented model. As shown in Fig. 3.5, this reduced model includes the steering wheel, steering intermediate shaft, electric motor, and lateral dynamics of vehicle. These steering components have been selected because of their important influence in the steering dynamics. The lateral dynamics of the vehicle have been included in this model to predict the lateral force of front tires because it makes the largest contribution to the resistive steering torque. Considering the moment of inertia and the viscous damping of a steering wheel, the steering wheel equation of motion is obtained:

$$J_{sw}\ddot{\theta}_{sw} = -b_{sw}\dot{\theta}_{sw} + T_{tb} + u_\tau \tag{3.11}$$

$$T_{tb} = K_{tb}(\theta_{sw} - \theta_r) \tag{3.12}$$

where u_τ and T_{tb} are the driver torque and the torque developed due to flexibility of the torsion bar. θ_{sw}, J_{sw} and b_{sw} are angle of rotation, moment of inertia and viscous damping

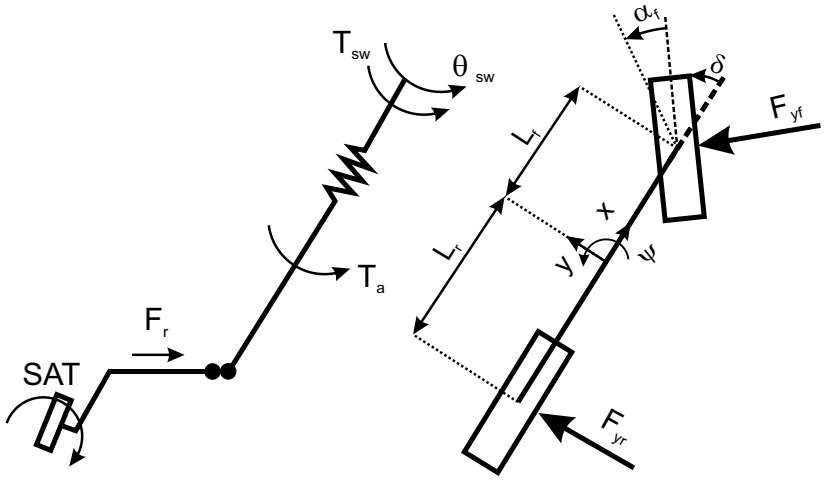

Figure 3.5: Schematic view of the control-oriented model confined in the LQG controller including a linear bicycle model (right) with a column-assisted EPS system (left)

of the steering column.

The rack and its connection to the wheel spindle as well as intermediate shaft of steering are combined together, and represented as a single inertia at the intermediate shaft. The dynamics of the steering intermediate shaft are described by:

$$J_r\ddot{\theta}_r = -K_r\theta_r - b_r\dot{\theta}_r + T_{tb} + T_a + T_r + u_d \tag{3.13}$$

where θ_r, J_r and b_r are angular displacement, inertia and damping of the intermediate shaft. K_r is the stiffness induced by the inclined kingping axis on the rack displacement. $G_{steering}$ is the ratio of the rotation of steering wheel angle to the average value of left and right wheel steer angles. T_r and u_d represent the self-aligning torque (SAT) and external torque due to road irregularities or disturbances at the intermediate shaft, respectively. T_a is the assist torque provided by the DC motor; assuming the worm gear ratio of G, $T_a = GT_e$ (see Eq. (3.9)).

A single-track or "bicycle" model can be used to analyze the vehicle dynamics behavior as shown in Fig. 3.5. This model includes several important exclusions and simplifications. These simplifications greatly reduce the model's complexity and degrees of freedom, but

do not significantly affect the vehicle lateral dynamics. For example, in the bicycle model, the height of vehicle's center of gravity is at the road surface; therefore, the roll and pitch angles of the vehicle are neglected. As a result, the normal tire force at the left and right sides of vehicle remain the same during cornering. Thus, the lateral forces produced by the front or rear wheels remain the same, so the left and right wheels are lumped together and represented by a single wheel. In this section, a bicycle model is used to capture the lateral dynamics of the vehicle and estimate the self-aligning torque of the high-fidelity vehicle. The vehicle's velocity at the center of mass is denoted by V and makes an angle β with the heading direction of the vehicle. The side slip angle (β) and yaw rate (ω_z) of the vehicle's center of mass are selected as the state variables of the bicycle model. The equations of motion of this model are expressed as follows:

$$m v_x \left(\dot{\beta} + \omega_z\right) = F_{yf} + F_{yr} \tag{3.14}$$

$$I_{zz}\, \dot{\omega}_z = L_f\, F_{yf} - L_r\, F_{yr} \tag{3.15}$$

where F_{yf} and F_{yr} are front and rear lateral force of the wheels and are approximated by the linear tire model in contrast to the Fiala tire model used in the high-fidelity model:

$$F_{yf} = C_{\alpha f}\alpha_f \tag{3.16}$$

$$F_{yr} = C_{\alpha r}\alpha_r \tag{3.17}$$

As shown in Fig. 3.5, the front and rear slip angles with small steer angles can be approximated as follows:

$$\alpha_f = \frac{v_y + L_f\omega_z}{v_x} - \delta_f \tag{3.18}$$

$$\alpha_r = \frac{v_y - L_f\omega_z}{v_x} \tag{3.19}$$

In these equations, the longitudinal velocity of the vehicle at center of mass is assumed

Table 3.4: List of parameters used in the control-oriented model

Parameters	Description	Value	Unit
J_{sw}	inertia of steering wheel	0.0009	[kg.m^2]
b_{sw}	viscous damping of steering wheel	0.008	[N.s/m]
J_r	inertia of steering intermediate shaft and rack	0.01258	[kg.m^2]
b_r	viscous damping of intermediate shaft and rack	3.715	[N.s/m]
K_r	stiffness of intermediate shaft and rack	71.4	[N/m]
$G_{steering}$	average steering ratio	15.29	[m]
L_f	the distance from front tire to c.g.	1.192	[m]
L_r	the distance from rear tire to c.g.	1.548	[m]
m	vehicle mass	2077	[kg]
I_{zz}	vehicle yaw inertia	1995.78	[kg.m^2]
$C_{T\alpha}$	self-aligning-torque stiffness	2000	[N.m/rad]
C_α	front and rear tire cornering stiffness	117000	[N/rad]

constant and is expressed as v_x, and the steering angle of front wheel is represented by δ_f.

Self-aligning torque, which is created by the interaction between the tire and the road, can be found from Eq. (3.7) of Fiala tire model. However, for small slip angles, the SAT is a linear function of slip angle (α_f). Assuming the average steering angle of the wheels is $\delta_f = \theta_r / G_{steering}$, the SAT can be found from Eq. (3.20).

$$T_z = C_{T\alpha}\,\alpha_f = C_{T\alpha}\left(\delta_f - \beta - \frac{L_f\,\omega_z}{v_x}\right) \tag{3.20}$$

The remaining parameters are defined and summarized in Table. 3.4. The control-oriented model consists of four linear ordinary differential equations (ODEs), three of which are second-order which is equivalent to a set of seven first-order linear ODEs. The state-space representation of the control-oriented model is presented in Appendix A.

3.3 Internal Model

Drivers generally steer a vehicle in a predictive way, meaning that based on the their knowledge of the vehicle response they anticipate the vehicle trajectory, and steer the vehicle accordingly. It is hypothesized that a race car driver has a good understanding of the vehicle such as the saturation level of the tires, while a novice driver considers the vehicle as a point mass based on the current state of vehicle [65, 63]. This complexity of the internal model can used as a factor to include the driver skill in the simulations. In this thesis, a column-assisted EPS with a bicycle model of vehicle (control-oriented model) is selected as the internal model. However, the Fiala tire model is used instead of linear tire model to accurately model the tire forces in the internal model. This nonlinear model is used in the control movement of the driver arm.

In the internal model, the longitudinal speed of vehicle is assumed constant; thus, it is a fair assumption that the longitudinal slip (S) is equal to zero. Therefore, the Fiala tire model equations are reduced to Eqs. (3.5) and (3.7), and the longitudinal force and rolling resistance moments are assumed to have a negligible effect. The tire normal forces are found by the static distribution of vehicle weight on the front and rear tires:

$$F_{zf} = \frac{mgL_r}{L_f + L_r}, \quad F_{zf} = \frac{mgL_r}{L_f + L_r} \tag{3.21}$$

where F_{zf} and F_{zr} are the front and rear tire normal forces.

3.4 Model Validation

To use the aforementioned control-oriented and internal models in the control design process, the models should be a good representation of the actual system.

To demonstrate this, a sinusoidal steering maneuver is simulated for the control-oriented, internal and the high-fidelity models. Figure 3.6 shows the torque required to steer the wheels against the steering wheel angle in the following situations. Figure 3.6a shows the

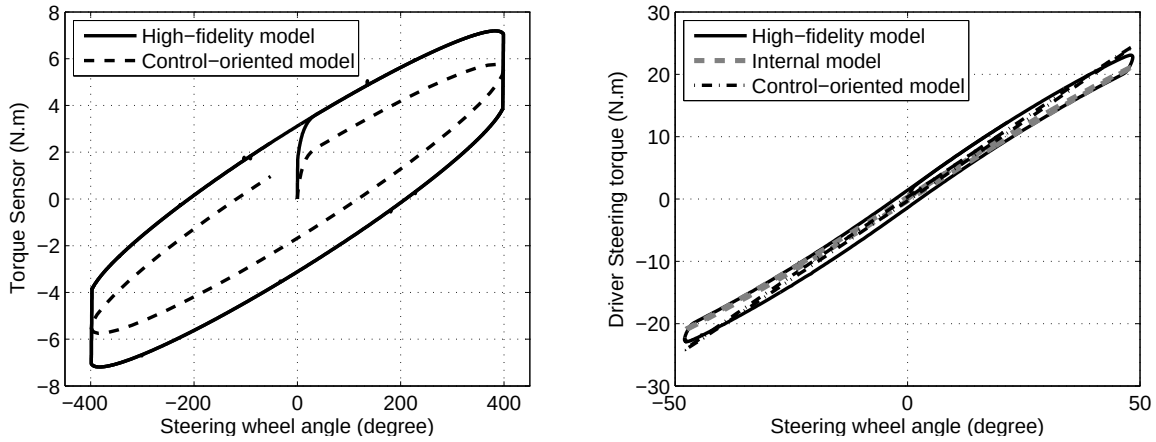

(a) (b)

Figure 3.6: (a) The steering torque required versus steering wheel motion when the front wheels are on the friction-less pads, (b) The steering torque required for a smooth steering wheel motion at 10 m/s vehicle speed

required torque when the wheels are on friction-less pads; this graph is used to identify b_r and K_r coefficients, while Fig. 3.6b is used to estimate the SAT contribution to the required steering torque. In this simulation, the longitudinal speed of the car is 10 m/s (36 km/hr). An optimization approach is used to find the steering and vehicle parameters. The discrepancy seen in Fig. 3.6a is the result of the absence of friction in the control-oriented model. This conclusion is verified by removing the Coulomb friction from the steering system and comparing the steering torques. The Coulomb friction is not included in the control-oriented model to keep the linearity of the model.

Then, a random steering maneuver with different voltage and disturbance inputs to the system as shown in Fig. 3.7a is simulated for the internal model, control-oriented and high-fidelity models. Since the maximum driver torque is usually about 10 $N.m$, a sinusoidal driver torque input with a magnitude of 10 $N.m$ is used. The magnitude of the terminal voltage is assumed to be 5 V, and the magnitude of the disturbance force at the rack is 500 N. Figure 3.7 shows the steering wheel angle, assist torque and lateral acceleration of the high-fidelity vehicle model as well as the tuned control-oriented model and internal

model. These measurements are selected since they are the sensor measurements of the EPS system, and they should agree well with the real measurements (in this case the high-fidelity model). The results show a good correlation between these three models. A shown in Fig. 3.7c, the torque sensor value for all three models is the same since the dynamics between the steering input and torque sensor measurement are closely modeled in all models. However, other measurements have slight differences since the vehicle dynamics is simplified in the control-oriented and internal models.

3.5 Chapter Summary

In this chapter, a high-fidelity vehicle model, control-oriented model and internal model are developed. The high-fidelity vehicle model, including a detailed representation of the vehicle's suspension and steering system, is used to verify two other simplified vehicle models and will be used to evaluate the proposed EPS controller. The control-oriented model consists of a linear bicycle model and a column-assist EPS system; this model will be used inside the EPS controller. The third model is the control-oriented model with non-linear tire models to be used as the internal model confined in the driver model. Based on the results presented in the Section 3.4, all three models show similar behavior when subject to harmonic inputs with magnitudes and frequencies in the ordinary steering range.

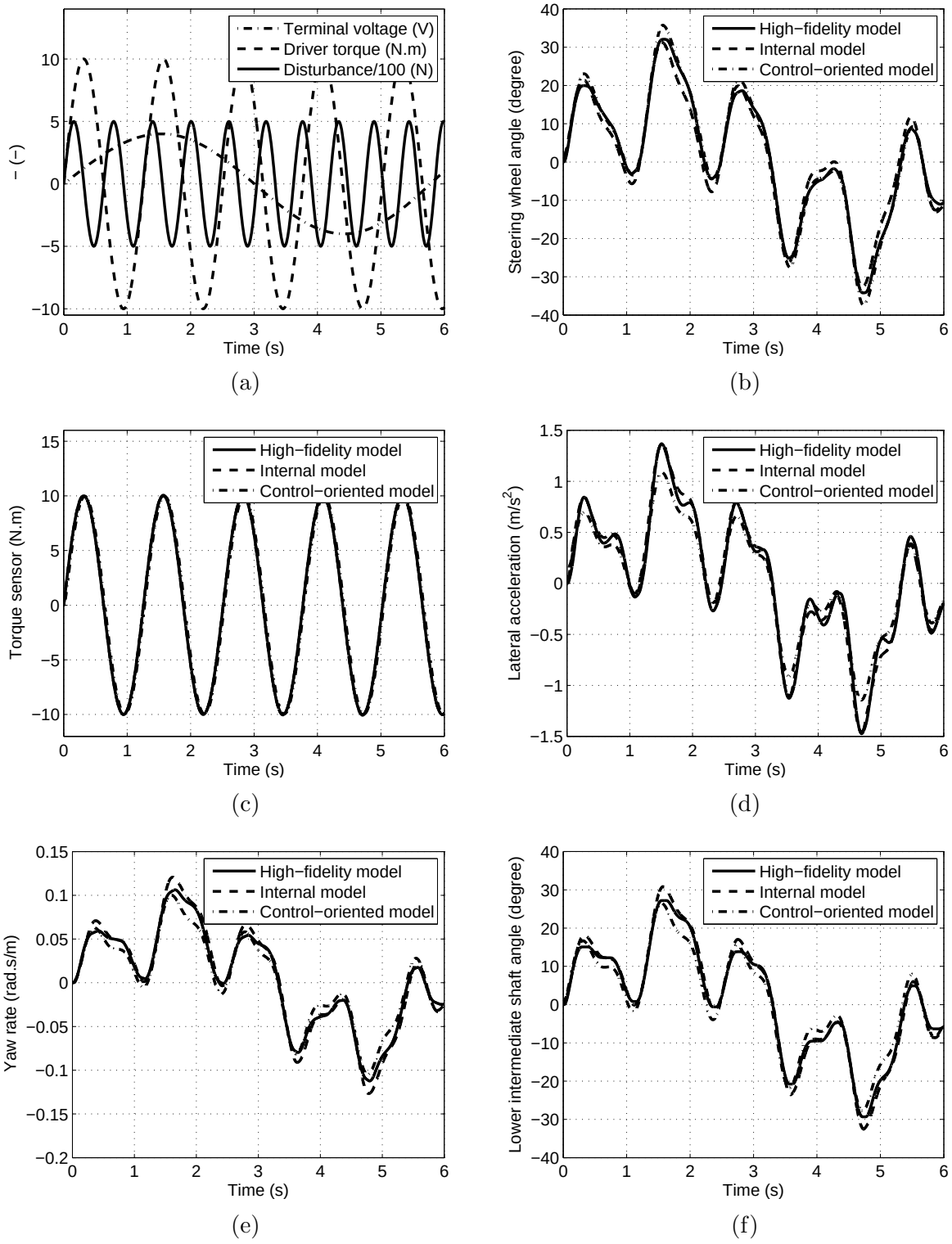

Figure 3.7: Comparison of the control-oriented model with the high-fidelity vehicle model (a) Inputs to the system: terminal voltage, driver torque and disturbance force, (b) Steering wheel angle, (c) Torque sensor (torsion bar torque), (d) Vehicle lateral acceleration, (e) Vehicle yaw rate, (f) Lower intermediate shaft angle

"THE FUNDAMENTAL VARIATIONAL PRINCIPLE
Namely, because the shape of the whole universe is most perfect and, in fact, designed by the wisest creator, nothing in all of the world will occur in which no maximum or minimum rule is somehow shining forth . . . "

Leonhard Euler (1707 – 1783)

4

Neuromusculoskeletal Driver Model

In this chapter, a physics-based driver model including a three-dimensional musculoskeletal model of driver arm and a novel Central Nervous System (CNS) motor control structure, hereafter called the three-dimensional (3D) driver model is developed. A simplified two-dimensional driver model with the same CNS structure, hereafter called the two-dimensional (2D) driver model is also developed. The 3D driver model is used to replicate the neuromusculoskeletal dynamics of a human driver while the 2D driver model will be used in the vehicle component-level design procedures. The simplified 2D driver model conveys the same general characteristics as the high-fidelity (3D) driver model but does not contain all the details of the system.

4.1 Physics-based Three-dimensional Driver Model

Before getting into the details of the high-fidelity (3D) driver model, the author would like to explain the difference between the two types of models that are used in our simulations: the high-fidelity model and the internal models. The high-fidelity model (section 4.1.1) tries to faithfully replicate the real system, and is used to obtain the simulation outputs. The internal models, on the other hand, do not necessarily contain all the details of the system, and are only used to provide some prediction about the real system. These simplified models are confined within the motor control systems (sections 4.2.1 and 4.2.2), and are solved multiple times at each time step. Therefore, the simplicity of the models is vital in keeping the computational burden at a manageable amount. The validity of both types of models is equally important, as the errors in either will affect the reliability of the results. Additionally, due to the interaction of the models, error in the any of models will hinder the interpretation of the results.

4.1.1 3D Musculoskeletal Arm Model

In this section, the 3D musculoskeletal arm model is developed to reliably study the neuromuscular dynamics of steering tasks with a larger range of operations than already published models such as the neuromuscular driver model introduced by Pick and Cole [116].

Figure 4.1a shows the schematic view of the 3D arm model. In this model, the torso (scapula, assumed fixed relative to the vehicle) is attached to the upper arm (humerus) via a spherical joint. The forearm (ulna and radius) is, in turn, connected to the upper arm via a revolute joint to allow for flexion/extension of the elbow. Finally, a universal joint is used to connect the forearm to the hand, allowing the flexion/extension and abduction/adduction of the wrist joint. It is also assumed that the hand firmly grips the steering wheel; thus, hand/steering wheel interaction is modeled as a fixed (weld) joint.

The number of degrees of freedom in this model is smaller than the actual degrees of freedom in a human arm. Unlike the human arm, this model does not allow supination/pronation of the forearm. These degrees of freedom have negligible effect on the

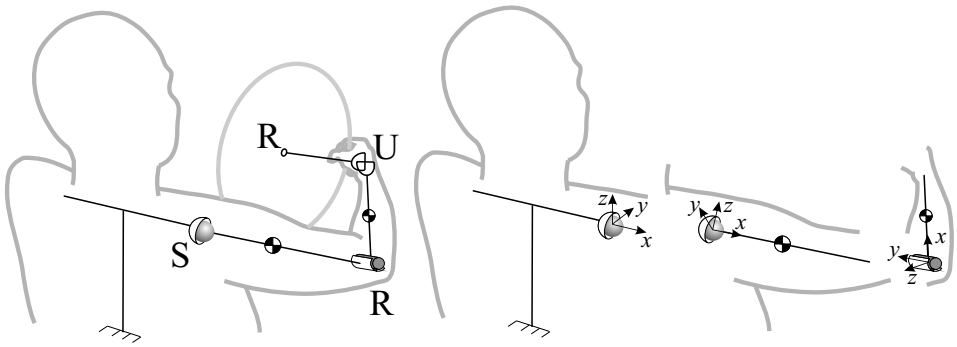

(a) (b)

Figure 4.1: (a) Schematic view of the 3D arm model. (b) Coordinate systems for each segment

kinematics of the steering act for the range of steering angle ($\pm 90°$) considered here; moreover, the associated muscles (Supinator, Pronator Teres and Subscapularis) have negligible activation during steering [111]. Such simplifications reduce the complexity of the model, while maintaining its versatility.

In total, 15 muscles are used in this model to move the arm (see Figure 4.2a); 8 and 7 of these muscles are responsible for shoulder and elbow motions, respectively. The muscles that are not included are either negligible in effect, or related to the removed degrees of freedom (e.g. supination). Moreover, in spite of significant activity of some wrist actuator muscles during steering [111], the wrist joint is left unactuated because the elbow and shoulder muscles are of the most interest. The muscle path parameters used in this work are adopted from existing research articles [111, 43, 159, 139], and are summarized in Table B.1 of Appendix B.

4.1.2 Hill-type Muscle Model

The model used to simulate the muscle dynamics is inspired from the popular Hill muscle model [139, 51]. As shown in Fig. 4.3, the Hill muscle model consists of a Contractile Element (CE) and a Parallel Elastic element (PE) in series with a Series Elastic element

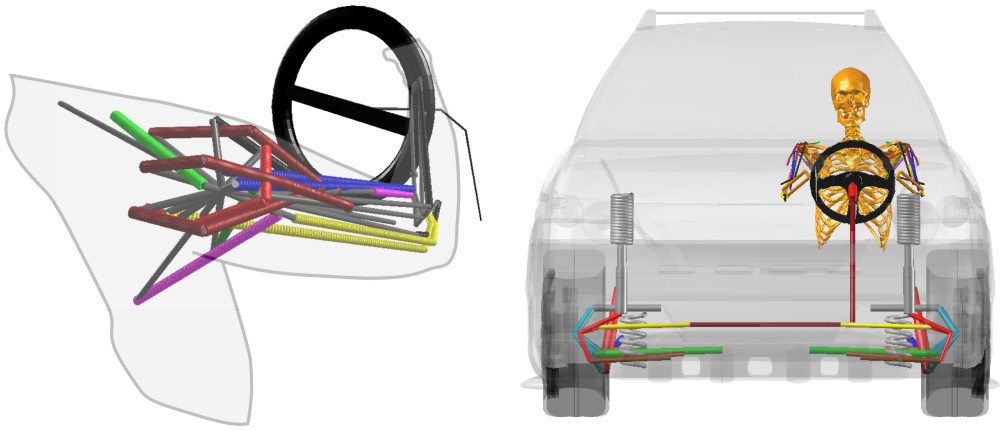

(a) (b)

Figure 4.2: The 3D arm and the vehicle models in MapleSim (a) The muscle-actuated arm model, (b) Vehicle and driver model

(SE). In this thesis, the tendon dynamics (SE) are neglected, as the motion is relatively slow, and amount of energy transfer in tendons is small. However, stiffness produced by the SE element of muscles wrapping the shoulder and elbow joints, as a result of muscle co-contraction, are approximated and replaced with a stiffness and damping at the joint. This stiffness and viscous damping increases with the muscle co-contraction as a function of the muscle co-contraction ratio. Therefore, the muscle model is reduced to the CE element in parallel with the PE element. Based on these assumptions, the muscle force can be found as follows:

$$F_{TM}(t) = F_0^{max} \left\{ F_{PE}\left(t, L_M\right) + F_{CE}(t, a, L_M, V_M) \right\} \ cos(\alpha_p) \tag{4.1}$$

where F_{PE} and F_{CE} are the passive and active forces of the muscle, respectively. L_M, V_M, α_p and F_0^{max} are the muscle length, contraction velocity, pennation angle and maximum isometric muscle force, respectively. The muscle activation (a) represents the fraction of active motor units in the muscle (between 0 and 1), and since the SE element is removed, the pennation angle for all muscles is assumed to be zero.

The force generated by the active part of muscle (CE) can be separated into force-length

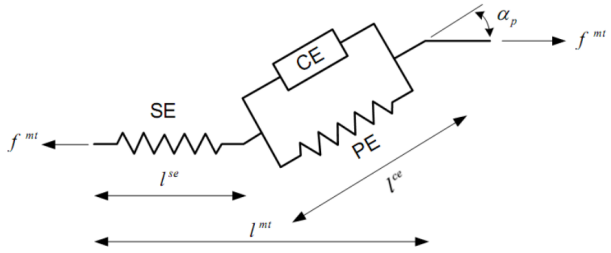

Figure 4.3: An example of a Hill-type muscle model [139]. The Hill muscle model consists of series elastic element (SE), parallel elastic element (PE) and contractile element (CE) as the active part of muscle.

and force-velocity relations [139], which is scaled by the activation level of the muscle as shown in Eq. (4.2). A schematic diagram of these two relations is shown in Fig. 4.4.

$$F_{CE}(t, a, V_M) = a\,(t)\;\; F^{L}_{CE}\,(t, L_M)\;\; F^{V}_{CE}(t, a, L_M, V_M) \tag{4.2}$$

The force-length relation is described by the normal distribution function as follows [139]:

$$F^{L}_{CE}\,(t, L_M) = \mathrm{e}^{-\left(\frac{L_M(t)}{L_M^{opt}}-1\right)^2/\gamma} \tag{4.3}$$

where the shaping factor γ is set to 0.45, and the length of muscle in the initial posture is selected as the optimal length of muscle (L_M^{opt}). The driver is holding the steering wheel at 3 o'clock position in his/her initial posture, and the steering axis is parallel to the line connecting the shoulder to the steering wheel (see Fig. 4.17a). The force-contraction velocity dependent relation is approximated by the following formula [139, 127]:

$$F^{V}_{CE} = \begin{cases} \dfrac{V_M/V_M^{max}L_M^{opt}+AV_M^{max}}{V_M/V_M^{max}L_M^{opt}A_f+AV_M^{max}} & V_M < 0 \\ \\ \dfrac{V_M B\bar{F}^{len}_{max}/V_M^{max}L_M^{opt}+ACV_M^{max}}{V_M B/V_M^{max}L_M^{opt}A_f+ACV_M^{max}} & V_M > 0 \end{cases} \tag{4.4}$$

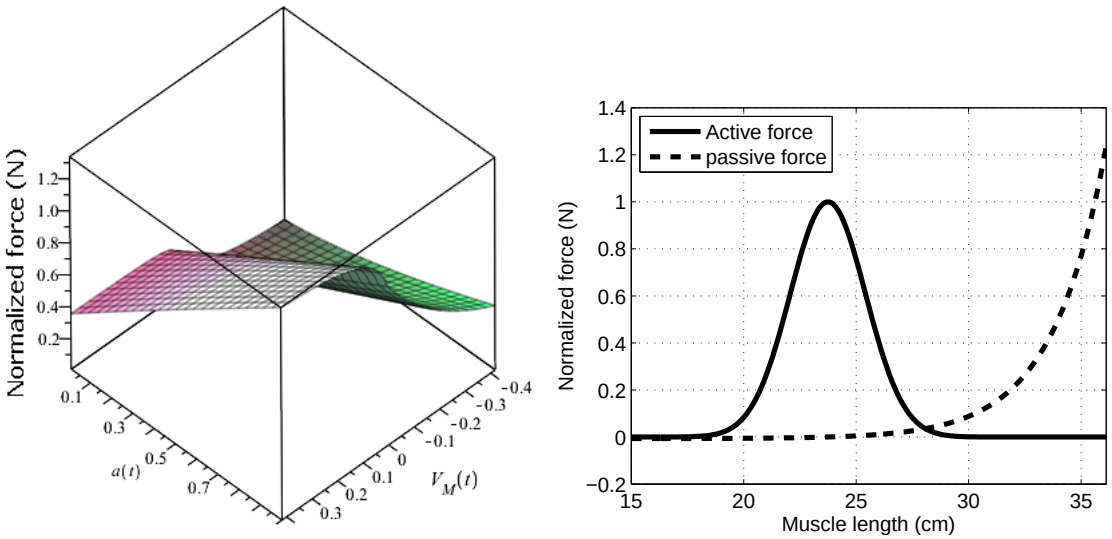

(a) (b)

Figure 4.4: (a) The relation of the muscle force-velocity dependent relation (F_{CE}^{V}) with activation, (b) The muscle force-length dependent relation of CE (active force) and PE element (passive force)

where V_M^{max}, the maximum contraction velocity of the muscle, is set to 10 (L_M^{opt}/s) and A, B and C are shape factors calculated by $A = 0.25+0.75\ a(t)$, $B = 2+2/Af$ and $C = \bar{F}_{len}^{max}-1$, respectively. $\bar{F}_{len}^{max}$, the maximum normalized muscle force achievable during lengthening, is set to 1.4 and A_f, a force-velocity shape factor, is set to 0.25.

The force-length relationship of the PE element of the muscle as shown in Fig. 4.4b is represented by an exponential function [139]:

$$F_{PE}\left(t, L_M\right) = \frac{\mathrm{e}^{k_{pe}\left(\frac{L_M(t)}{L_M^{opt}}-1\right)}/\epsilon_0^m - 1}{\mathrm{e}^{k_{pe}} - 1} \tag{4.5}$$

where k_{pe}, a shape factor, is set to 5 , and ϵ_0^m, the passive muscle strain due to the maximum isometric muscle force, is set to 0.6.

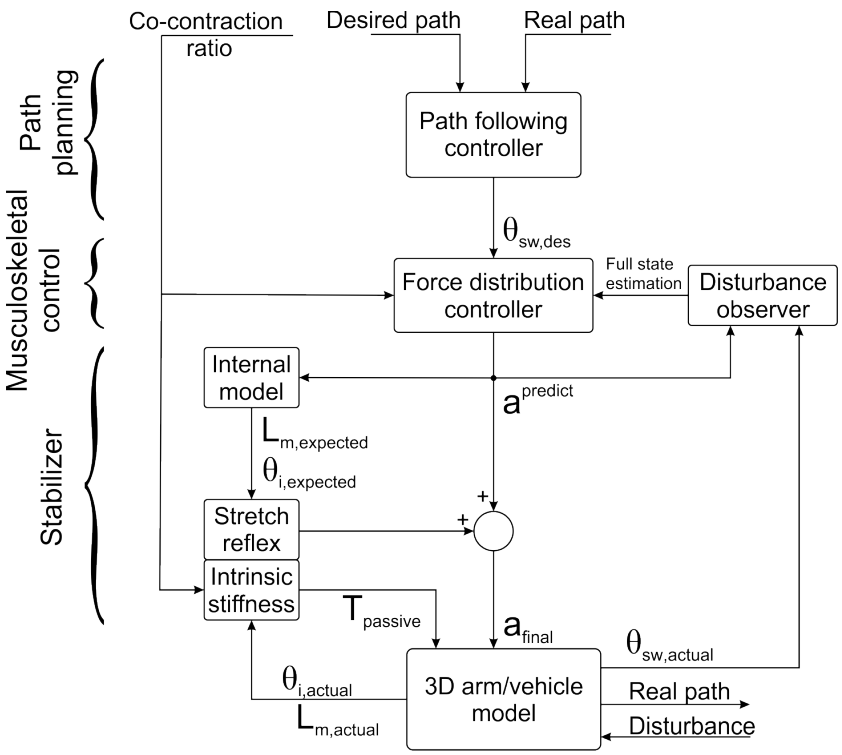

Figure 4.5: The motor control framework to study steering task

4.2 Motor Control Framework

A feature-rich motor control framework for the musculoskeletal driver model considering the sensory and actuator dynamics of human limb has been developed to study the driver/vehicle interaction. In humans, the CNS comprises information processing in the brain, the cerebellum and the neural circuits of spinal cord, to modulate motor commands and control the voluntary and the involuntary actions of the driver.

To reliably study motor action tasks, we need to establish a predictive framework with sufficient bio-fidelity. With the motor control framework presented in this thesis, we can define an environment (which may include disturbances and uncertain dynamics) and a desired steering action, run the simulation, and observe the consequences. Such a model can help to study steering tasks and design new driver-assistance technologies.

As shown in Fig. 4.5, the proposed motor control framework consists of three parts: the path planning part, the musculoskeletal control part, and finally the stabilizer part. The path planning controller (level one of control hierarchy) works in the low-dimensional end-effector space (in this context the steering wheel angle); it defines a desired steering wheel trajectory, $\theta_{sw,des}$, based on its internal representation of the system. The musculoskeletal controller (level two in the hierarchy), works in the high-dimensional muscle space, and tries to predict the muscle activation, $a^{predict}$, required to follow the high-level controller's set points. In the stabilizer part, the stretch reflex (the lowest level in the hierarchy) also works in high-dimensional muscle space, and the intrinsic stiffness module works in the joint space. The lowest level of hierarchy is responsible for compensating for inaccuracies and disturbances in the system.

4.2.1 Level One – Model Predictive Path Planning Controller

The first layer of the framework, the path planning part, estimates the required steering wheel angle to perform a specific task, and is represented by a model predictive controller (MPC) [23, 90].

As argued by Kim and Cole [65], the cerebellum may contain representations of the nonlinear body/vehicle dynamics, in the form of a set of linear models (internal models). The versatility of this set shows the driver steering skill, which results in better performance of the driver in the near-limit conditions. In this thesis, a single linear model is used to represent the driver's steering skill. Since all the predictions in the MPC are based on this internal model, this model is of great importance. For this reason, the validated nonlinear internal model of vehicle (as defined in section 3.3, a bicycle model of vehicle with non-linear tire model) is linearized at the equilibrium tire slip angles ($\alpha_f = \alpha_r = 0$) to be used in the MPC path-following controller. Therefore, the internal model is reduced to a linear bicycle model with a linear tire model (control-oriented model). The control-oriented model captures the significant dynamics of the yawing and lateral motion of the vehicle. Figure 4.6b shows the comparison of the lateral response to a sweep sinusoidal steering wheel angle (shown in Fig. 4.6a) for the high-fidelity and this internal control-oriented

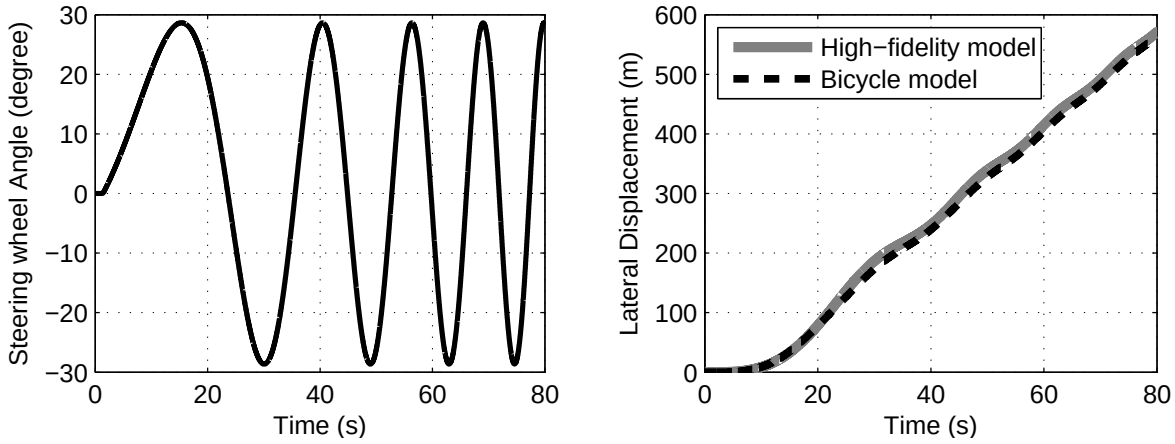

(a) (b)

Figure 4.6: System response for the high fidelity vehicle and the bicycle model (a) The steering wheel angle as the input to the systems, (b) The lateral position as the output of the systems

model at a constant speed of 10 m/s.

The MPC path planning controller tries to predict the best steering wheel trajectory by solving an optimization problem. The cost function to minimize is defined by Eq. (4.6).

$$J_{PF} = \sum_{i=1}^{n_p} \left\{ c_1 \left(y(i) - y_{des}(i) \right)^2 + c_2 \left(w_z(i) - w_{z,des}(i) \right)^2 \right\} + \sum_{i=1}^{n_c} c_3 (\theta_{sw}(i))^2 \tag{4.6}$$

where n_p and n_c are the prediction and control horizon lengths, and θ_{sw}, y, w_z, y_{des} and $w_{z,des}$ are the steering wheel angle, vehicle's lateral position, yaw rate and their desired values, respectively. Lastly, c_1, c_2 and c_3 are weighting factors in the cost function, which requires that the vehicle follow the desired path (first term), with as little steering as possible (the second term).

In this implementation of MPC, the time is discretized into 10 ms intervals, in which the control inputs (the steering wheel angle) are assumed to be constant. MPC finds the optimal sequence of control input (with the control horizon length) over the prediction

horizon length resulting in the optimal tracking performance. Then, the MPC selects the initial element of the sequence and applies it to the high-fidelity model.

To study the effect of prediction and control horizon lengths on the path planning performance of the driver model, two simulation studies using the control-oriented model are performed. In these simulations, a step signal with amplitude of 3 m is set as the desired lateral trajectory of the vehicle, as shown in Fig. 4.8. Since the desired trajectory is a sharp step signal, the path planning controller should plan to begin steering earlier than when the step arises. This behavior of MPC clearly shows the predictive path planning ability of the driver model. In the first set of simulations, the prediction and control horizons of the MPC controller are kept identical, and raised from looking 1 s ($n_p = n_c = 100 \times 0.01 = 1$ s) ahead of the vehicle to 3 s ($n_p = n_c = 300 \times 0.01 = 3$ s), consecutively. Figure 4.7 shows the steering wheel angle calculated by the MPC to perform the lane change maneuver. It can be seen that with the prediction horizon of 1 s, the driver model cannot manage to perform the lane change in the specified time. By increasing the horizons, the perfect lane change is achieved. As shown in Fig. 4.8, with prediction horizons over the 2.5 s, the vehicle actual path does not change significantly. Therefore, 2.5 s is chosen as the prediction horizon length in the remaining of this thesis.

In the second set of simulations, to study the influence of control horizon on the performance of controller, the prediction horizon kept constant and equal to 2.5 s while the controller horizon increases gradually. As shown in Fig. 4.10, with a single interval control horizon ($n_c = 1 \times 0.01 = 0.01$ s, this case reproduces results similar to MacAdam optimal controller [23]), the performance of controller is degraded; nonetheless, the closed-loop system is stable. By increasing the control horizon, the performance of controller converges to the case with full length control horizon; however, the increase more than 0.25 s only slightly improves the performance of the controller, while notably increases the computational expense. Figure 4.9 shows the required steering wheel angle to perform the lane change maneuver corresponding to the varied prediction control length. Therefore, in our path planning MPC, the prediction horizon length is 250 intervals ($250 \times 0.01 = 2.5$ s) and the control horizon length is 25 intervals ($25 \times 0.01 = 0.25$ s). The prediction horizon is long-enough that it covers the delay associated with the cognition of the road changes.

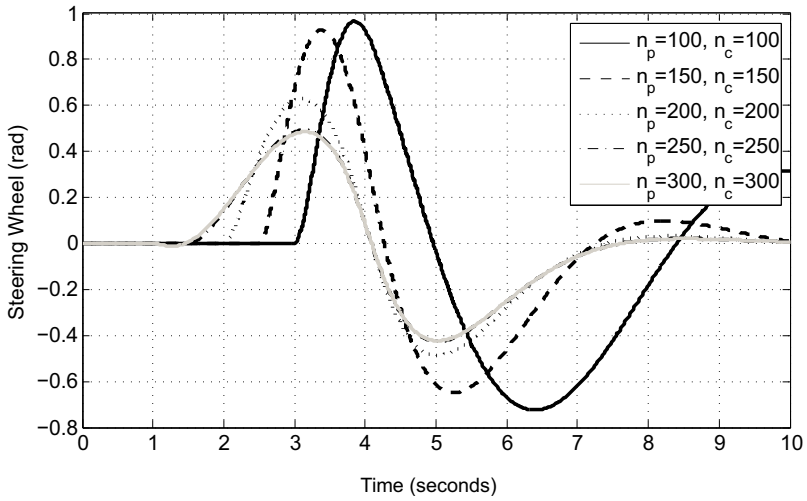

Figure 4.7: The effect of prediction and control horizon of MPC path planning controller on the steering wheel angle

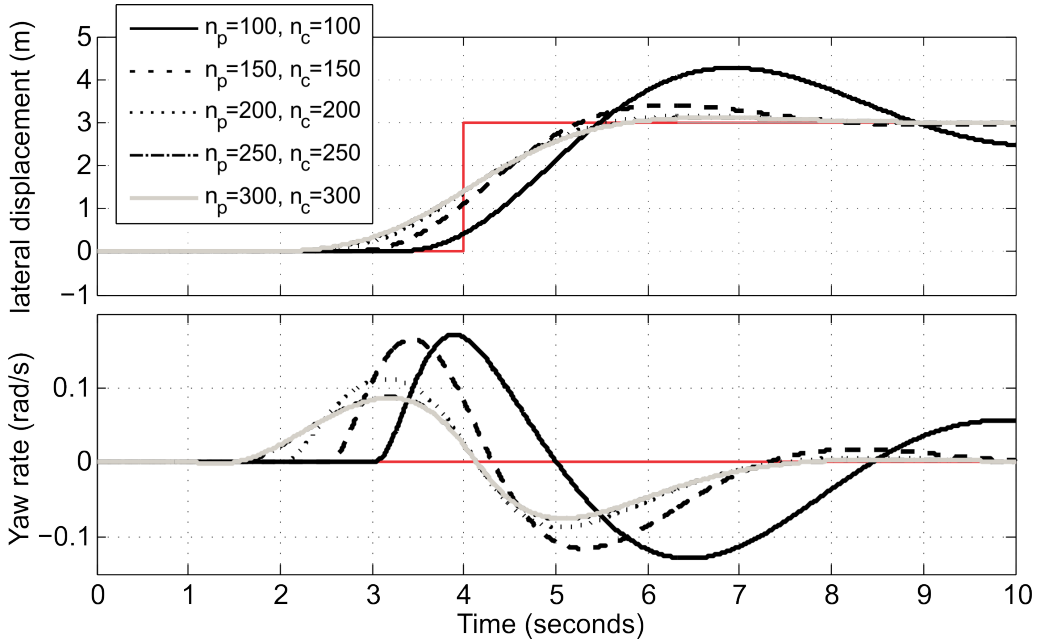

Figure 4.8: The effect of control and prediction horizon lengths of MPC path planning controller on the vehicle actual lateral displacement and yaw rate

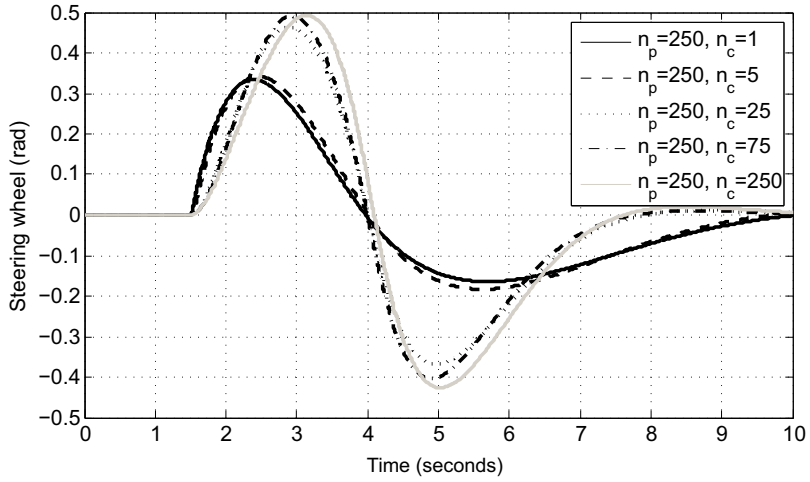

Figure 4.9: The effect of prediction and control horizon of MPC path planning controller on the steering wheel angle

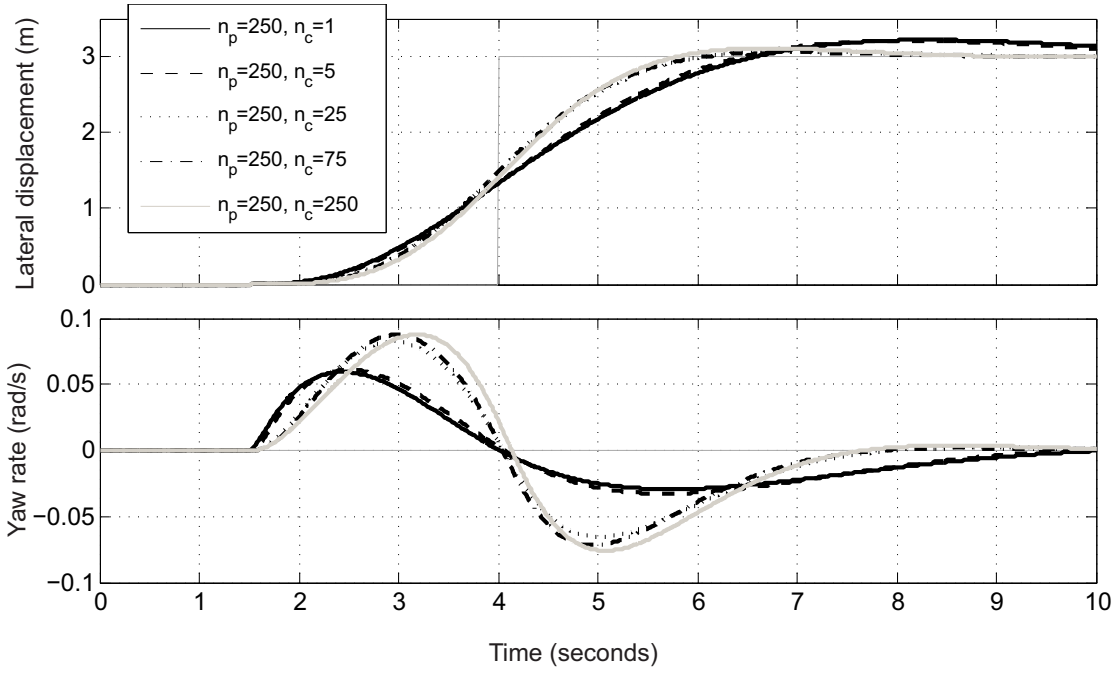

Figure 4.10: The effect of control horizon length of MPC path planning controller on the vehicle actual lateral displacement and yaw rate

4.2.2 Level Two – Force Distribution Controller and Disturbance Observer

The second layer of the motor control framework, the musculoskeletal control, includes the Force Distribution (FD) controller and the disturbance observer. This layer represents the process of information collection from the sensory organs and the control of conscious voluntary actions of the upper limb.

In this thesis, the FD controller assigns the required muscle activations to perform a specific arm motion. The development of the FD controller has been inspired from a well-known motor control hypothesis: it postulates that the CNS minimizes a physiological cost function while performing a motion. However, the configuration and states of the body should be known to the CNS/FD controller to find the optimal muscle forces. Therefore, an observer is added to the system to estimate the state variables during the motion. In the presence of disturbances, the disturbance observer identifies the disturbance and predicts the altered state variables. However, the FD controller response to disturbance has a relatively long latency due to biological delays in signal processing.

4.2.2.1 Force Distribution Controller

Similar to the path planning controller, the system behavior (steering wheel rotation as a result of the muscle activity) is predicted by an internal representation of the system, called the vehicle-driver internal model. Here, the internal model of vehicle (section 3.3) in conjunction with the 3D model of arm (section 4.1.1) is selected as the vehicle-driver internal model. However, to incorporate steering skill into the internal model, the vehicle model is linearized at zero slip angle. Consequently, the vehicle-driver internal model set consists of a single member, a 3D arm model holding the steering wheel at 3 o'clock position and a resistive torque calculated using the control-oriented model from section 3.3. The resistive steering torque (SAT) can be calculated from Eq. (3.20).

This resistive torque can be approximated with a passive torque (spring and damper) at the steering column. Figure 4.11b demonstrates the comparison of the passive torque

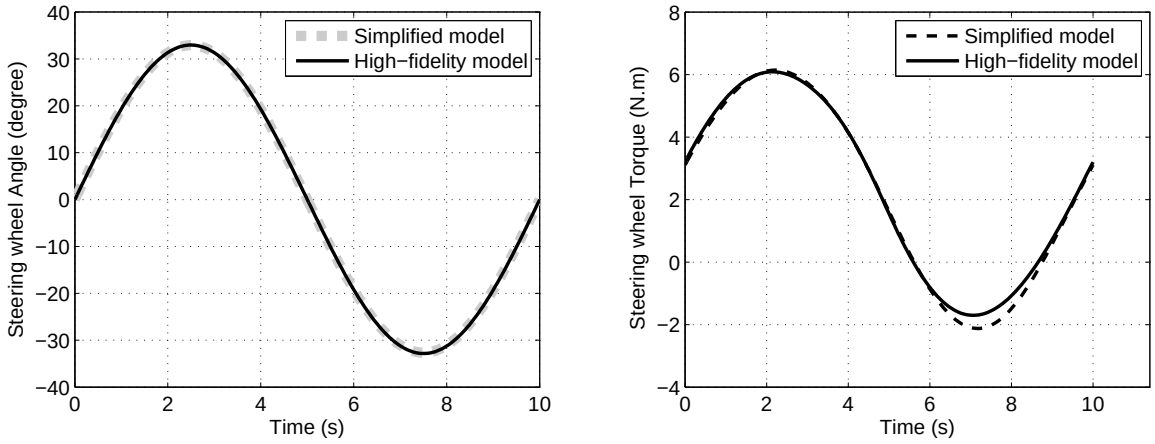

(a) (b)

Figure 4.11: Simplified model resistive steering torque for a sinusoidal steering angle trajectory, compared against the high fidelity model. In the high-fidelity model, the right hand of the driver is holding the steering wheel at 3 o'clock position.

and high-fidelity model of vehicle and arm (in terms of the resistive torque). In this figure, the resistive steering torque is shown when the steering wheel angle follows a sinusoidal trajectory (see Fig. 4.11a). Therefore, to accelerate the simulations, the passive torque is used (instead of the control-oriented model) along with the 3D model of arm as the internal model. The passive resistive torque at the steering wheel, T_{sw}, is given by

$$T_{sw} = K_{sw}\theta_{sw} + C_{sw}\dot{\theta}_{sw} \tag{4.7}$$

where the stiffness, K_{sw}, and the damping coefficients, C_{sw}, are found so that the internal model response matches the real vehicle dynamics as closely as possible within the range of interest. K_{sw} and C_{sw} are functions of vehicle driving condition such as vehicle speed, road coefficient of friction, etc.

The output of the path-following controller is the low-dimensional value for the steering wheel angle $\theta_{sw,des}$. To perform the steering task, the desired steering wheel angle must be transformed into the high-dimensional muscle activation space. The major challenge associated with such transformation is the inherent redundancy of the problem (there are

more actuators than required). The redundancy issue can be addressed by including a separate criterion when solving for the muscle activations $a^{predict}$. Such criteria are usually chosen to minimize a form of the physiological cost (such as muscle force or muscle fatigue) while maintaining the desired response.

In this thesis, the force distribution controller minimizes the muscle activations according to the physiological cost function [41], as shown in Eq. (4.8).

$$G(\mathbf{a}) = \sum_{i=1}^{n} (a_i - \alpha_i)^p \tag{4.8}$$

where the symbols a_i and α_i represent the individual muscle activations, and the muscle co-contraction ratios, respectively. The exponent p is chosen to be 2 in the simulations. The summation accounts for all muscles ($n = 15$).

Additionally, since our motor control framework is a forward dynamic simulation (i.e. the applied forces generate the motion), tracking the desired motion is challenging. To ensure that the applied forces result in the desired motion, the tracking error is also included as a separate term into the FD controller cost function.

$$a_i^{predict}[k] = \arg\min \left\{ w_1 \left(\theta_{sw}[k] - \theta_{sw,des}[k]\right)^2 + w_2 \; G(\mathbf{a}[k]) \right\} \tag{4.9}$$

where $\theta_{sw}[k]$ is the resultant steering wheel at time step k, which is compared against the desired value ($\theta_{sw,des}[k]$, defined by the path-following controller), and w_1 and w_2 are the weighting factors in the cost function.

The minimization can be performed at each time step (Forward Static Optimization [129]) or over the entire time span (Dynamic Optimization [5, 128]). In this research, the former approach is selected. At each time step, the force distribution controller solves a constrained optimization problem to minimize both the physiological effort and the tracking error (Eq. (4.9)), while keeping the activations in the range $a_i \in [0, 1]$.

The sequential quadratic programming (SQP) optimization routine is used to solve this optimization problem. Figure 4.12 shows the performance of the second layer of motor

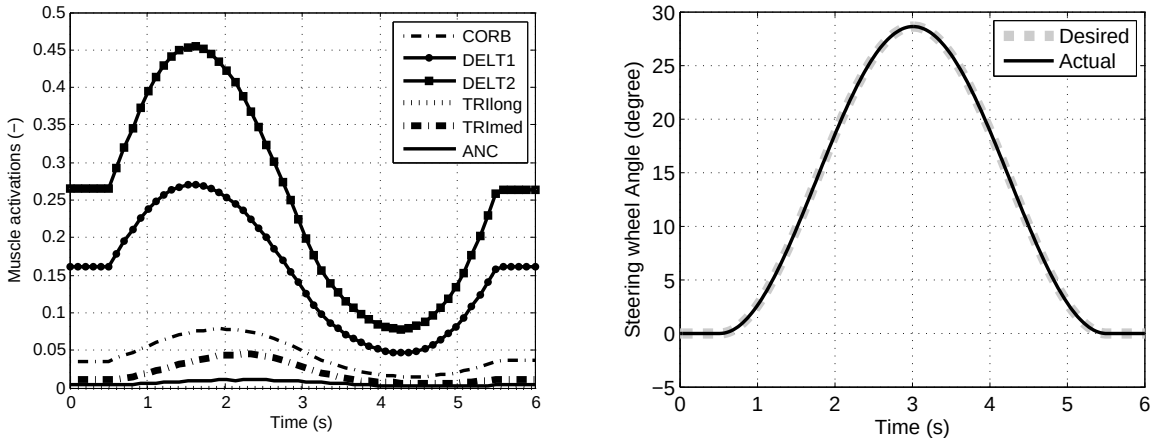

(a) (b)

Figure 4.12: Force distribution controller performance (a) The muscle forces calculated by the controller, (b) The desired and actual steering wheel angle

control framework in steering with the right hand only, in which Fig. 4.12a shows the required muscle forces to follow the steering wheel trajectory in Fig. 4.12b. The anterior and middle part of deltoid muscle (DELT2, DELT1) and coracobrachialis muscle (CORB) are used to abduct and then adduct the shoulder and long and medial head of triceps, and the anconeus muscle (ANC) has been used to extend and then flex the elbow. No antagonist muscle is activated in this simulation because gravity helps the driver to return the steering wheel to its original position.

4.2.2.2 Disturbance Observer

The FD controller needs the state variables of the steering and arm dynamics to predict the optimal muscle activations. A disturbance observer is used to estimate the arm and steering state variables as well as the disturbance torque at the steering wheel. In this thesis, the disturbance observer is used to replace the predictor/corrector process of the CNS internal model structure to estimate the limb position. If there is no disturbance in the system, the estimated states are similar to the actual states of the system, since they have started from the same initial condition and have similar dynamics. In this situation,

the identified disturbance torque accounts for the difference between the internal model (passive torque) and the actual resistive steering torque.

However, when the system states are altered by an external disturbance, there is an error in the estimated states. To correct this error, a feedback loop on the steering wheel position is added to the observer to identify the disturbance and predict the altered states, as shown in Fig. 4.13a. However, there is a delay associated with vestibulo-ocular and signal processing to represent the difference between the expected and actual steering wheel angle.

To summarize, the feedback estimator is a proportional and integral controller with a time delay to identify the applied external disturbance at the steering wheel and predict the altered state variables required for the force distribution controller. Therefore, the response of the disturbance observer/force distribution will lead to a response with latency in the voluntary range. The transfer function of the feedback loop used to identify the disturbance torque is,

$$H^e = \frac{T_{\text{disturbance}}(S)}{\Delta\theta_{\text{sw}}(S)} = \left(K_p^e + \frac{K_i^e}{S}\right) e^{-\tau_d^e S} \tag{4.10}$$

where $T_{\text{disturbance}}$ and $\Delta\theta_{\text{sw}}$ are the estimated disturbance torque and the steering wheel angle error between actual and estimated, and K_p^e and K_i^e are the proportional and integral coefficients, respectively and τ_d^e is the time delay associated with the biological signal processing.

Figure 4.13b shows the performance of the disturbance observer to identifying a disturbance torque at the steering wheel. In this simulation, the car is driving in a straight line when a sudden unknown disturbance is applied to the car, which results in a pulse shape steering torque at the steering wheel. The observer starts to identify the disturbance after 300 ms, reaches the actual disturbance after one second, and then returns to zero again.

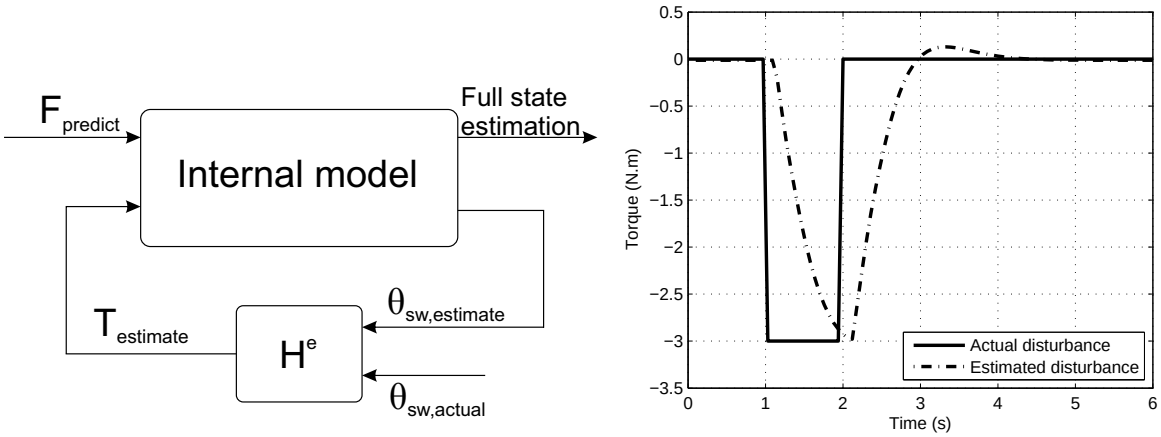

(a) (b)

Figure 4.13: Disturbance observer mechanism and performance (a) The mathematical realization of the disturbance observer in the motor control framework, (b) The disturbance torque at the steering wheel estimated by the disturbance observer

4.2.3 Level Three – Stretch Reflex/Intrinsic Stiffness

The third layer of the motor control framework, the stabilizer layer, stabilizes the limb and reduces the error introduced by external disturbances. This layer includes the stretch reflex and the intrinsic stiffness mechanisms. The stretch reflex uses the muscle proprioceptive feedback of the muscle spindles to regulate the muscle length, and the intrinsic stiffness modulates the visco-elastic properties of the muscles by co-contracting muscles wrapping a joint to stand against external disturbances.

The involuntary response due to stretch reflex occurs more quickly than the voluntary actions. In spite of the difference in their nature and response time, both the involuntary stretch reflex and the voluntary co-contraction contribute to movement stabilization.

4.2.3.1 Stretch Reflex

The sensitivity of the stretch reflex and its effectiveness in the rejection of unexpected motions can be modulated by the high centres of the CNS, via modulation of the γ-motor neu-

ron activities [3, 141]. During a voluntary action, the nervous system has expected settings for muscle lengths; such expected lengths are set by adjusting the muscle spindle sensitivity, which in turn is done by modulating the γ-motor neuron activities. If due to a change in environment, the muscle length diverges from the expected value (say over-stretched), the Ia afferent activity will increase. Because of the excitatory synapse between the Ia afferent and α-motor neurons, such increase in Ia activity will boost the α-motor neuron activity which results in more muscle force that resists the muscle stretch. The stretch reflex can therefore provide disturbance rejection properties. In this research, the short-loop monosynaptic spinal stretch reflex is considered as the most effective mechanism for disturbance rejection and the transcortical (long-loop) stretch reflex is neglected. Figure 4.14 presents a schematic of the stretch reflex mechanism in a human, and its block diagram replication in our model.

The response of the muscle spindles to a change in the muscle length can be considered as a nonlinear summation of the muscle length and muscle contraction velocity, and there is a delay associated with the response [49, 95] according to the transfer function:

$$H^{sr} = \frac{a_{muscle}(S)}{L_{muscle}(S)} = \left(K_p^{sr} + K_d^{sr} S\right) e^{-\tau_d^{sr} S} \tag{4.11}$$

where L_{muscle} and a_{muscle} are individual muscle length and activation, and K_p^{sr}, K_d^{sr} and τ_d^{sr} are the proportional and derivative coefficients and the delay associated with short-loop stretch reflex mechanism, respectively.

The expected muscle length is found from the response of the internal model to the predicted optimal muscle activations (within the FD controller, see Figure 4.5). For each muscle, the error between the expected length from the actual length is calculated, and then multiplied by H^{sr} to find the amount of corrective activation. It is then added to the original activation command to drive the muscle (see Figure 4.14b).

Figure 4.15 shows the disturbance rejection capabilities of the reflex loop. Figure 4.15a shows that the driver tries to keep the steering wheel stationary, when the disturbance torque as described in section 4.2.2.2 (see Figure 4.13b) is suddenly applied to the steering wheel. Figure 4.15b shows the middle part of deltoid muscle response to the disturbance

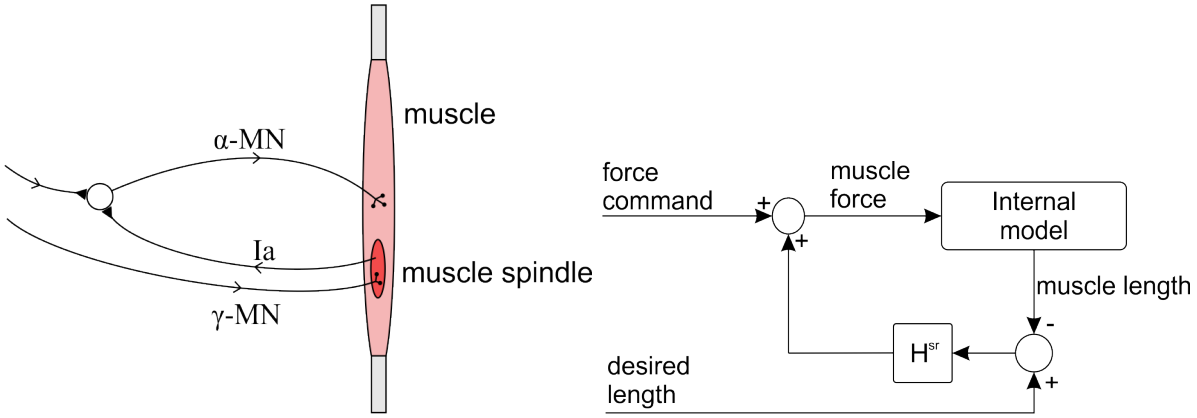

(a) (b)

Figure 4.14: Stretch reflex mechanism and performance (a) The schematic of the stretch reflex loop in humans, (b) The mathematical realization of the stretch reflex in the arm model

to stabilize the steering wheel. It can be seen that the stretch reflex responds quickly when the disturbance occurs but it takes more time for voluntary contribution of the CNS to notice, identify, and resist the disturbance.

4.2.3.2 Intrinsic Stiffness

Joint stiffness (impedance) modulation is another strategy employed by the CNS to resist external disturbances. This strategy works against all sorts of perturbations, but it is highly energy consuming. The voluntary contribution to the joint stiffness and impedance has roots in the structure and properties of muscle during co-contraction.

It is shown in [154] that the intention to resist external disturbance is well correlated to the antagonistic co-contraction ratio. Likewise, the muscle co-contraction can represent the driver's steering skill or the concentration of the driver on the path. In this thesis, the equilibrium-point hypothesis [37] has been used to regulate the intrinsic properties of joints. Feldman proposed that the net passive moment at the joint is a function of joint angle and the equilibrium point, and the CNS manipulates the equilibrium point by adjusting the antagonistic co-contraction [37].

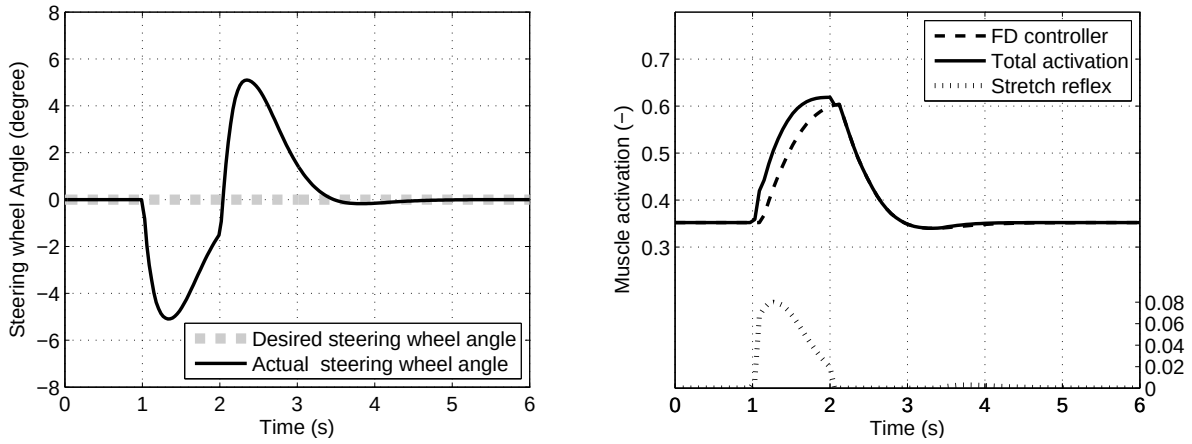

(a) (b)

Figure 4.15: Disturbance rejection properties of the stretch reflex (a) Actual and desired steering wheel angle, (b) The middle part of deltoid muscle force. The three graphs are the force distribution controller prediction, the stretch reflex addition and the total muscle force

Since in the implementation, the SE element of Hill-type muscle model is not included, a moment is added to the joints to represent the intrinsic properties of the muscles wrapping the joint. This moment is the function of the deviation of the actual 3D direction of shoulder/elbow from its expected value (from the forward model, Figure 4.5) and the muscle co-contraction ratio as illustrated in Eq. 4.12,

$$\bar{T}_i^{IS} = \alpha \ (K_i^{IS}\theta_i + C_i^{IS}\dot{\theta}_i) \ \bar{n} \tag{4.12}$$

where α is the muscle co-contraction ratio and θ_i and $\dot{\theta}_i$ are angle and angular velocity difference between the expected and actual shoulder/elbow directions. The passive moment is in the direction $\bar{n}$ which is the unit vector normal to the error plane, and is constructed using the cross product of the actual and expected direction vectors as shown in Fig. 4.16a.

Figure 4.16b shows the passive joint moments produced by intrinsic properties of muscle when the muscle co-contraction ratio is assumed to be 30%, in the scenario described in 4.2.2.2.

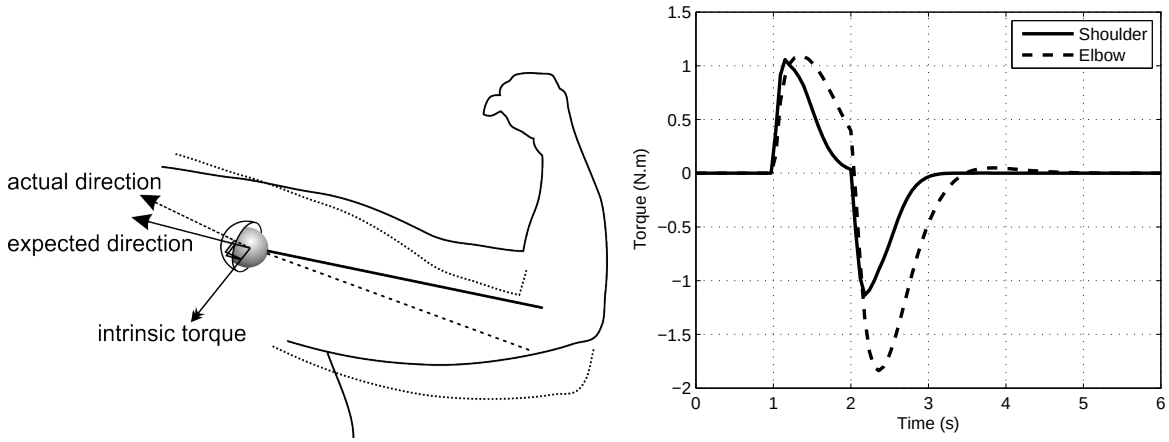

(a) (b)

Figure 4.16: (a) Sketch of the joint stiffness mechanism, (b) The passive joint moment produced by intrinsic properties of the muscles (reference frame as shown in Figure 4.1a).

4.3 Evaluation of Active Properties of Musculoskeletal Driver Model

To develop a realistic driver model, and to secure the interpretation of neuromusculoskeletal dynamics of the driver's arm model, the muscle functions of the 3D arm model are validated against experimental data [89].

The first study on the upper limb muscles function on the automotive steering task has been conducted by Jonsson and Jonsson (J&J) [60, 58, 59] in 1975 using electromyography (EMG). They studied the functionality of shoulder, elbow and trunk muscles in the steering task by performing a controlled condition experiment on a driving simulator with two hands on the steering wheel. However, no experimental measurements were disclosed, and only the functionality of muscles were discussed. Later in 2006, Pick and Cole [114] chose eight muscles based on J&J publications and studied the EMG activity of driver arm muscles to investigate the muscle functionality and the relation between muscle EMG and steering torque. Similarly in 2013, *JTEKT Corporation* researchers [50, 80, 98] captured the EMG activity of ten arm muscles while performing the steering maneuver with only right hand

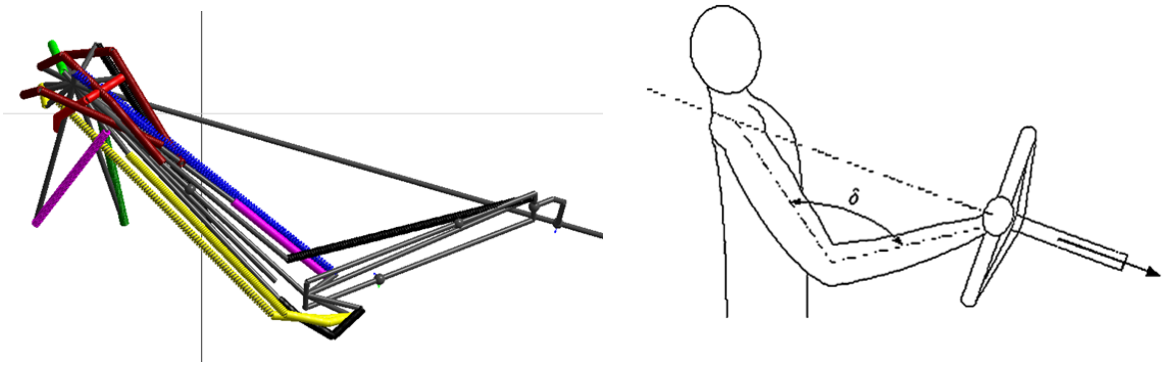

(a) (b)

Figure 4.17: (a) Schematic view of the 3D arm model. (b) Experimental setup [50]

for a larger population of drivers. In this thesis, the EMG signals of the right arm from the latest research [50] have been used to evaluate the 3D arm model, while the other papers have been used to adjust the differences.

Two steering maneuvers, similar to the experiments described by Hayama et al. [50], are performed by the 3D arm model, and the predicted muscle activations are compared to the EMG signals from the experiments. The muscle activation signal is the muscle's detected EMG voltage normalized by its maximum voluntary contraction value. However, the EMG signals from [50] are not normalized; therefore, for the model evaluation, EMG signals are scaled to match the predicted muscle activations. In these experiments, the steering wheel and seat are adjusted in a way that the line from shoulder to steering wheel center is parallel to steering axis, and the driver's elbow angle is about 100° and the hand is at 3 o'clock position, as shown in Fig. 4.17b.

In the first maneuver, the driver holds the steering wheel stationary against a triangular-waveform steering torque as shown in Fig. 4.18a, while in the second maneuver, the driver performs a sinusoidal steering with amplitude of 60° and frequency of 2 rad/s, as shown in Fig. 4.18b. Both experiments are equally important for evaluation of the driver model. The first experiment simulates the on-center handling situation, where the driver steers in a straight line and the road irregularities generate a disturbance torque at the steering wheel,

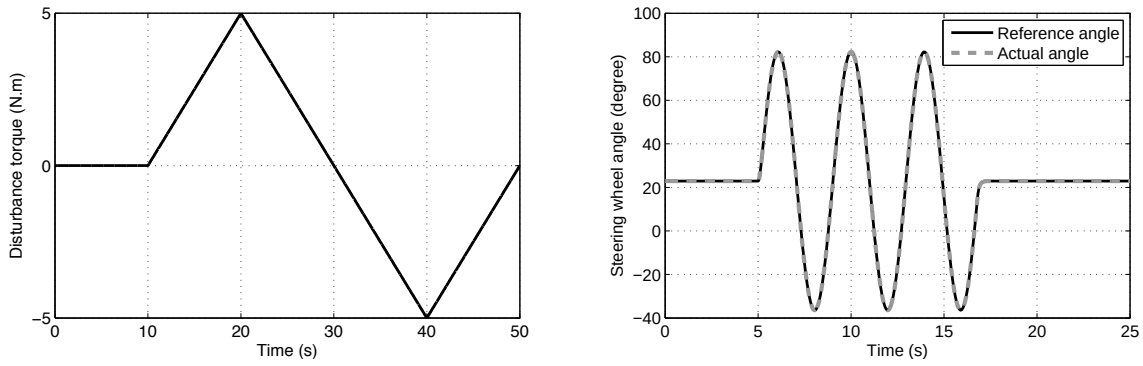

(a) (b)

Figure 4.18: (a) The triangular-wave form steering torque in the disturbance rejection experiment, (b) The steering wheel angle in the slalom steering maneuver experiment

and the second experiment represents a regular steering task such as slalom maneuver.

From the fifteen muscles modeled in the 3D arm model, electromyographic activity of eight muscles have been measured in the experiments. As shown in Fig. 4.20, in the disturbance rejection experiment, the predicted muscle activations found from the 3D arm model are closely correlated with the experimental data. However, the EMG signal of the posterior deltoid muscle shows two bursts (see Fig. 4.20g) while the model predicts only one burst. The second burst could be the result of EMG signal crosstalk from the middle and anterior portions of deltoid. Surface EMG crosstalk is the EMG signal detected over a non-active muscle generated by a nearby muscle. This explanation is consistent with foundings in [60, 98] where they consider the posterior deltoid as a synergist to the muscles resisting the negative steering torques (although Pick and Cole consider it as synergist to muscles assisting the negative steering torques). Similarly, the lateral head of triceps brachii is activated over the whole disturbance duration, while the predicted activation is only active at the negative disturbance torque. This could be result of either crosstalk signal detection or the high co-contraction ratio of elbow muscles in the experiments.

Figure 4.21 depicts the model muscle activation predictions and the EMG signals in the sinusoidal steering maneuver. In this simulation, since the muscle length and contraction velocity change during the maneuver, the muscle dynamics effect is more noticeable than

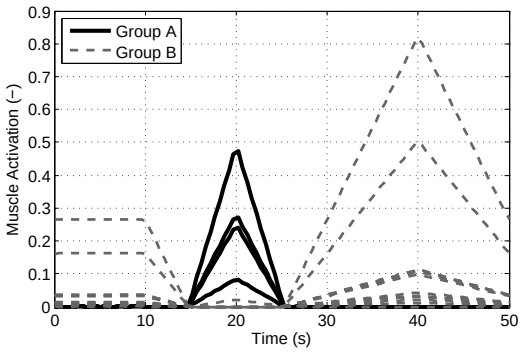

Figure 4.19: Muscle groups for the active experiment

isometric contraction. Although a simplified muscle model is used in the 3D arm model to simulate the muscle dynamics, the correlation between experiments and model predictions are fairly consistent.

Figure 4.19 shows that the muscle functions can be easily classified into two groups: the muscles generating the clockwise torque and muscles generating counterclockwise torque. Latissimus dorsi, brachialis and posterior deltoid muscles act as synergist muscles to their already known agonist muscle, long head of triceps brachii, to resist the negative steering torque (Group CW), while the second group (Group CCW) hires more muscles such as anterior and middle portions of deltoid muscle and pectorials major muscles to resist the positive steering torque. The muscle functions for steering with only right hand is summarized in table 4.1.

Table 4.1: List of muscles producing torque in the clockwise and counterclockwise direction in the first maneuver

Clockwise torque	Counterclockwise torque
Anterior deltoid	**Long head of triceps**
Middle deltoid	Posterior deltoid
Pectoralis major	Latissimus dorsi
Infraspinatus	Brachialis
Short head of biceps	
Medial head of biceps	

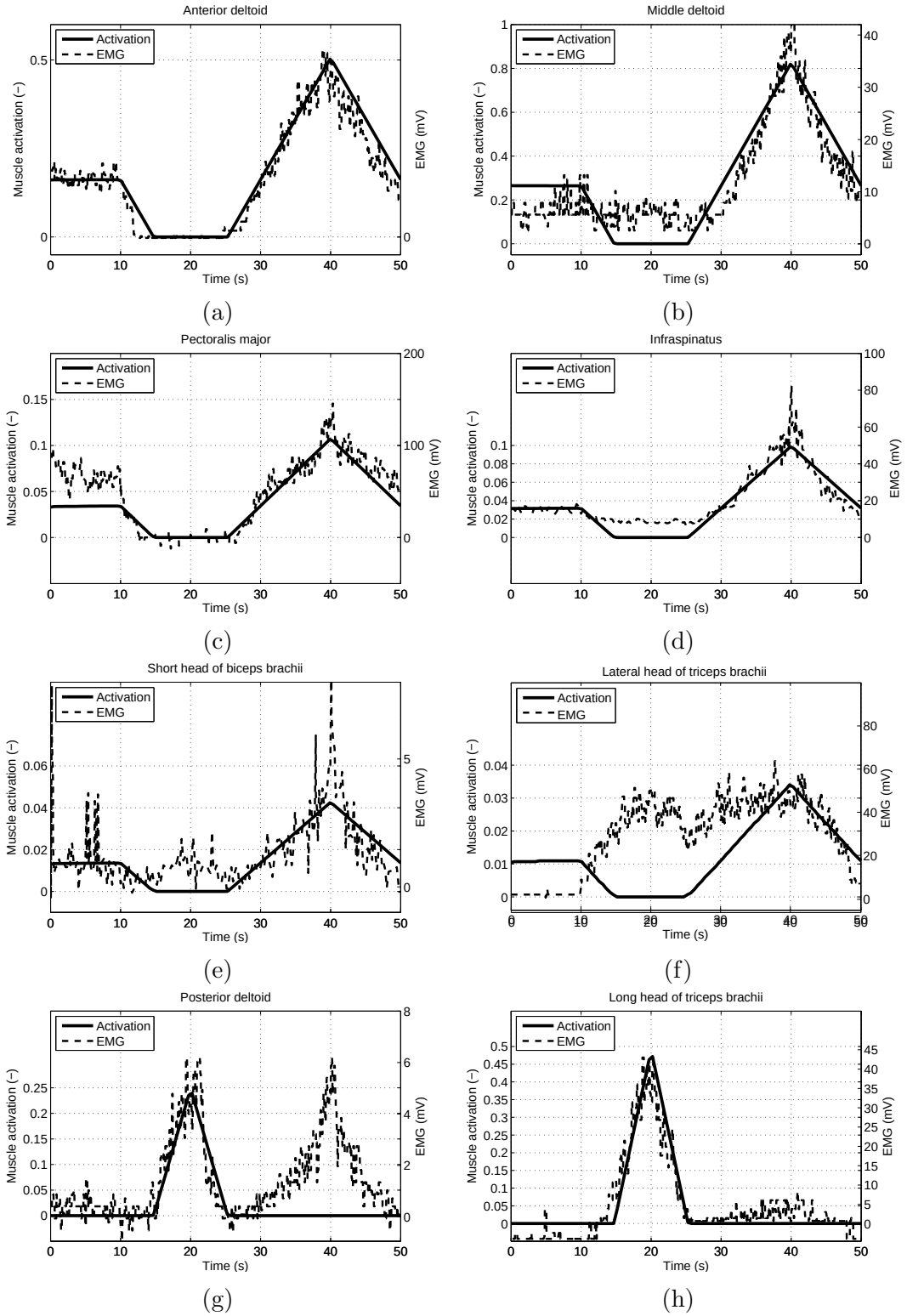

Figure 4.20: Electromyography signal and optimal muscle activation comparison for the disturbance rejection maneuver (a) Anterior deltoid, (b) Middle deltoid, (c) Pectorialis major, (d) Infraspinatus, (e) Long head of biceps brachii, (f) Lateral head of triceps brachii, (g) Posterior deltoid, (h) Long head of triceps brachii

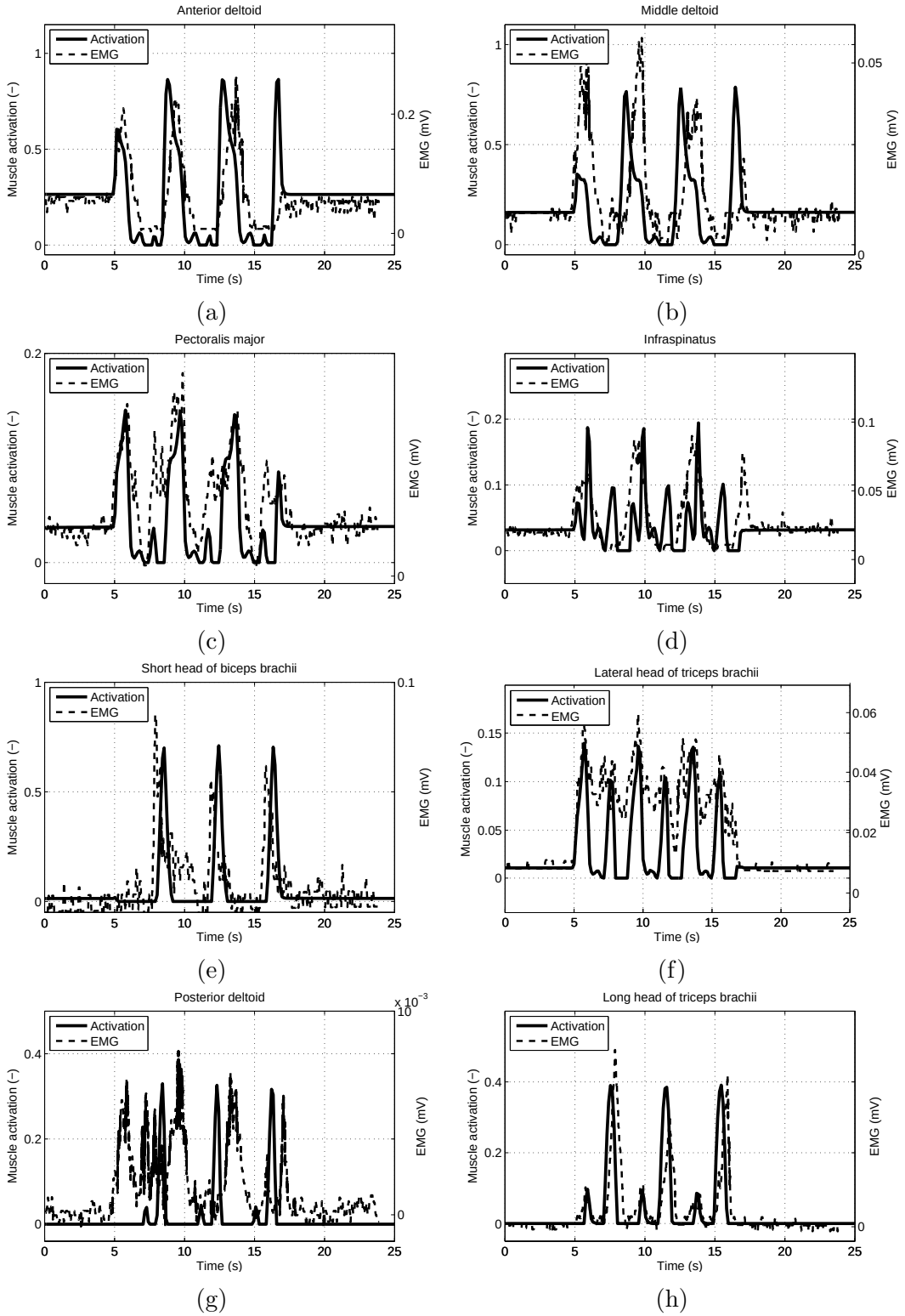

Figure 4.21: Electromyography signal and optimal muscle activation comparison for the slalom-like steering maneuver (a) Anterior deltoid, (b) Middle deltoid, (c) Pectorialis major, (d) Infraspinatus, (e) Long head of biceps brachii, (f) Lateral head of triceps brachii, (g) Posterior deltoid, (h) Long head of triceps brachii

4.4 Steering with Two Hands

Since the validity of the driver's right arm model is verified, to study a realistic driving condition, the second arm (left arm) is developed and attached to the steering wheel at the nine o'clock position. The muscles and bones of the left arm are developed in way a that the driver model becomes symmetrical as shown in Fig. 4.22a. In this model, thirty muscles are used to actuate the driver's arms and to finally turn the steering wheel, and the plausible range of steering motion without replacing the hands is -90° to +90°.

To study the dynamics of steering with two hands, a sinusoidal steering maneuver is performed with this 3D driver model, as shown in Fig. 4.22b. As expected, the shoulder muscles make the major contributions to steering. Figure 4.23 illustrates the right and left shoulder muscle activations to perform the mentioned steering task. As shown in Figs. 4.23a and 4.23b, the shoulder muscles can be classified on the basis of steering torque into the muscles providing the counterclockwise steering torque (group I) and the muscles providing the clockwise steering torque (group II). Group I consists of long head of triceps, Latissimus dorsi and posterior portion of deltoid, and group II consists of anterior and middle portions of deltoid, pectoralis major and Coracobrachialis. When the driver turns the steering wheel clockwise, the group I muscles of the right arm and the group II muscles of the left arm are activated, and in the counterclockwise rotation, the opposite muscles of each arm are involved. The shoulder muscles providing clockwise and counterclockwise steering torques are summarized in Table 4.2.

Table 4.2: List of shoulder muscles producing torque in the clockwise and counterclockwise direction when steering with two hands holding the steering wheel

Counterclockwise torque (group I)	Clockwise torque (group II)
Long head of triceps (TRIlong)	**Anterior deltoid (DELT1)**
Posterior deltoid (DELT3)	Middle deltoid (DELT2)
Latissimus dorsi (LAT)	Pectoralis major (PECT)
	Coracobrachialis (CORB)

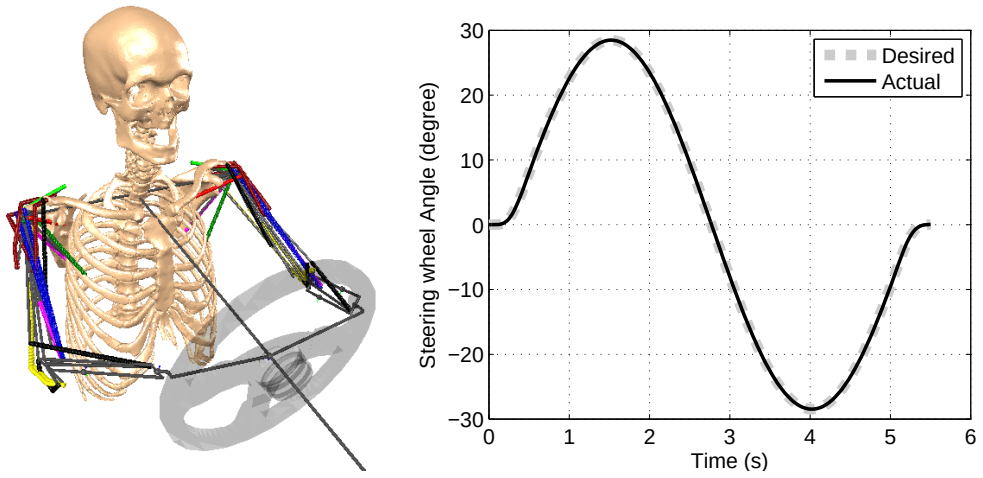

(a) (b)

Figure 4.22: (a) Schematic view of the driver model in MapleSim with two hands on the steering wheel, (b) The sinusoidal steering wheel angle maneuver

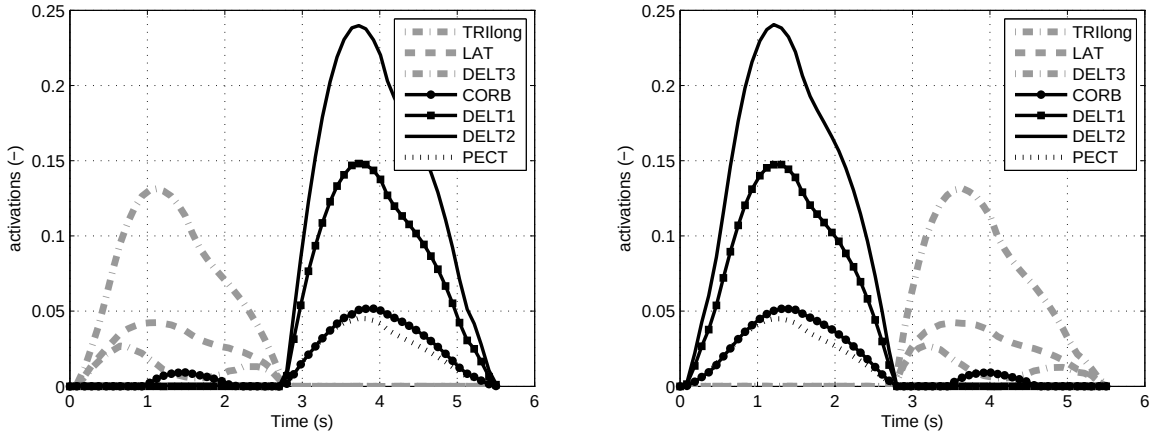

(a) (b)

Figure 4.23: Sinusoidal steering wheel task (a) Right arm shoulder muscle forces, (b) Left arm shoulder muscle forces

4.5 Simplified Two-dimensional Driver Model

In this section, a simplified two-dimensional (2D) neuromusculoskeletal driver model is developed to be used in component-level optimization procedures to design and develop new driver-assistance technologies. For the purposes of optimization, the model should be fast to reduce the optimization time and at the same time convey the important dynamics of the human driver.

To develop a simplified driver model, first, the kinematics of the high-fidelity 3D driver model performing a steering maneuver is studied. Figure 4.24 shows the variation of elbow and shoulder angles when the driver performs a sinusoidal steering maneuver with an amplitude of 45 degrees and frequency of 0.5 Hz (see Fig. 4.24a). As shown in Fig. 4.24b, the shoulder's plane of elevation and elevation angle are significantly larger than the elbow flexion and extension angle for a typical steering maneuver. The standard deviation of the elbow angle for this simulation is about 5 degrees while it is 22 and 18 degrees for the shoulder's plane of elevation and elevation angle. As expected, the standard deviation of the shoulder's axial rotation is small, around 3 degrees. The deviation of the elbow angle from its initial position is less than 5 degrees when the steering wheel angle variation is less than 35 degrees, and the humerus deviation from the humerus sagittal plane (see Fig. 4.25a) is less than 5 degrees for a steering variation of less than 14 degrees as shown in Fig. 4.25b. The humerus sagittal plane is defined as the plane normal to the initial humerus direction and the vertical axis of thorax.

As a result of the simulations performed for single and double hand steering in sections 4.4 and 4.3, it is known that the shoulder muscles are the prime movers in steering tasks, and the shoulder muscles of each arm can be classified into two groups: the muscles providing counterclockwise torque and the muscles providing clockwise torque on the steering wheel. This classification can be easily seen in Figs. 4.19 and 4.23 for the cases with one and two hands steering, respectively.

Therefore, removing the elbow joint and its associated muscles will have small effect on the dynamics of the driver's arm. Similarly, the shoulder joint can be reduced from a spherical joint to a revolute joint for small steering angles. Based on these assumptions, a

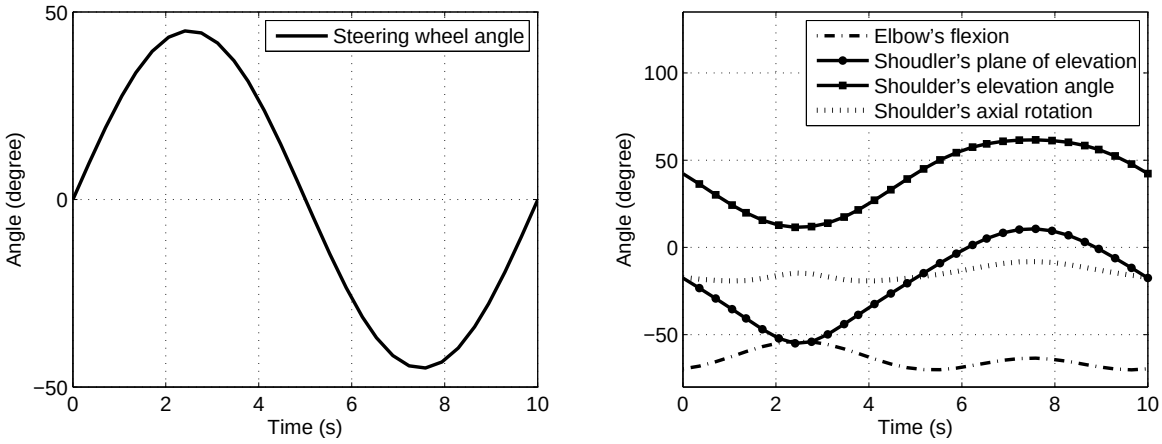

(a) (b)

Figure 4.24: (a) The sinusoidal steering wheel maneuver, (b) Shoulder and elbow angles presented by the recommendation of the International Society of Biomechanics (ISB). The shoulder angles are consistent with the description of shoulder joint angles recommended by the International Society of Biomechanics (ISB) [156].

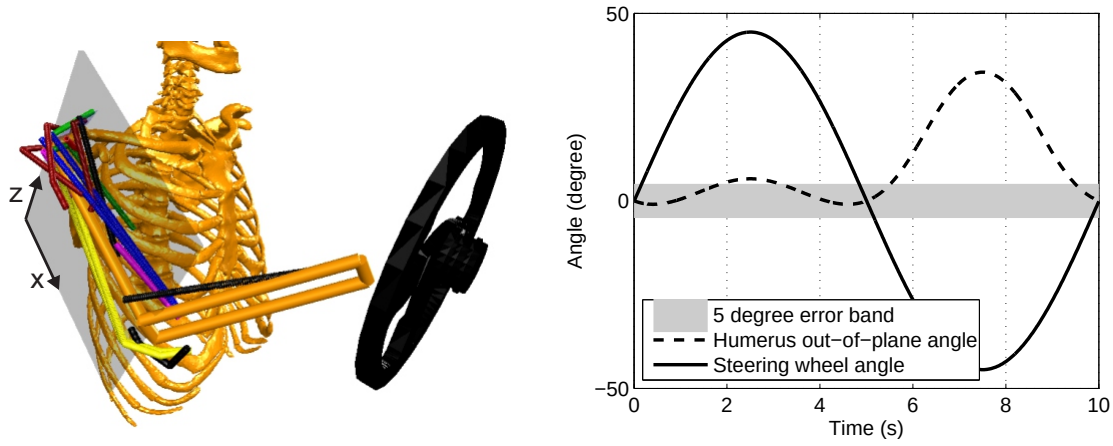

(a) (b)

Figure 4.25: (a) The sagittal plane of humerus in the initial position, (b) The deviation angle of humerus from the sagittal humerus plane during a sinusoidal steering maneuver

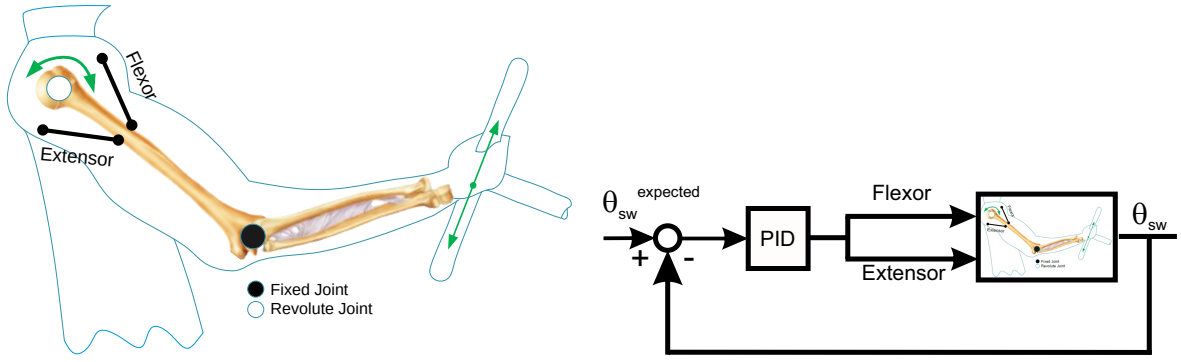

(a) (b)

Figure 4.26: (a) The two-dimension musculoskeletal driver model, (b) The simulation setup used to solve the muscle redundancy problem

simplified 2D driver model is developed as shown in Fig. 4.26a, in which the arm segments move only in the sagittal plane of the driver's body, pivoting at the shoulder. Two representative muscles, one flexor and one extensor, are used to actuate each arm segment. The two-element Hill-type muscle model (similar to the one used in the 3D driver model) is used to simulate muscle dynamics. Table 4.3 shows the parameters used in the 2D driver model.

Table 4.3: List of parameters used in the two-dimensional driver model

Parameters	Description	Value	Unit
F_0^{max}	maximum isometric muscle force	1200	[N]
r_{sw}	the radius of the steering wheel	0.21	[m]
ℓ	the distance between the hand gripping position at the steering wheel to the shoulder	0.7	[m]

A similar hierarchical CNS structure to the 3D driver model is used in the 2D driver model. In the first level, an identical path-following controller to the one used in 3D driver model is used to find the expected steering wheel angle. In the second level, zero co-contraction ratio is assumed for the physiological cost function (muscle fatigue, see Eq. (4.9)). This cost function leads to arm movements with no muscle co-contraction.

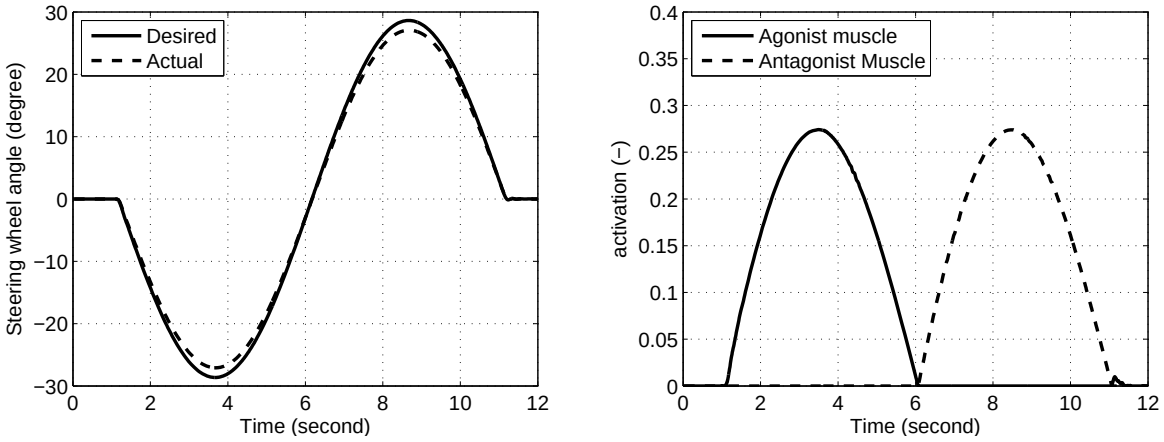

(a) (b)

Figure 4.27: (a) The desired and actual steering wheel angle of the 2D driver model, (b) The agonist and antagoinst muscle activation to perform the sinusoidal steering wheel angle

Since the arm model is reduced to the arm segment hinged at the shoulder actuated with a pair of agonist and antagonist muscle, a proportional-derivative (PD) controller is used instead of FSO to find the required shoulder torque to perform the steering task. Then, the required torque calculated by the PD controller is separated into positive and negative torques and fed to the agonist and antagonist muscles, as shown in Fig. 4.26b.

A sinusoidal steering maneuver is performed to study the performance of the 2D driver model. Figure 4.27a shows the desired and actual steering wheel angles, and the muscle activation to perform this maneuver for the right arm is shown in Fig. 4.27b; the muscle activations of the left arm are the opposite of those in the right arm, and there is no co-contraction between flexor and extensor muscles as expected.

The same stabilizer layer structure as the 3D driver model is used in the simplified 2D driver model by constructing the the stretch reflex feedback loop for the agonist and antagonist (flexor and extensor) muscles. This model has the same disturbance rejection properties as the high-fidelity model. A similar scenario as described in section 4.2.2.2 is used in the relaxed driving condition (no co-contraction and no disturbance observer)

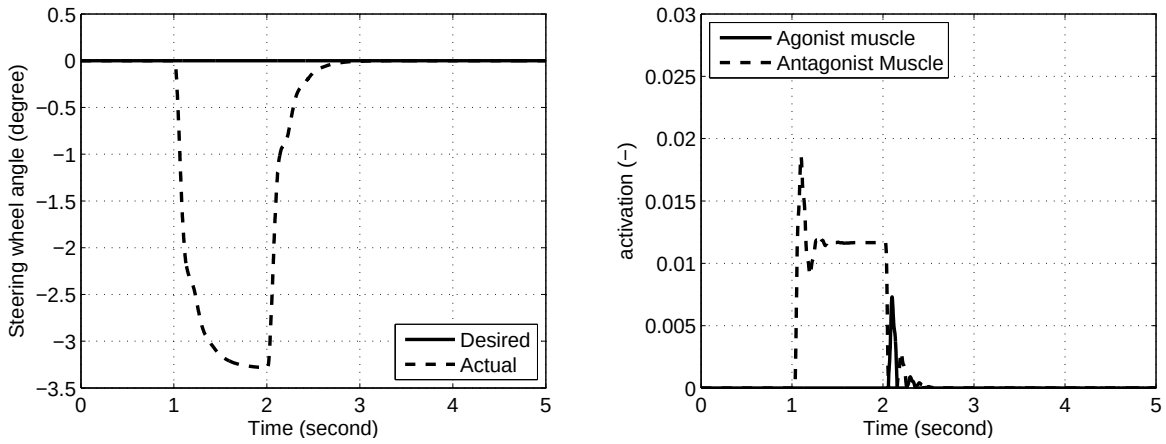

(a) (b)

Figure 4.28: (a) The desired and actual steering wheel angle of the 2D driver model, (b) The agonist and antagoinst muscle activation to perform the sinusoidal steering wheel angle

to study the disturbance rejection properties of the 2D driver model. Figure 4.28a shows the steering angle variation when a disturbance torque (see Fig. 4.33b) is applied to the steering wheel, and figure 4.28b shows the muscle activations associated with the stretch reflex.

4.6 Validation of Passive Properties of Musculoskeletal Driver Models

Pick and Cole [117] in 2007 performed an experiment to identify the passive properties of driver arms holding a steering wheel. In this experiment, the steering wheel was subjected to a filtered pseudo-random binary-sequence excitation, and drivers asked to hold the steering wheel. Eight young subjects consisting of seven males and one female (21-32 year-old) with average height of 1.7 m and weight of 75 kg are used to collect electromyography data as well as the steering torque and steering wheel angle. In this experiment, the

intrinsic stiffness of the arm (joints and muscles) and the reflexive response of arm (stretch reflex) contribute to the steering response. The authors suggest that a single-degree-of-freedom linear mass-damper-spring model can be used to capture the underlying dynamics of the passive response of the driver arm:

$$H_{mod}(S) = \frac{\theta(S)}{T(S)} = \frac{1}{J_{dr}S^2 + B_{dr}S + K_{dr}} \tag{4.13}$$

where K_{dr} and B_{dr} are the torsional stiffness and damping of the driver's arm as seen at the steering wheel, and J_{dr} is the inertia of arm and steering wheel. Three conditions have been studied to identify the transfer function parameters: fully relaxed muscles, co-contracted muscles, and biased muscles. In the fully relaxed condition, the subjects were asked to hold the steering wheel with just enough force that the hands are not slipping as wheel rotates, while in the co-contracted muscle condition, the subjects were co-contracting the muscles in order to hold the steering wheel firmly in the straight ahead position. In the biased condition, the subjects were asked to hold the steering wheel at a constant angle by tensioning the muscles enough to hold steering wheel stationary, but otherwise relaxed the muscles as possible. The identified parameters for the first and second condition are given in Table 4.4 and are used to evaluate both the 3D and 2D driver models.

Table 4.4: The identified parameters of the passive properties of driver arm [117]

Condition	J_{dr} (kg.m^2)	B_{dr} (N.m.s/rad)	K_{dr} (N.m/rad)
fully relaxed	0.130	0.35	4.17
co-contracted	0.130	1.08	78.63

As shown in Table 4.4, the damping coefficient is slightly increased and the stiffness coefficient is significantly increased in the co-contracted condition compared to fully relaxed condition. The increased stiffness is associated with the joint stiffness induced by co-contracting all the muscles wrapping the shoulder and elbow joints. Co-contracting an agonist and antagonist muscle pair around a joint change the length of muscle tendons, which result in more stiffness at the joint while producing the same actuating torque.

A similar study to Pick and Cole [117] is performed on the 3D and 2D driver models to

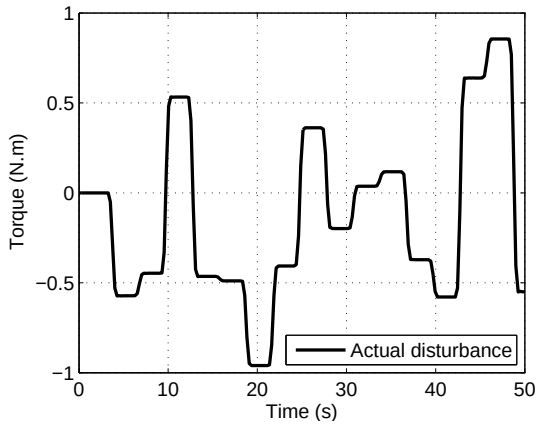

Figure 4.29: The random signal used as the disturbance torque at the steering wheel to evaluate the passive properties of driver arm

verify and adjust the parameters associated with the passive properties of driver model, i.e. stretch reflex and stiffness of joints, which are reported in Table 4.5. Figure 4.29 shows the excitation at the steering wheel in the fully relaxed and co-contracted conditions. In the fully relaxed condition, the co-contraction ratio is zero while in the co-contracted condition it is equal to 40%. Since the objective of these experiments is to identify the muscle passive parameters, the cognition time delay associated with the disturbance observer is assumed to be longer than the disturbance period. This means the model only uses the passive properties of arm to counteract the unknown disturbance torque.

As shown in Figs. 4.30 and 4.31, the driver-steering system responses of the 2D and 3D driver models correlate with Pick and Cole's identified transfer functions for the fully relaxed muscles and co-contracted muscle conditions, respectively. Figures 4.30b and 4.31b show the passive torques produced at the shoulder and elbow joints of the driver arm.

Table 4.5: List of the joint stiffness and the reflexive parameters used in the 2D and 3D driver models

Parameters	Description	Value	Unit
K_{sh}, C_{sh}	stiffness and damping of shoulder joint of 3D model	12, 8	[N/m, N.s/m]
K_e, C_e	stiffness and damping of elbow joint of 3D model	50, 10	[N/m, N.s/m]
K_{sh}, C_{sh}	stiffness and damping of shoulder joint of 2D model	100, 5	[N/m, N.s/m]
K_p^{sr}, K_d^{sr}	proportional and derivative stretch reflex coefficient of 2D and 3D model	9, 1	[N/mm, N.s/mm]

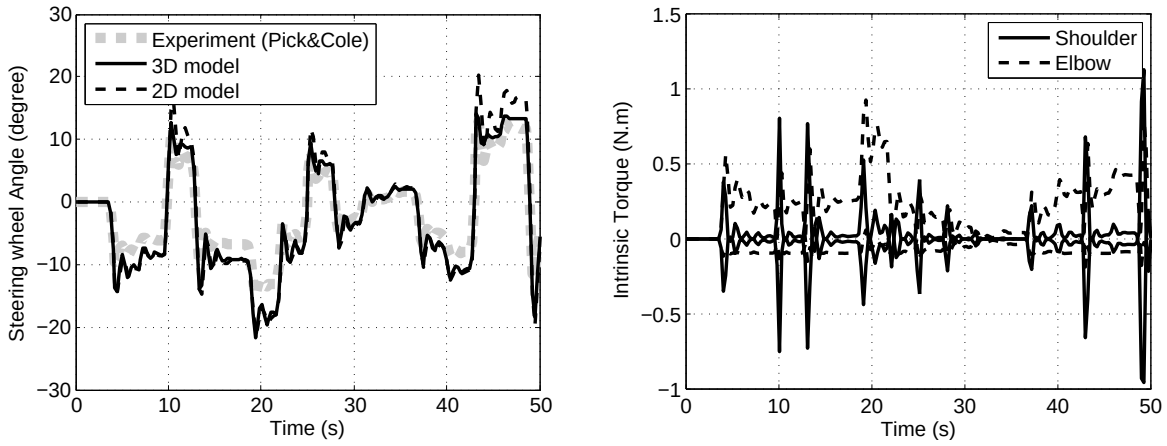

(a) (b)

Figure 4.30: The driver response to the random steering torque when the driver is holding the steering wheel in the fully relaxed condition (a) The steering wheel angle, (b) The shoulder and elbow joint passive force

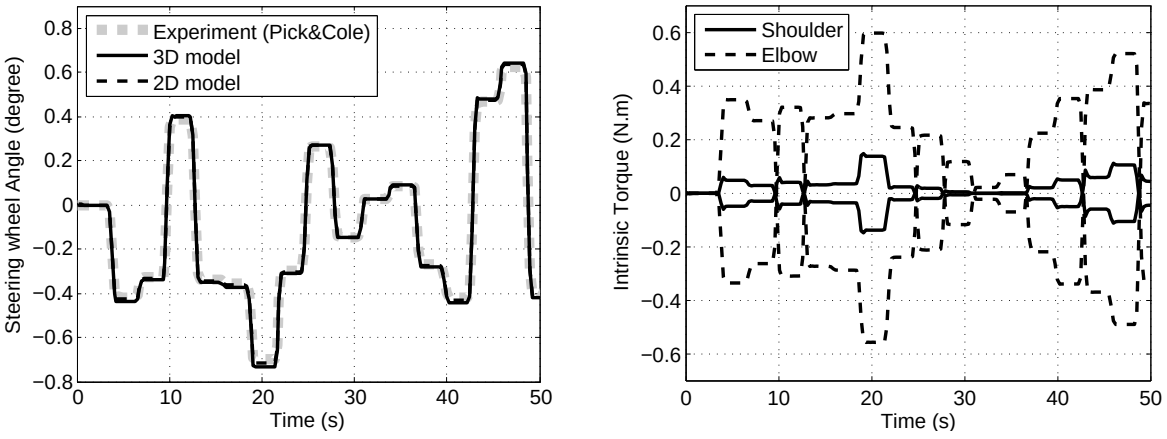

(a) (b)

Figure 4.31: The driver response to the random steering torque when the driver is holding the steering wheel in the co-contracted condition (a) The steering wheel angle, (b) The shoulder and elbow joint passive force

4.7 Simulation Results and Discussion

Two simulation studies have been performed to study the performance of the driver models in different steering maneuvers. In the first simulation, the two-dimensional driver model performs a double lane change maneuver without any external disturbance in the relaxed driving condition. In the second maneuver, the three-dimensional driver model performs a lane change maneuver in the presence of an external disturbance in the relaxed and tensed driving conditions. All the simulations are performed in the Matlab/Simulink environment. The MapleSim models are exported as optimized C-code using the Maple CodeGeneration toolbox to Matlab, and the motor control framework is constructed in the Simulink environment.

4.7.1 ISO Double Lane Change Maneuver with Two-dimensional Driver Model

The simulation results of the first simulation study are presented in Fig. 4.32. In this simulation, the two-dimensional driver model performs an ISO double lane change (DLC) maneuver with the speed of 10 m/s.

A trajectory satisfying the ISO lane change constraints is predefined and used as the desired trajectory of the vehicle position in the path planning controller, as shown in Fig. 4.32a. Figure 4.32b shows the expected steering wheel angle calculated by the path planning controller to follow the predefined trajectory. The actual value closely follows the expected value; it means that the PD controller can successfully replace the forward static optimization (FSO) controller. Figure 4.32c shows the required agonist and antagonist muscle activations calculated by the PD controller to perform the steering maneuver. Since there is no disturbance to the system and the maximum activation is less than the maximum allowable activation (a_{max}=1), the actual steering wheel angle is equal to its expected value.

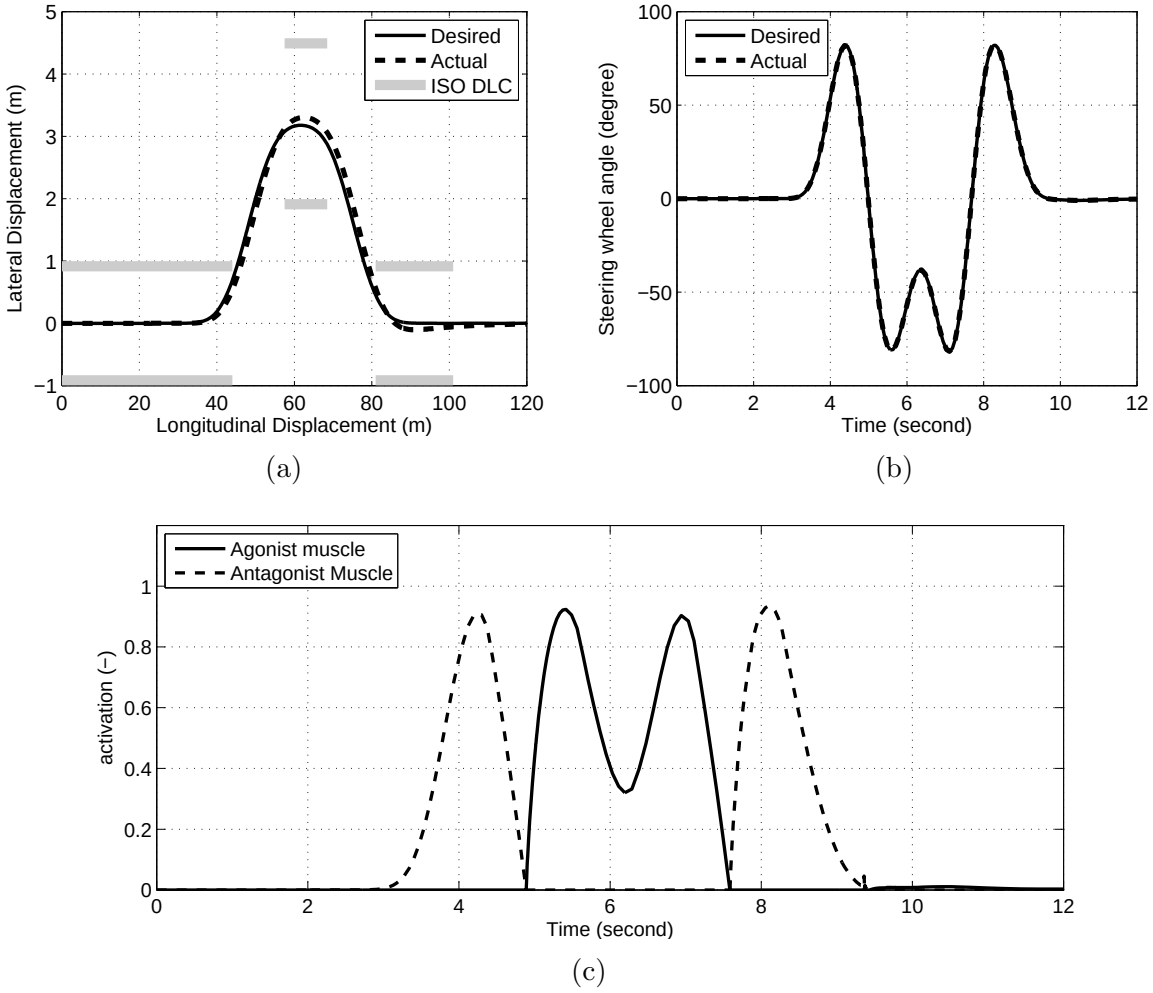

Figure 4.32: Simulation results of the double lane changing maneuver using two-dimensional driver model (a) Desired and actual lateral displacement with ISO lane change trajectory constraints, (b) Desired and actual steering wheel angles (c) Muscle activations to perform the ISO lane change maneuver

4.7.2 Lane Change Maneuver with Three-dimensional Driver Model

The simulation results of the second simulation study, a step-like lane change maneuver, at the speed of 10 m/s using the 3D driver model are presented in Figs. 4.33 and 4.34. Three simulations have been performed to show the full extent of the physics-based driver model capabilities. The first simulation is performed in the normal driving condition (no disturbance). The other two simulations correspond to relaxed and tensed driving conditions, when a two second long pulse-shaped disturbance occurs at the steering wheel. The torque disturbance at the steering wheel could be considered the result of a pothole or a strong cross wind. The parameters used in the simulations are summarized in Table 4.6.

In the relaxed condition, the voluntary contribution of the CNS (the FD controller) in disturbance rejection is neglected; in other words, it takes longer for the observer to estimate the altered states than the duration of disturbance itself. Additionally, the muscle co-contraction ratio is assumed to be zero; therefore, there is no intrinsic muscle stiffness properties in the relaxed driving condition. In the tensed driving condition, the latency associated with the disturbance observer and the muscle co-contraction ratio are assumed to be 300 ms and 30%, respectively.

Figures 4.33 and 4.34 show the effect of the external disturbance on all layers of the motor control framework. Figure 4.33a shows the comparison between the lateral displacement of the vehicle in the presence and absence of the disturbance. It can be seen that, for all three conditions, the driver starts to steer 2.5 seconds before the desired trajectory, which is consistent with predictive ability of the path following controller; the responses also settle down at about t=9 s. However, the deviation from the desired path (overshoot)

Table 4.6: Co-contraction ratio and stretch reflex and disturbance observer time delay values used in the simulations

Parameters	Description	Value	Unit
α	muscle co-contraction ratio (relaxed, tensed)	(0%, 30%)	[-]
τ_d^e	disturbance observer time delay (relaxed, tensed)	(∞, 0.3)	[s]
τ_d^{sr}	stretch reflex time delay	0.025	[s]

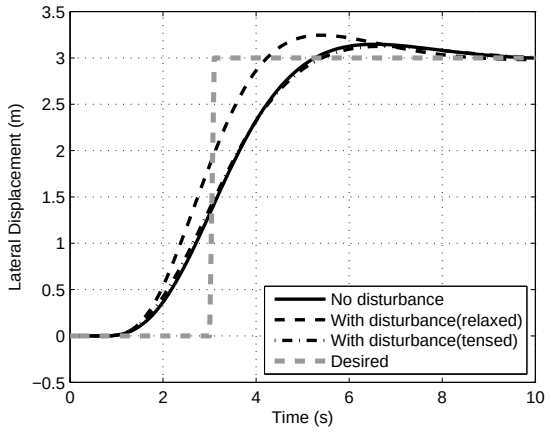

(a)

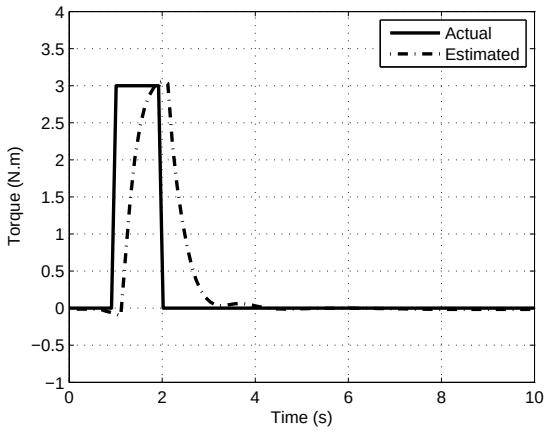

(b)

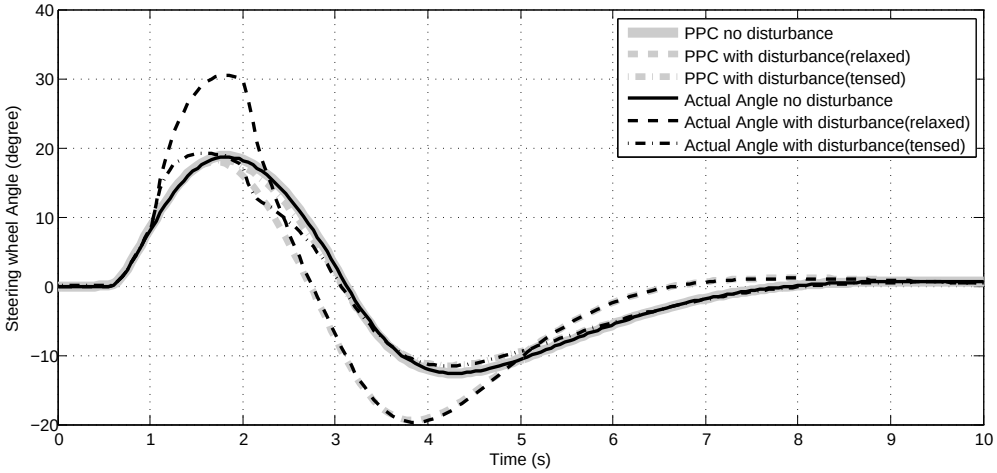

(c)

Figure 4.33: Simulation results of the lane changing maneuver (a) Desired and actual lateral displacement with and without disturbance, (b) Actual and estimated disturbance torque applied to the steering wheel (c) Desired and actual steering wheel angles, with and without disturbance. PPC is the output of path planning controller.

of the perturbed vehicle is different across the three simulations. In the relaxed driving condition, the overshoot is more than the tensed condition and unperturbed vehicle. This difference is a result of the difference in the actual steering wheel angles in Figure 4.33c.

As a result of the disturbance, the reflex addition to the muscle forces is substantial. However, despite the stretch reflex corrections, the arm cannot follow the desired steering wheel trajectory. This deviation in the steering wheel angle, in turn, results in a deviation in the vehicle's path. The path following controller then tries to correct the path by providing a new desired steering wheel angle, which finally results in different muscle activations that are predicted by the force distribution controller compared to the case with no external disturbance.

In addition to the disturbance itself, Figure 4.33b also shows the performance of the disturbance observer for the tensed driving condition. It can be seen that the observer does not start to identify the disturbance at the steering wheel until 300 ms (the observer time delay) after its onset, after which it quickly reaches the actual disturbance torque. The time delay associated with the observer is the latency regarding the information transmission to and processing in the sensorimotor area of brain, which leads to voluntary response of the driver to overcome the disturbances. The slight difference between the estimated and actual disturbance in the no disturbance zone is due to the difference between the internal model and the actual vehicle model.

At the beginning and end of the disturbance we have the largest error in the disturbance estimation, which causes the largest error in the actual and desired steering wheel angles. These periods are the times before the voluntary action intervenes and reduces the disturbance. At the same time, because of this error in the steering wheel angle, the first layer of the motor control framework, the path-following controller, intervenes and corrects the desired steering wheel angle to follow the new desired path.

Figure 4.34 shows the required muscle activations wrapping the shoulder to perform the expected steering wheel angle in the three simulation conditions. It can be seen that there is no antagonist muscle activation in the no disturbance condition as shown in Fig. 4.34a, as the gravity helps the driver to turn the steering wheel clockwise. In this condition, the anterior and the middle part of deltoid muscle (DELT1, DELT2), coracobrachialis muscle (CORB), infraspinatus (INFRA) and pectoralis major (PECT) are responsible for the steering action. On the other hand, in the relaxed condition, as a result of the disturbance and consequently the deviation of steering angle from its expected value, the antagonist

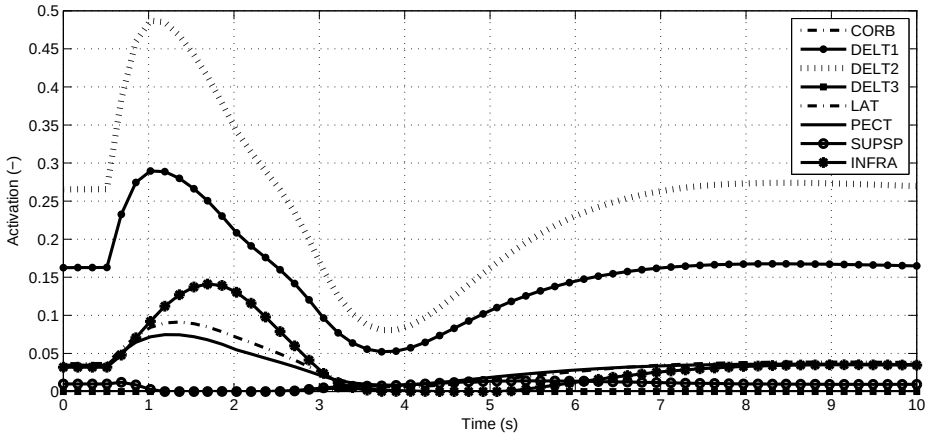

(a)

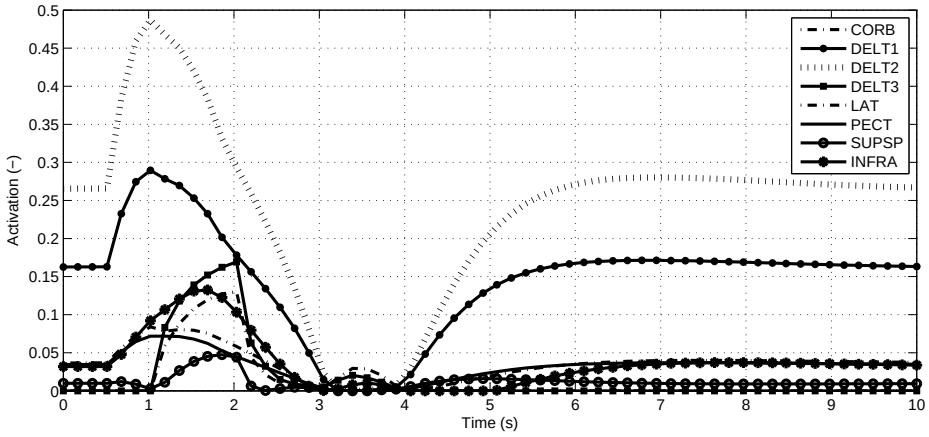

(b)

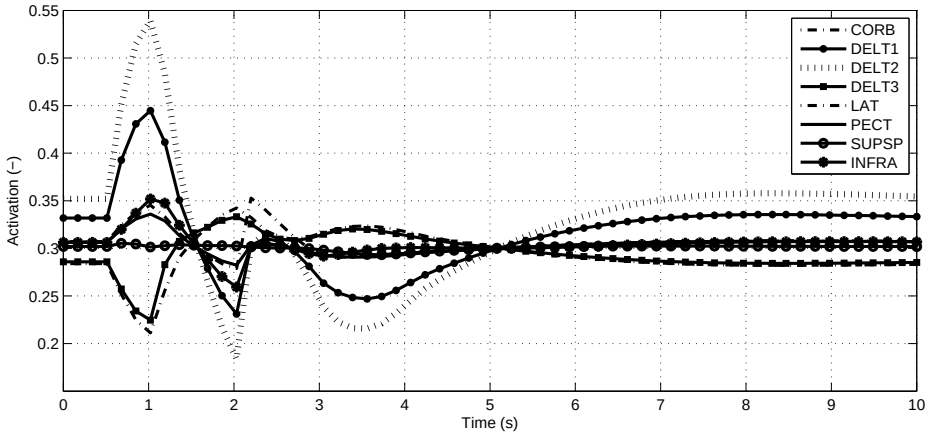

(c)

Figure 4.34: (a) Total shoulder muscle activations during the maneuver without disturbance (only active muscles are shown), (b) Total muscle activations during the maneuver with the presence of disturbance in the relaxed driving condition, (c) Total muscle activations during the maneuver with the presence of disturbance in the tensed driving condition. Note the difference in vertical scale.

muscles are activated to first stabilize the steering wheel and then to return it to its expected value. In the tensed driving condition, the muscle activations are already built up to stabilize the steering if there is a disturbance. As shown in Fig. 4.34c, both agonist and antagonist muscles are activated to reject the disturbance; thus the vehicle closely follows the path of the unperturbed vehicle.

4.8 Chapter Summary

In this chapter, a high-fidelity driver model (3D driver model) as well as a control-oriented driver model (2D driver model), in conjunction with a hierarchical central nervous system model, are developed. Both models are evaluated against published experimental data, to verify the passive and active properties of a human driver model.

A hierarchical approach is used to capture the complexity of neuromuscular dynamics and the CNS in the coordination of driver upper limb activity, and consequently the steering wheel angle. The proposed motor control framework has three layers: the first layer is responsible for finding the proper steering wheel angle to follow the desired path, the second layer is responsible for actuating the arm, and the final layer is added to ensure better control precision and disturbance rejection. In the final layer, the CNS regulates the muscle activation by modulating the intrinsic stiffness of the muscle and stretch reflex phenomena to coordinate the movement of limb in the presence of external disturbances or steering faults.

"The real voyage of discovery consists not in seeking new landscapes, but in having new eyes."

Marcel Proust (1871 – 1922)

5

Electric Power Steering Control Design

Recent research studies suggest that considering the human driver alongside the vehicle measurements can lead to better understanding of the underlying dynamics between driver and vehicle as well as more accurate evaluation of driver-assist technologies [50, 98]. As an example, a neuromuscular driver model offering physiologically realistic steering maneuvers can provide insights into the task performance and energy consumption of the driver. Considering specific driver or a general population characteristic in the design can enhance and strengthen a driver-assist product. In this thesis, a two-dimensional (2D) driver model as described in section 4.5 is used to study the effect of the driver's characteristics such as age, gender and physical ability on the steering tasks. Then, this modified driver model is used to tune the Electric Power Steering (EPS) characteristic curves for that particular population.

Many research studies have investigated the structural design of the EPS controller but left the characteristic (assist) curve design unattended. The design of characteristic curves is a complex procedure and usually is based on trial and error. The shape and dynamics of these curves were studied in [168, 167, 74, 157] to provide easier implementation and better assistance; however, there is no well-accepted curve in the literature yet. A well-defined characteristic curve should be designed to allow a permissible level of resistance (road feel), while providing enough assistance to reduce driver fatigue.

In this chapter, a systematic approach has been proposed to tune the characteristic curves for both road feel and assistance. Then, a model-based EPS controller is developed to incorporate these characteristic curves as well as to attenuate external disturbances to the system.

5.1 Effects of Age and Gender on Muscle Mechanics

The 2D neuromuscular driver model is human-centered, meaning that the physical abilities and limitations of the driver are taken into account. Many studies have documented changes in the mechanical output of skeletal muscles with aging. These changes can be the result of age-related muscle atrophy and re-modeling. These phenomena can occur as early as the age of 30 in men, and can reach a loss of 54-89% in the muscle strength by the age of 75 [139]. However, this decrease is only observed in the 5^{th} decade in women [133].

The muscle atrophy due to a decrease in the total number, size and the specific strength of muscle fibers is reported to reduce the maximum muscle isometric force (muscle strength) by 20 to 40 percent by the age of 70 [139]. In this thesis, the average value of 30 percent reduction is chosen for older adults. Older muscles also have larger amounts of non-contractile tissues, which result in a greater portion of total tension. This is reflected in the model by reduction of the passive muscle strain in older adults.

The number of fast twitch motor units and their cross-sectional area are reported to be reduced by 20 percent in old muscles, which can result in a reduction in the muscle maximum contraction velocity [139]. Since the muscle strength during lengthening is better

Table 5.1: List of muscle parameters for young and old adults

#	population	$V_m^{max}(L_0^{opt}/s)$	ϵ_0	$\bar{F}_{len}^{max}$	$F_0^{max}(\%)$
1	Young Male	10	0.6	1.4	100
2	Old Male	8	0.5	1.8	70
3	Young Female	10	0.6	1.4	80
4	Old Female	8	0.5	1.8	50

preserved with age, the maximum normalized force achievable during lengthening ($\bar{F}_{len}^{M}$) was increased from 1.4 for young adults to 1.8 for older adults [139]. Other parameters such as the optimal fiber length and shape, as well as the tendon stiffness are relatively unchanged by age, and therefore assumed to be constant in this study. Table 5.1 shows the adjusted muscle parameters for young and old adults.

Figure 5.1a demonstrates the effect of changes in the maximum contraction velocity (V_m^{max}) of muscle on the generated normalized muscle force. The normalized muscle force is more sensitive to a variation of V_m^{max} in the negative contraction velocities (shortening) than the positive contraction velocities (lengthening). Similarly, Fig. 5.1b shows that with a stiffer passive muscle strain (ϵ_0^m), the produced muscle force increases in the long muscle lengths. As expected the maximum normalized force during lengthening is strongly a function of $\bar{F}_{len}^{max}$, as shown in Fig. 5.2a. Figure. 5.2b shows the effect of the combination of V_m^{max} and $\bar{F}_{len}^{M}$ on the normalized muscle force.

Studies on the knee and trunk muscles show, in general, the peak value of generated torque in women in all age groups, regions and function is lower than men [133]; specifically, the knee extension muscles in men can produce 20% more torque than women. Similarly, another study compared the abduction, adduction, internal and external rotation strength of the arm for healthy men and women [54]. The authors proposed that the strength reduced linearly by age, and women can produce less torque than men. In this thesis, the maximum isometric muscle force is reduced by 20% in women; however, the other parameters are kept unchanged.

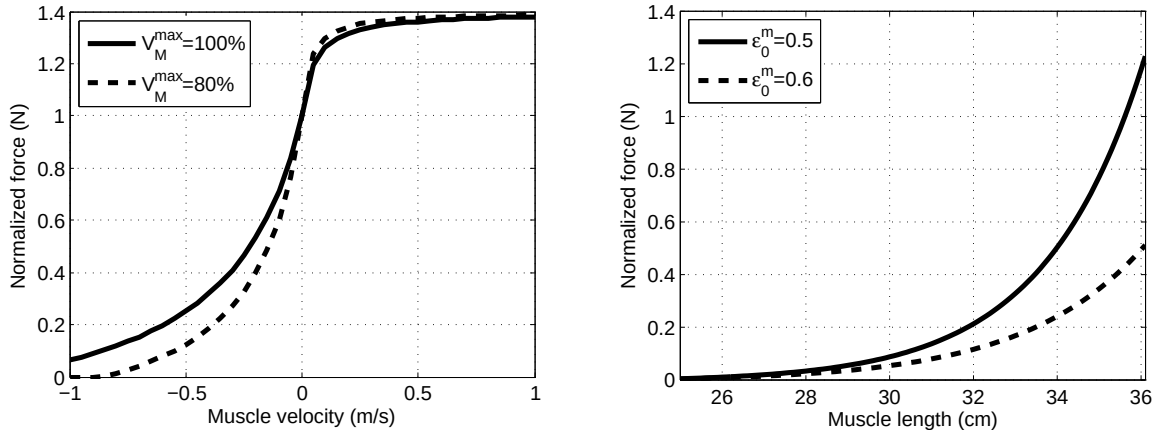

(a) (b)

Figure 5.1: (a) The effect of variation of maximum muscle contraction velocity on the normalized muscle force, (b) The effect of variation of muscle passive strain on the normalized muscle force

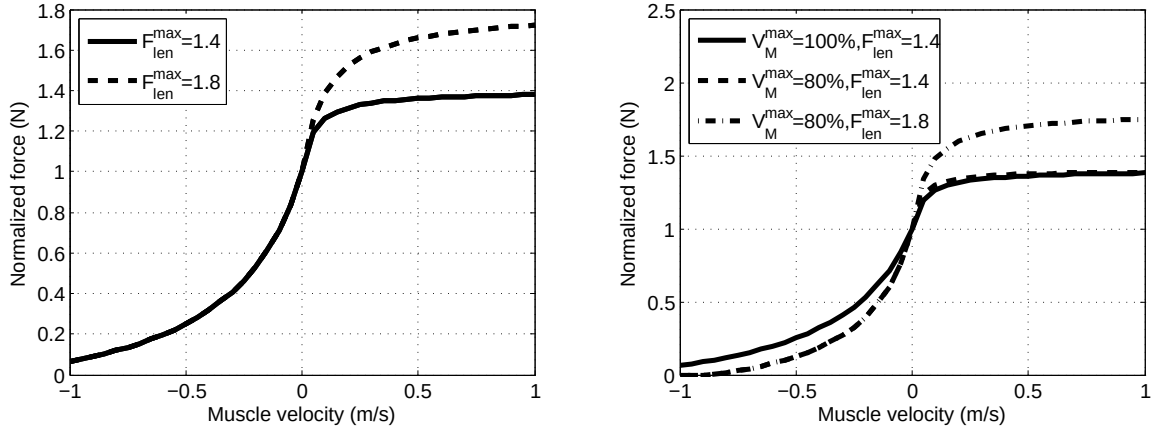

(a) (b)

Figure 5.2: (a) The effect of variation of maximum muscle force during lengthening on the normalized muscle force, (b) The effect of variation of combination of maximum muscle contraction velocity and maximum force during lengthening on the normalized muscle force

5.2 EPS Characteristic Curves

In design optimization, a low-order linear model is more desirable than a high-order non-linear model because it reduces the computational time while conveying the important dynamics of the high-fidelity model. Therefore, in this study, a linear vehicle model including a column-assist EPS system (control-oriented model, as described in section 3.2) in conjunction with a 2D driver model (as described in section 4.5) is used to study and design an EPS characteristics curve. Figure 5.3a shows a schematic diagram of the steering system of the control-oriented model and the location of the electric power steering system. Since the EPS controller will be designed to track a desired assist torque based on the EPS characteristic curves, the dynamics of electric motor and reduction gear are neglected here and it is assumed that the assist torque is directly applied at the steering column. Typically, the steering characteristic curves are a non-linear or multi-linear function of the driver steering torque at different vehicle speeds. In this section, a nonlinear and a bi-linear characteristic curve are introduced and tuned for the different driver types in Table 5.1.

5.2.1 Nonlinear EPS Characteristic Curve

Figure 5.3b shows a steering characteristic curve (at a specific vehicle speed), which is a non-linear function of the driver torque. This characteristic curve or so-called nonlinear EPS characteristic curve consists of an unassisted zone to avoid the off-center feeling, a sinusoid steering assistance zone and a saturation zone. This curve is expressed by the following equation [157]:

$$T_a = \begin{cases} 0 & 0 < T_d < T_{d0} \\ f(T_d) & T_{d0} < T_d < T_d^{max} \\ T_m^{max} & T_d^{max} < T_d \end{cases} \tag{5.1}$$

where

$$f(T_d) = \frac{1}{2}\left\{\sin\left[\pi\left(\frac{T_d - T_{d0}}{T_d^{max} - T_{d0}}\right)^{\kappa} - \frac{\pi}{2}\right] + 1\right\} T_m^{max} \tag{5.2}$$

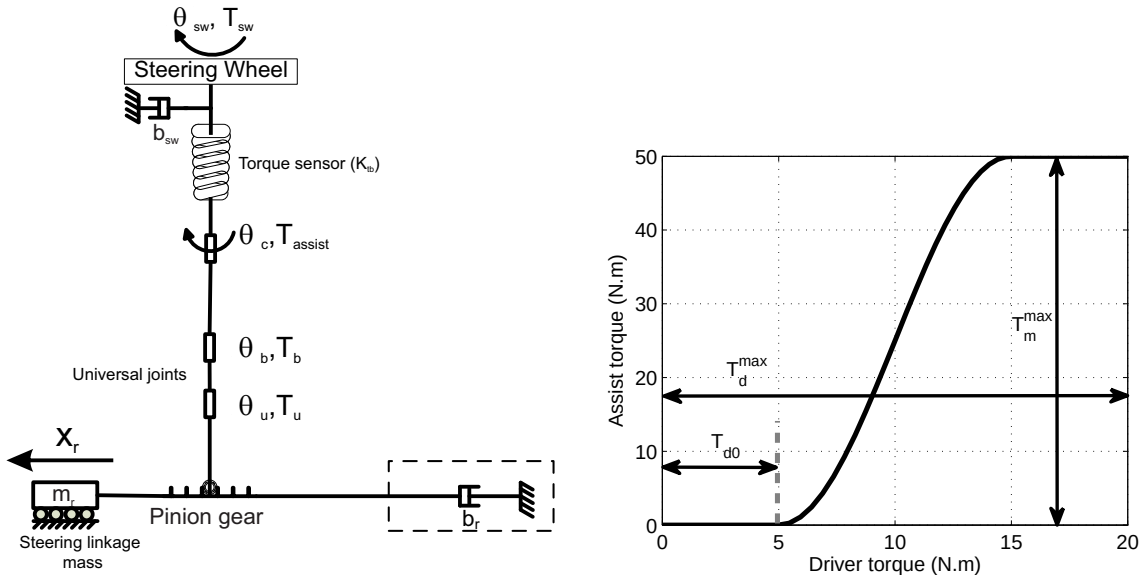

(a) (b)

Figure 5.3: (a) A schematic view of column-assist EPS system, (b) Sinusoidal EPS characteristic curve

and T_a and T_m^{max} represent the assist torque and the maximum torque of the motor. T_d, T_{d0} and T_d^{max} respectively represent the driver's steering torque, the driver's steering torque when the motor begins to assist, and the driver's steering torque when the motor assist reaches the maximum assistance. The exponent κ is a shape factor associated with the slope of the characteristic curve. Figure 5.4 illustrates the effect of variation of the shape factor (κ) and the maximum driver torque (T_d^{max}) on the shape of the EPS characteristic curve. In Fig. 5.4a the maximum driver torque is kept constant while the shape factor is increased gradually; it can be seen that the increase of shape factor reduces the assistance since the maximum assist torque is fixed. Similarly, in Fig. 5.4b the driver maximum torque is varying when the shape factor is fixed; it can be seen that an increase in the maximum driver torque results in the reduction of assistance.

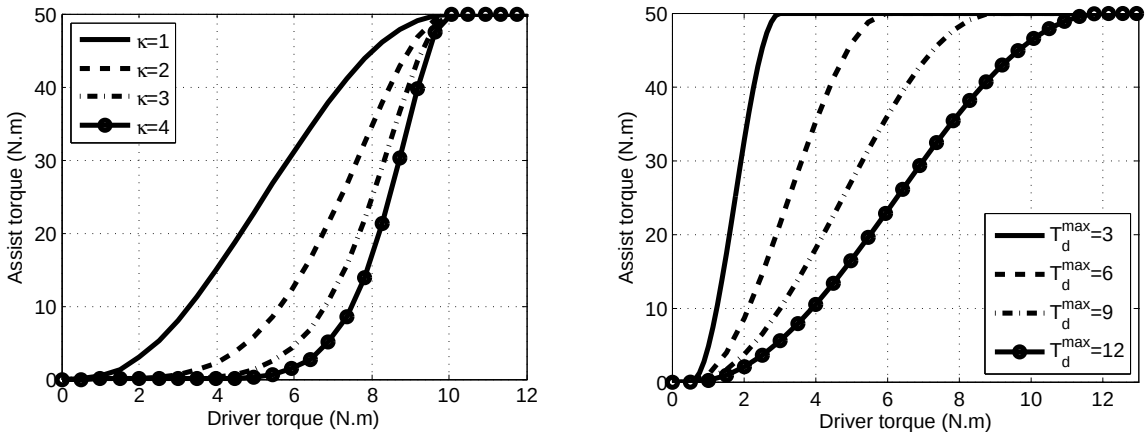

(a) (b)

Figure 5.4: Sinusoidal EPS characteristic curve (a) Effect of variation of κ, (b) Effect of variation of T_d^{max}

5.2.2 Bi-linear EPS Characteristic Curve

Figure 5.5a shows a steering characteristic curve which is a bi-linear function of the driver torque at a constant vehicle speed. Similar to the nonlinear EPS characteristic curve, the bi-linear characteristic curve consists of an unassisted zone, a steering assistance zone, and a maximum assist value that is restricted by maximum motor torque. The bi-linear characteristic curves can be expressed as follow:

$$T_a = \begin{cases} 0 & 0 < T_d < T_{d0} \\ K_a(T_d - T_{d0}) & T_{d0} < T_d < T_m^{max}/K_a + T_{d0} \\ T_m^{max} & T_m^{max}/K_a + T_{d0} < T_d \end{cases} \tag{5.3}$$

where K_a is the assist gain, and the remaining of parameter definitions are similar to the nonlinear characteristic curve. The nonlinear (sinusoidal) EPS characteristic curve has two adjustable shaping factors (T_d^{max}, κ), whereas the bi-linear curve has only one shaping factor (K_a). Therefore, the calibration procedure for the bi-linear curves is easier than the nonlinear curve.

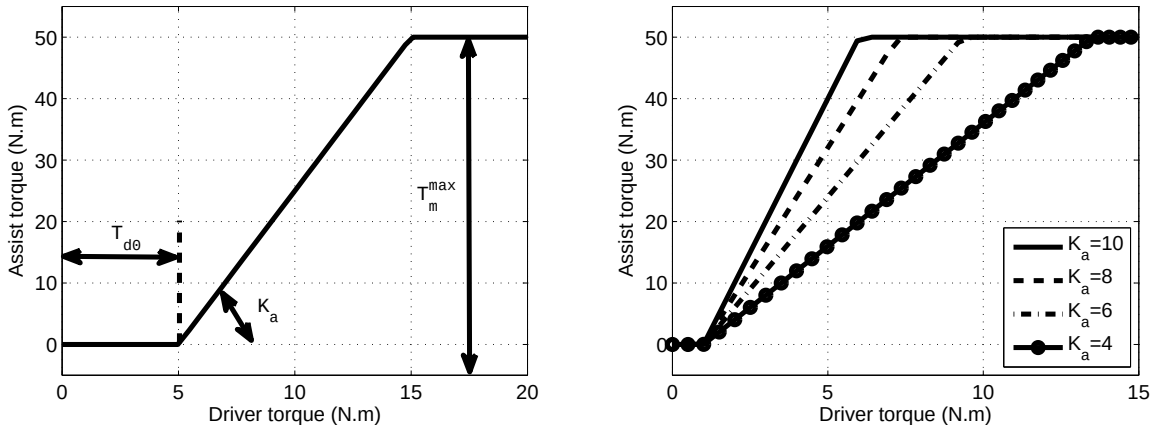

(a) (b)

Figure 5.5: (a) Bi-linear EPS characteristic curve, (b) Effect of variation of K_a on the characteristic curve

5.3 Steering Feel Optimization Procedure

In this section, a systematic approach to tune the EPS characteristic curves to provide a good steering feel is introduced. However, the word "good" is very subjective and is a function of many parameters such as the driver's physical ability. Therefore, to achieve a good steering feel, both driver characteristics and the road feel should be considered in the EPS characteristic curve. In this case, the average energy transferred from road to driver (road feel) should be as strong as possible in a certain frequency domain, while the physical workload of the driver should be minimized.

The transferred torque to the steering wheel can be separated into two portions: (1) the torque due to road-tire friction and suspension mechanism and (2) the torque due to external disturbances. Since the disturbance forces applied to the steering system will be attenuated by the EPS controller (see section 5.5), this portion is neglected here. In this study, the control-oriented vehicle model steered with the 2D driver model is used to simulate an ISO double lane-change maneuver [40] at a speed of 10 m/s. The expected trajectory of the vehicle is defined in such a way that the ISO double lane change maneuver

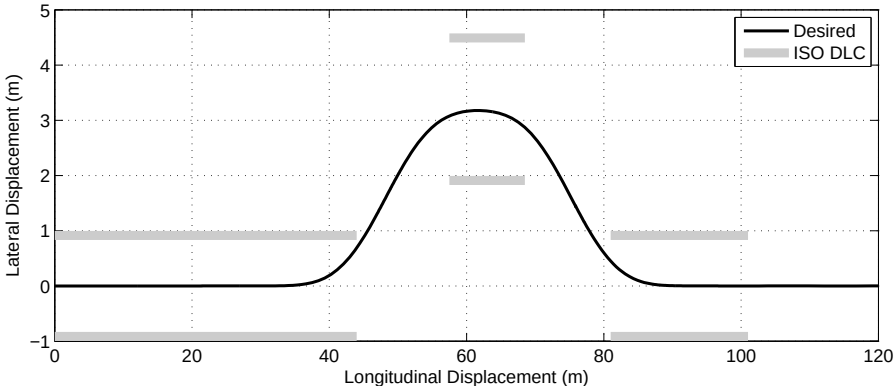

Figure 5.6: ISO double lane change (DLC) constraint and vehicle desired trajectory.

constraints are satisfied as shown in Fig. 5.6.

To tune the EPS characteristic curves for a particular population, the muscle parameters are adjusted to represent the population. Then, an optimization is performed to find the optimum EPS assist curves for that specific population. The characteristic curve parameters (κ and T_d^{max}) for the sinusoid and (K_a) for the bi-linear curve have been optimized for different driver types by minimizing the following cost function:

$$CF = \frac{1}{t_f} \int_0^{t_f} \Big(q_1 \ \tilde{F}_{rf} + q_2 \ G(a) + q_3 \ i^2 \Big) dt \tag{5.4}$$

where $\tilde{F}_{rf}$ and $G(a)$ respectively are the inverse of road feel and the muscle fatigue of the driver during the steering task, and i is the electric motor current. q_1, q_2 and q_3 are the weighting factors, which have been chosen in a way to normalize each term in the cost. The q_1 and q_2 weighting factors are used to adjust the steering stiffness while q_3 is used to reduce the EPS electric motor size. The muscle fatigue ($G(a)$) is defined in Eq. (4.8), and it is assumed that the driver is in the relaxed condition (there is no muscle co-contraction while performing the maneuver, $\alpha_i = 0$).

The road feel criterion is used to quantify the intensity of feedback information from the road to the driver. To consider the non-linearity induced by the steering system and the assist curve for a specific maneuver, the road feel is defined in the time domain as the

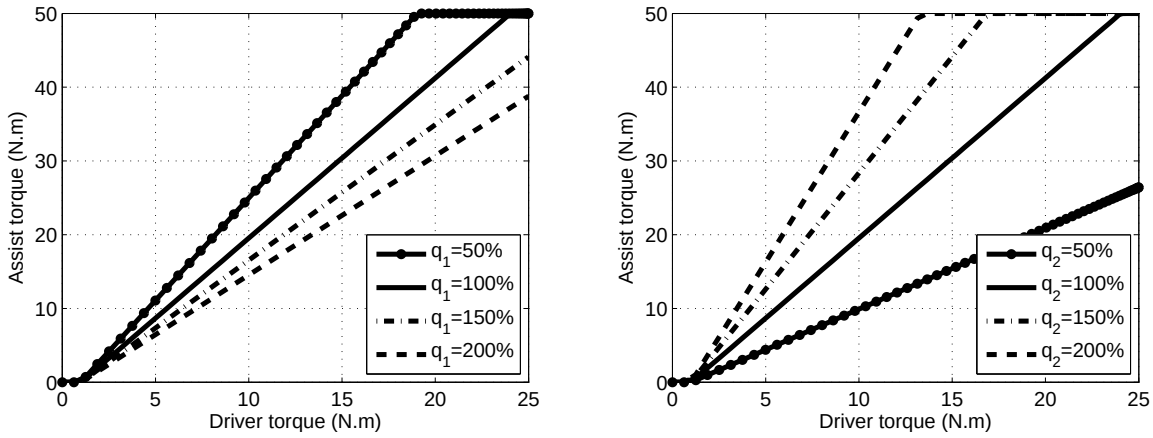

(a) (b)

Figure 5.7: Sensitivity of the optimal characteristic curve to the variation of optimization weights, (a) Variation of q_1, (b) Variation of q_2

relationship between the resistive steering torque to the driver torque as follows [163]:

$$F_{rf} = \frac{1}{\tilde{F}_{rf}} = \frac{|T_d(t)|}{|T_r(t)|} \tag{5.5}$$

where T_r is the resistive torque at the pinion gear, and T_d is the driver torque. Since the resistive torque is due to road-tire friction force, the larger the ratio is, the more feedback (feel) is delivered to driver about the road friction and surface roughness.

Figure 5.7 shows the sensitivity of characteristic curve to the variation of cost function weighting factors. The cost function weights are modified proportional to their nominal values. The results demonstrate that the variation of muscle fatigue weight has a greater effect on the characteristic curve's assist gain than the variation of road feel weight, because the cost function is a linear function of the road feel but a quadratic function of muscle activations. These cost function weights can be used to adjust the target steering feel. For example, for a sports car, the driver expects to have stiffer steering than in a comfortable car. To have a more sporty feel, the road feel weighting factor should be increased as shown in Fig. 5.7a, which results in less assistance and a steering system that is therefore more sensitive to road forces.

5.4 Driver-Specific EPS Characteristic Curves

In this section, the sensitivity of the optimal characteristic curves to the variation of muscle parameters has been studied. The maximum assist torque (T_m^{max}) is assumed to be constant and equal to 50 N.m, and a value of 1 N.m is selected for the no-assist zone (T_{d0}) to avoid the off-center steering feel.

To study the effect of variation of muscle parameters on the EPS characteristic curves, first, the muscle parameters are changed separately and the effect of each parameter on the curves is studied. Then, the muscle parameters are modified to the values in Table 5.1, and the EPS characteristic curves are tuned for each driver type.

Figure 5.8 demonstrates the effect of maximum isometric muscle force (F_0^{max}) on the optimal delivered assistance. As expected, a stronger driver with a higher maximum isometric muscle force require less assistance, and consequently more resistive steering torque. In other words, since the stronger driver has stronger muscles, the average value of muscle activations is less compared to a driver with weaker muscles. Therefore, the EPS curve stretches to reduce the assistance. In this case, both bi-linear and sinusoid EPS characteristics curves show the same behavior. Similarly, Figure 5.9 depicts that the assist gain and the slope of assist curves are reduced by increasing the maximum contraction velocity (V_m^{max}) of muscle. As shown in Fig. 5.2a, the amount of generated muscle force at a specific shortening velocity increases by increasing V_m^{max}, which means that a muscle with less V_m^{max} requires more muscle activation to generate the same force than a muscle with higher V_m^{max}, and more driver assist torque.

Figure 5.10 shows the effect of variation of maximum muscle force during the lengthening ($\bar{F}_{len}^{max}$) on the optimal characteristic curves. As shown in Fig. 5.10a, by increasing $\bar{F}_{len}^{max}$, the assistance is reduced for small driver torques and increased for large driver torques in the nonlinear characteristic curves. However, in the bi-linear curves (see Fig. 5.10b), the assist gain is only slightly reduced by an increase of $\bar{F}_{len}^{max}$. Figure 5.11 shows that the variation of passive muscle strain on the assist curves has a negligible effect, since it only affects the passive part of muscle and has no effect on the force generating part of muscle.

Figure 5.12a presents the optimal curves for all four populations. As expected, the

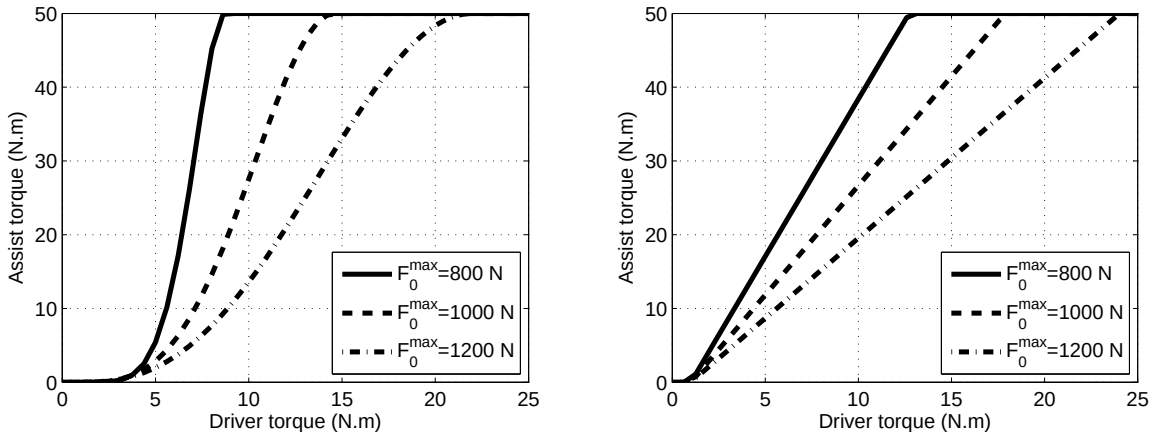

Figure 5.8: The effect of maximum isometric muscle force variation on the optimal assist curves (a) Non-linear characteristic curve, (b) Bi-linear characteristic curve

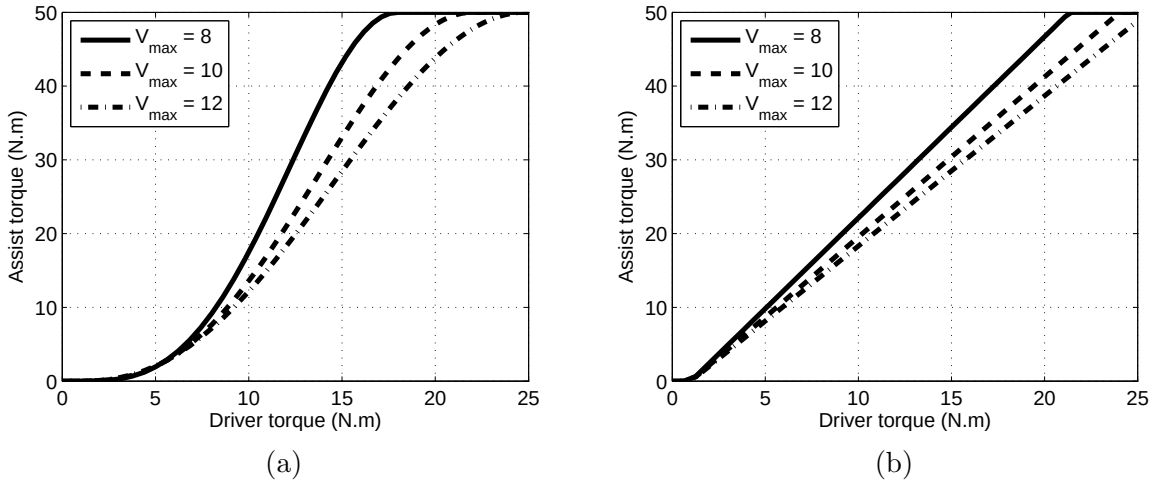

Figure 5.9: The effect of maximum muscle contraction velocity variation on the optimalassist curves (a) Non-linear characteristic curve, (b) Bi-linear characteristic curves

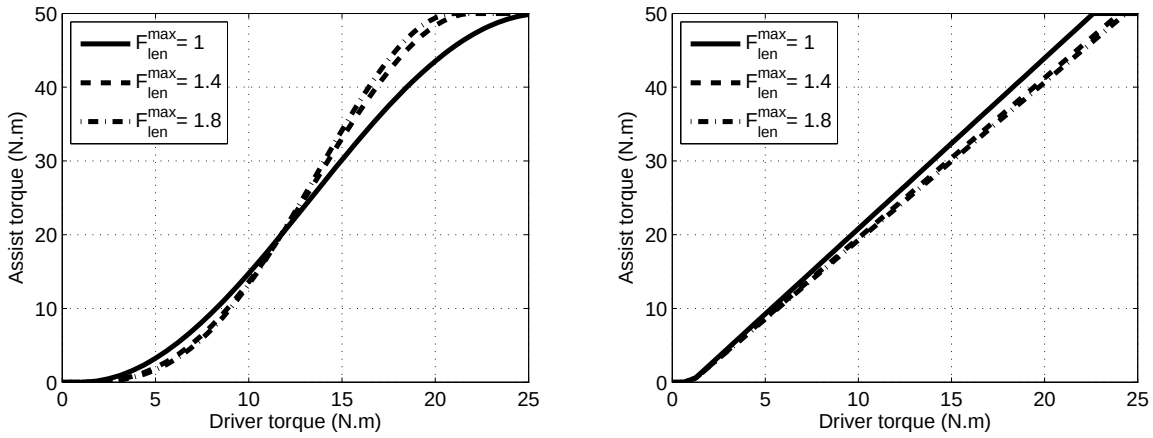

(a) (b)

Figure 5.10: The effect of maximum muscle force during lengthening variation on the optimal assist curves (a) Non-linear characteristic curve, (b) Bi-linear characteristic curve

driver with more strength requires less assistance while perceiving more road information. Therefore, young male drivers require less assistance than young females, old male and old female drivers. Similarly, in the bi-linear curves as shown in Fig. 5.12b, the old female driver requires the most assistance and the young male driver requires the least assistance. Table 5.2 displays the optimal assist gains and optimal shaping factors of the bi-linear and nonliear characteristic curves. In section 5.6.4, the optimal assist gains of the bi-linear characteristic curves will be used in the proposed optimal EPS controller to deliver the proper steering assistance to each population.

Table 5.2: Optimal characteristic curve parameters for young and old adults

#	population	nonlinear characteristic curve $(\kappa,\ T_d^{max})$	bi-linear characteristic curve K_a
1	Young Male	(1.24, 22)	2.17
2	Young Female	(1.63, 13.27)	3.17
3	Old Male	(3.49, 7.7)	4.34
4	Old Female	(5.59, 7.45)	7.4

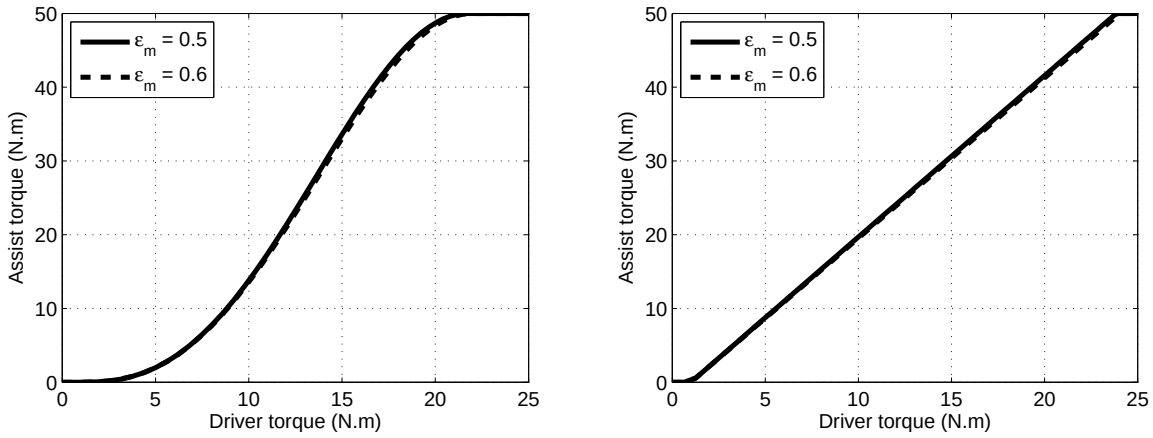

(a) (b)

Figure 5.11: The effect of passive muscle strain variation on the optimal assist curves (a) Non-linear characteristic curve, (b) Bi-linear characteristic curve

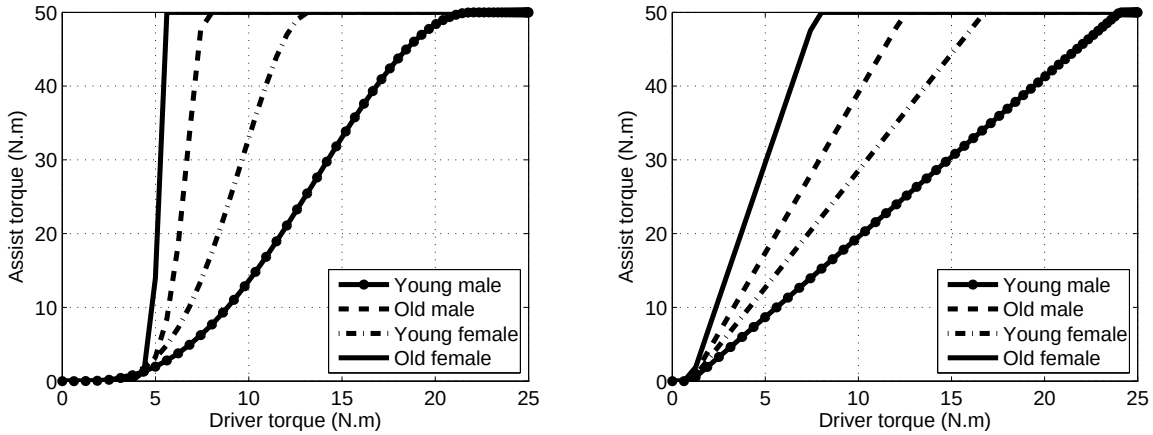

(a) (b)

Figure 5.12: The optimal assist curve for the four driver types (a) Non-linear characteristic curve, (b) Bi-linear characteristic curve

5.5 Optimal Model-Based Controller

Model-based control design is now widely accepted by the automotive industry as a time-saving and cost-effective approach because it enables optimal application of available mathematical-physical knowledge to achieve complex objectives. Compared to static rule-based control, this approach has better performance in the transient response of the vehicle. However, challenges are still posed in practical applications.

In this research, to investigate the application of optimal control to electric power steering systems, an observer-based optimal disturbance rejection controller (modified Linear Quadratic Gaussian - LQG) is presented.

As shown in Fig. 5.13, the steering system is subjected to two exogenous inputs, the driver steering torque (u_τ) and disturbance torque (u_d), and a known input of the electric motor voltage (u_v). The EPS controller should reject or attenuate any unwanted oscillations on the steering wheel while magnifying the driver's steering torque (based on the EPS characteristic curves). Since the driver's steering torque is unknown to the LQG controller, the torque sensor value is used instead of steering torque in the EPS control logic. Therefore, the number of unknown inputs for the controller is reduced to one.

Since not all states of the control-oriented model are measured using the external sensors, some states should be reconstructed using the available measurements and by use of

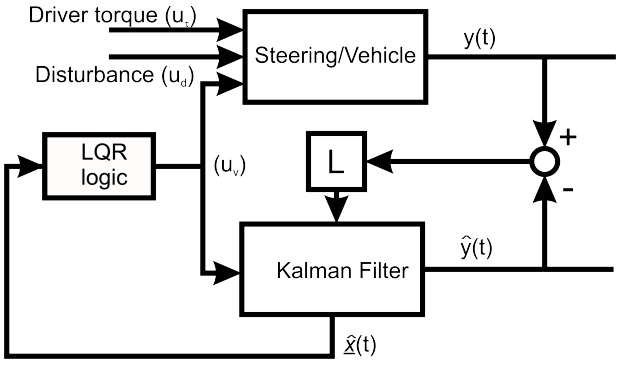

(a)

Figure 5.13: Workflow of the Linear Quadratic Gaussian controller

an observer (Kalman filter). The difference between real ($\mathbf{y}$) and estimated ($\hat{\mathbf{y}}$) value of sensor measurements due to external disturbances and different initial conditions are fed back to the observer (through an observer gain (L)) to adjust the state estimations ($\hat{\mathbf{x}}$) and to identify the external disturbance ($\hat{u}_d$).

The disturbance rejection observer uses an augmented disturbance model to estimate states and unknown disturbances. The observer, based on the idea of modifying the estimation using the difference between the estimated output and actual measurements, predicts the unknown disturbances. Since the driver torque and EPS electric motor current are measured by sensors, sudden changes in the driver steering torque and EPS control voltage are considered to be valid inputs, not disturbances.

Optimal disturbance rejection can be achieved by including a feedforward controller, canceling the effects of the disturbance, into the control logic [66]. Since the external disturbances to the steering systems are unknown, and it is not possible to predict the exact value of a random process beforehand, this method is impractical. However, an effective disturbance rejection can be achieved by including the dynamic properties of the disturbance in the observer and controller design [78, 124]. In this research, the disturbance torque at the intermediate shaft of steering is modeled as a zero-mean colored stochastic process. A shaping filter has been used to transform white noise w into an appropriately stationary random process of disturbance torque ($\hat{u}_d$). This linear shaping factor is defined as follows:

$$\dot{x}_D = A_D x_D + B_D w \tag{5.6}$$

$$\hat{u}_d = C_D x_D + D_D w \tag{5.7}$$

where x_D is the disturbance state, and A_d, B_d, C_d and D_d are shaping filter coefficients. Note that the shaping filter corresponding to Eqs. (5.6) and (5.7) is a causal first order low-pass filter with $D_D = 0$.

By substituting Eq. (5.7) into the state-space representation of the system (Eq. (A.1)

in Appendix A), the new system can be represented as follows:

$$\begin{aligned}\dot{\boldsymbol{x}} &= A\boldsymbol{x} + B_v u_v + B_\tau u_\tau + B_d u_d \\ &= A\boldsymbol{x} + B_v u_v + B_\tau u_\tau + B_d C_D x_D + B_d D_D w\end{aligned} \tag{5.8}$$

where A, B_v, B_τ, B_d and C are respectively the system, input and output matrices of the system, and the inputs to the system are defined as driver torque (u_τ), terminal voltage of electric motor (u_v) and disturbance torque (u_d) at the intermediate shaft (pinion).

Equation (5.8) can be rewritten by forming an augmented state vector $\underline{\boldsymbol{x}}$ including the system states $\boldsymbol{x}$ and the disturbance state x_D such that the dynamics of the system are described by:

$$\dot{\underline{\boldsymbol{x}}} = \underline{A}\ \underline{\boldsymbol{x}} + \underline{B}_v u_v + \underline{B}_w w \tag{5.9}$$

where

$$\underline{\boldsymbol{x}} = \begin{bmatrix} \boldsymbol{x} \\ x_D \end{bmatrix}, \quad \underline{A} = \begin{bmatrix} A & B_u C_D \\ 0 & A_D \end{bmatrix} \quad \underline{B}_u = \begin{bmatrix} B_v \\ 0 \end{bmatrix}, \quad \underline{B}_w = \begin{bmatrix} B_u D_D \\ B_D \end{bmatrix} \tag{5.10}$$

Since the torque sensor value is being used instead of the driver torque in the EPS controller, the driver torque is removed from the control inputs. Similarly, in the observer (Kalman filter) design, the driver torque (Eq. (3.11)) has been removed and the steering wheel angle is assumed to be the input to the system. Therefore, the state variables required for estimation are reduced to $\hat{x} = \begin{bmatrix} \beta & i & r & \theta_r & \dot{\theta}_r \end{bmatrix}^T$ and the system is subjected to only one external unknown input (disturbance torque). The state space representation is as follows:

$$\begin{aligned}\dot{\hat{\boldsymbol{x}}} &= \hat{A}\hat{\boldsymbol{x}} + \hat{B}_u u_v + \hat{B}_\theta \theta_{sw} + \hat{B}_d u_d \\ \hat{y} &= \hat{C}\hat{\boldsymbol{x}}\end{aligned} \tag{5.11}$$

By substitution of Eq. (5.7) into Eq. (5.11) and forming an augmented state vector $\underline{\hat{\boldsymbol{x}}}$ including the system states $\hat{\boldsymbol{x}}$ and the disturbance state x_D, the dynamics of the Kalman

filter system are described by:

$$\begin{aligned} \dot{\underline{\hat{\boldsymbol{x}}}} &= \underline{\hat{A}}\ \underline{\hat{\boldsymbol{x}}} + \underline{\hat{B}}_u u_v + \underline{\hat{B}}_\theta \theta_{sw} + \underline{\hat{B}}_w w \\ \hat{y} &= \underline{\hat{C}}\ \underline{\hat{\boldsymbol{x}}} \end{aligned} \tag{5.12}$$

where

$$\begin{aligned} \underline{\hat{\boldsymbol{x}}} &= \begin{bmatrix} \hat{\boldsymbol{x}} \\ x_D \end{bmatrix}, \quad \underline{\hat{A}} = \begin{bmatrix} \hat{A} & \hat{B}_d C_D \\ 0 & A_D \end{bmatrix}, \quad \underline{\hat{B}}_u = \begin{bmatrix} \hat{B}_d \\ 0 \end{bmatrix}, \\ \underline{\hat{B}}_\theta &= \begin{bmatrix} \hat{B}_\theta \\ 0 \end{bmatrix}, \quad \underline{\hat{B}}_w = \begin{bmatrix} \hat{B}_d D_D \\ B_D \end{bmatrix} \quad \underline{\hat{C}} = \begin{bmatrix} \hat{C} & 0 \end{bmatrix} \end{aligned} \tag{5.13}$$

In this thesis, according to the state equations defined in Eq. (5.12), a Kalman Filter is used as an optimal state estimator as follows [66]:

$$\dot{\underline{\hat{\boldsymbol{x}}}} = \underline{\hat{A}}\ \underline{\hat{\boldsymbol{x}}} + \underline{\hat{B}}_u u_v + \underline{\hat{B}}_\theta \theta_{sw} + L(\mathbf{y} - \underline{\hat{C}}\hat{\mathbf{x}}) \tag{5.14}$$

where

$$L = \Phi \underline{\hat{C}}^T V_2^{-1} \tag{5.15}$$

and V_2 is the intensity of the sensor noise and Φ is the solution to the following Riccati equation.

$$\Phi \underline{\hat{A}}^T + \underline{\hat{A}}\Phi + V_1 - \Phi \underline{\hat{C}}^T V_2^{-1} \underline{\hat{C}} \Phi = 0 \tag{5.16}$$

where V_1 is the intensity matrix of the plant disturbance, which is determined by trial and error.

Based on the separation principle, the optimal control can be determined by feeding the estimated states from the Kalman filter into an optimal state feedback controller. Therefore, the optimal control can be found by rearranging the estimated states and augmenting the known steering wheel angle and velocity to the state vector estimation,

$$u_v = \underline{K}_{FB} \left[\hat{\boldsymbol{x}}^T\ \theta_{sw}\ \dot{\theta}_{sw}\ \hat{u}_d \right]^T \tag{5.17}$$

where

$$\underline{K}_{FB} = R^{-1}\hat{\underline{B}}_u^T P \tag{5.18}$$

and R is a input usage weight (see Eq. (5.21)) and P the solution to the following Riccati equation:

$$P\hat{\underline{A}} + \hat{\underline{A}}^T P + Q - P\hat{\underline{B}}_u R^{-1}\hat{\underline{B}}_u^T P = 0 \tag{5.19}$$

where Q is a state deviation weighting matrix (see Eq. (5.21)).

It is known that the optimal disturbance rejection can be achieved by a full state feedback controller in conjunction with a feedforward controller with a known disturbance. Therefore, it can be seen that by partitioning the feedback gains of the proposed controller into $\underline{K}_{FB} = [K_{FB} \mid K_{FF}]$, the observer-based disturbance rejection controller can have a similar property; it has a feedback function of system states and feedforward function of the estimation of disturbance, as follows:

$$u_v = [K_{FB} \mid K_{FF}] \left[\hat{\boldsymbol{x}}^T \ \theta_{sw} \ \dot{\theta}_{sw} \mid \hat{u}_d\right]^T = K_{FB}[\hat{\boldsymbol{x}}^T \ \theta_{sw} \ \dot{\theta}_{sw}]^T + K_{FF}\hat{u}_d \tag{5.20}$$

The LQG control finds the state feedback gains such that the following cost function is minimized.

$$J = \int_0^\infty \left(\underline{\boldsymbol{x}} \ Q \ \underline{\boldsymbol{x}}^T + \boldsymbol{u} \ R \ \boldsymbol{u}^T\right) dt \tag{5.21}$$

where Q or state deviation weighting matrix is a symmetric positive semi-definite matrix and R or input usage weight is a symmetric positive definite matrix.

In this thesis, the bi-linear characteristic curve as described in section 5.2.2 (see Fig. 5.5a) is used in the LQG controller. The EPS characteristic curves include two intervals: $[0, \ T_0)$ is the interval with no steering assistance, and $[T_0, \ T_{max}]$ is the interval with linear steering assistance. Therefore, for full tracking of characteristic curves in the whole operating region, two control laws are required. The first law is indicating that current of the electric motor should be zero unless there is a disturbance; in the presence of a disturbance the assist torque should cancel the disturbance torque. Therefore, the following cost function

is proposed for the first interval:

$$J_1 = \int_0^\infty \left(q(T_a - K_b\hat{u}_d)^2 + \rho u_v^2\right) dt \tag{5.22}$$

where q and ρ are the tracking and input usage weights, and K_b is the disturbance rejection feature switch. The disturbance rejection module is turned off when K_b is equal to zero, and it is enabled when K_b is equal to one.

The second interval suggests that the assist torque be proportional to the torque measured by the torque sensor. To construct the state-space representation, the state variables are defined as $\boldsymbol{x} = \begin{bmatrix} \beta & i + K_a T_{a0} & r & \dot{\theta}_r & \theta_{sw} & \dot{\theta}_{sw} \end{bmatrix}^T$. To ensure the improvement of steering feel by attenuation of the disturbance torque, the following cost function has been used in the second interval:

$$J_2 = \int_0^\infty \left(q(T_a - T_a^{des} - K_b\hat{u}_d)^2 + \rho u_v^{*2}\right) dt \tag{5.23}$$

where

$$T_a^{des} = K_a K_{tb} \left(\theta_{sw} - \theta_r\right) \tag{5.24}$$

Here, T_a and T_a^{des} are actual and desired assist torques and u_v^* is the modified terminal voltage of the electric motor ($u_v^* = u_v + K_a R T_0$), where T_a^{des} is proportional to the torque sensor value, and K_a is the EPS assist gain.

By substituting Eqs. (5.24) and (3.9) into Eq. (5.23) and expanding the equation, the Q and R in their standard integral quadratic form as shown in Eq (5.21) for the second interval can be described by:

$$Q = q \begin{bmatrix} 0 & 0 & 0 & 0 & 0 & 0 & 0 & 0 \\ 0 & G^2K_e^2 & 0 & GK_aK_eK_{tb} & 0 & -GK_aK_rK_{tb} & 0 & K_bGK_e \\ 0 & 0 & 0 & 0 & 0 & 0 & 0 & 0 \\ 0 & GK_aK_eK_{tb} & 0 & K_a^2K_{tb}^2 & 0 & -K_a^2K_{tb}^2 & 0 & K_bK_aK_{tb} \\ 0 & 0 & 0 & 0 & 0 & 0 & 0 & 0 \\ 0 & -GK_aK_eK_{tb} & 0 & -K_a^2K_{tb}^2 & 0 & K_a^2K_{tb}^2 & 0 & -K_bK_aK_{tb} \\ 0 & 0 & 0 & 0 & 0 & 0 & 0 & 0 \\ 0 & K_bGK_e & 0 & K_bK_aK_{tb} & 0 & -K_bK_aK_{tb} & 0 & K_b^2 \end{bmatrix} \quad R = \rho \tag{5.25}$$

The weights of current error (q) and terminal voltage (ρ) in cost functions J_1 and J_2 are chosen by trial and error to ensure that the current of electric motor will track the desired current with minimum electric motor terminal voltage.

5.6 Simulation Results and Discussion

To evaluate the performance of the proposed controller, closed-loop simulations with the high-fidelity vehicle and driver model are required. In this section, first, the effects of assist gain variation and the effect of disturbances on the performance of the controller have been studied using the high-fidelity vehicle model alone. Then, the 3D driver model steering the high-fidelity vehicle model is used to evaluate the performance of EPS controller with the already found optimal characteristic curves for the four driver types.

To study the robustness of the EPS controller to different assist gains, a sinusoidal steering maneuver is performed. In these simulations, the vehicle speed is equal to 10 m/s and the length of no-assist zone (T_{a0}) is set to 1 $N.m$. The Disturbance Rejection (DR) module is switched off ($K_b = 0$) and K_a is set to 0.5, 1 and 2, consecutively. As shown in Fig. 5.14 the proposed controller can closely follow the desired assist curves with different assist gains.

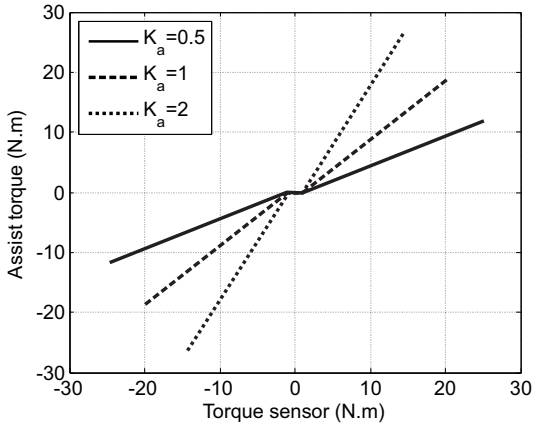

Figure 5.14: The produced assist torque versus torque sensor value with different assist gains

Second, to study the performance of the controller in a real-world condition, two maneuvers have been used. In the first maneuver, the vehicle is driving in a straight lane while suddenly a step-like disturbance torque (Fig. 5.16a) is applied to the steering column. In the second maneuver, the driver performs a sinusoidal slalom-like maneuver, in the presence and absence of a disturbance torque. In both cases, the vehicle speed is equal to 10 m/s and the assist gain (K_a) is set to 3 $N.m$.

5.6.1 Straight-line Driving Maneuver

In the first maneuver, while the vehicle is driving in a straight lane, three conditions have been applied to the EPS controller: the EPS system is off, the EPS system is enabled but the DR module is off, and the EPS system is fully functional. As shown in Fig. 5.15 with the given disturbance, the first situation has the largest steering wheel angle variation while in the second situation, the assistance module enables the driver to produce more resistive torque which results in less steering wheel angle variation. In the third situation, when the DR module is on, the EPS controller estimates the disturbance automatically and produces a counter torque at the steering wheel, so the effects of the disturbance are greatly reduced at the steering wheel.

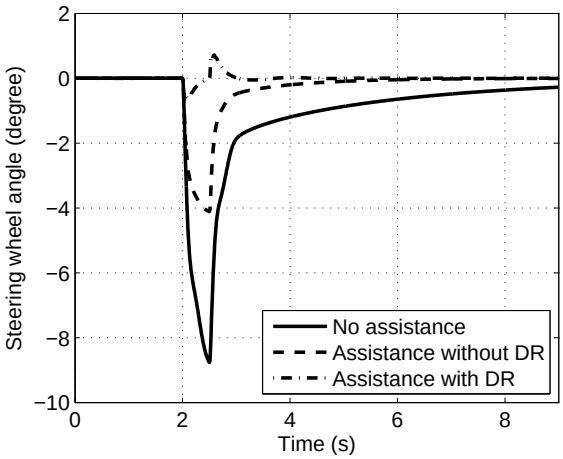

Figure 5.15: Comparison of the steering wheel angles in the straight line simulation in presence of a step-like disturbance

Fig. 5.16a shows the performance of the Kalman filter in the estimation of the external disturbance. It should be noted that Coulomb friction between the rack and rack housing is also considered as a disturbance since it is not included in the control-oriented model and it acts as an external force to the rack. Fig. 5.16b shows the assist torque produced by the EPS controller; it can be seen that the estimated disturbance is effectively used by the disturbance rejection module of EPS controller to reduce the transferred disturbance to the driver's hands.

5.6.2 Slalom Driving Maneuver

In the second maneuver, a sinusoidal rotation of steering wheel with frequency of 0.5 Hz and amplitude of 50 degrees is performed, and similar situations to the first maneuver have been studied in the presence and absence of an external disturbance.

In the first case, without the existence of any external disturbances, the performance of the controller for all three situations has been studied. As shown in Fig. 5.17a when the DR module is off, the assist curve is equal to its nominal value (bi-linear curve) as expected; however, when the DR module is enabled, the EPS controller produces more or less assist

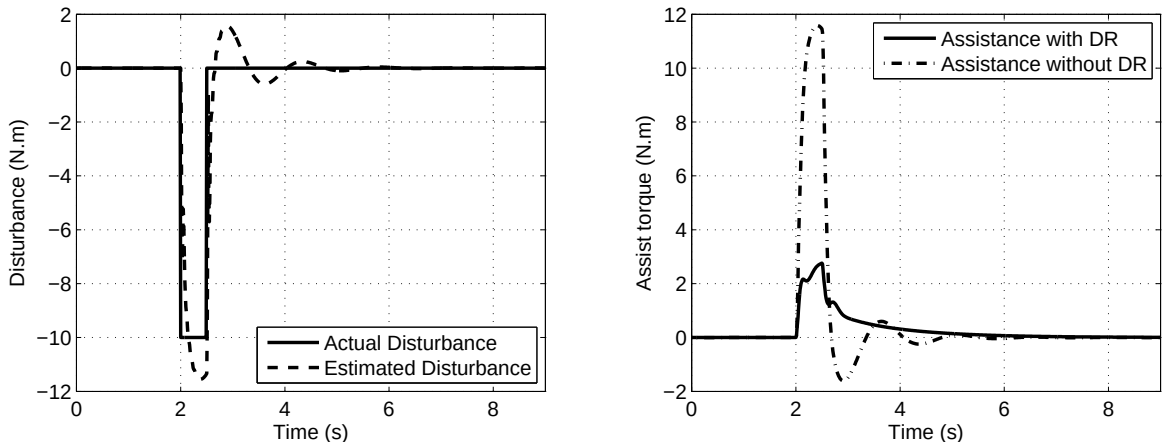

(a) (b)

Figure 5.16: (a) Comparison between the actual and estimated value of disturbance, (b) Torque sensor measurement when DR module is on and off

torque based on the estimated value of disturbance (as shown in Fig. 5.18a). Since there is no external disturbance to the system, the estimated value represents the friction present in the steering system and the virtual force that deviates the steering system from its linear response.

Figure 5.17b shows the torque sensor (driver torque) value against the steering wheel angle (the so called Lissajous curves) for all the aforementioned situations. It can be seen that in the no-assist zone, the Lissajous curves in all the situations are on top of each other, which represents the regular behavior (without EPS) of the steering system. In the linear assist zone, the driver's torque is significantly reduced since the controller is producing the assist torque proportional to the steering torque. A reduction in the area inside the required steering torque curve when the DR module is on in comparison with the control without DR can be observed since the EPS controller is compensating for the friction present. It can be also noted that the EPS controller with DR leads to a linear response while the behavior of the system is nonlinear.

Figure 5.18b shows the torque sensor value in all aforementioned situations. As expected, the steering torque for the case without assistance is higher than the other cases,

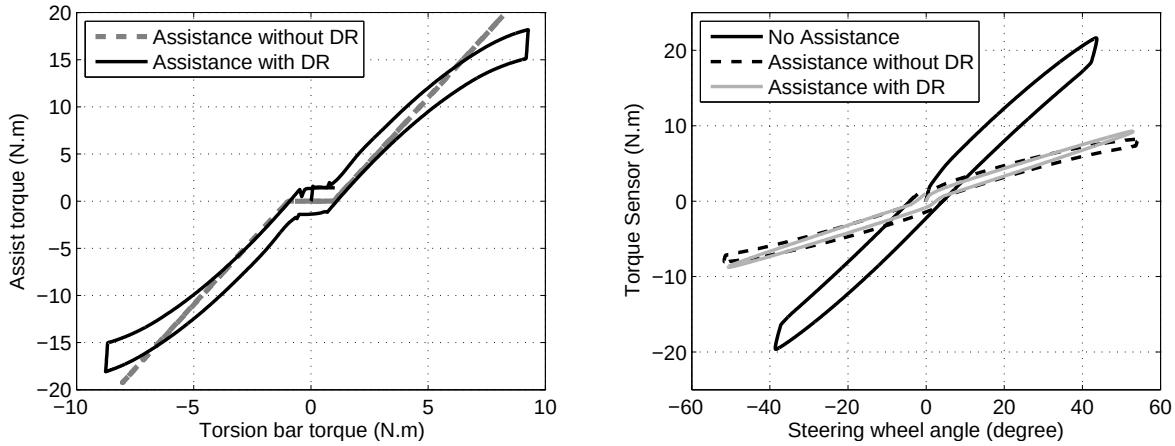

(a) (b)

Figure 5.17: Simulation of the proposed EPS controller applied to the high-fidelity vehicle model in a smooth steering maneuver (a) The produced assist torque versus torque sensor value in the absence of external disturbance with and without the DR module, (b) The required steering torque versus the steering wheel position in the absence of external disturbance with and without the DR module

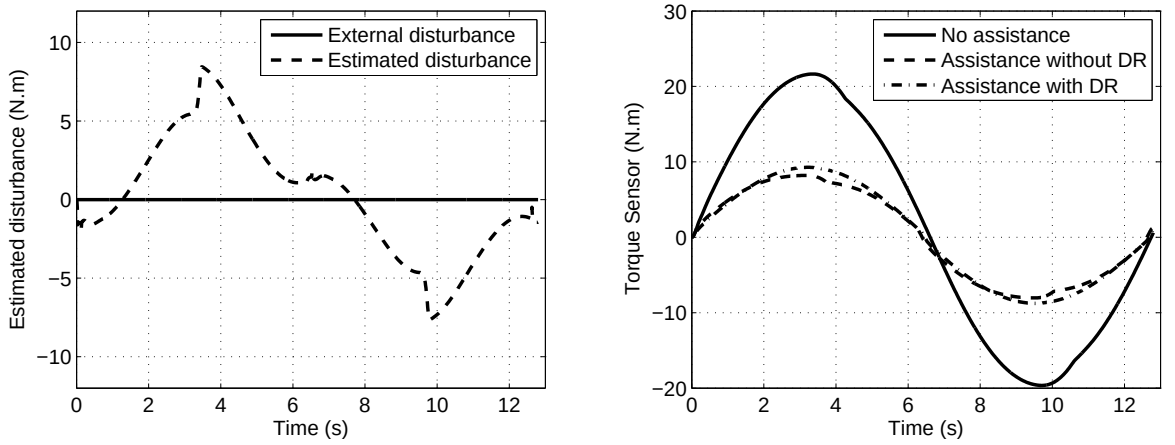

(a) (b)

Figure 5.18: (a) Comparison between the actual and estimated value of disturbance, (b) Comparison of the required driver torque with and without EPS controller in a sinusoidal steering maneuver

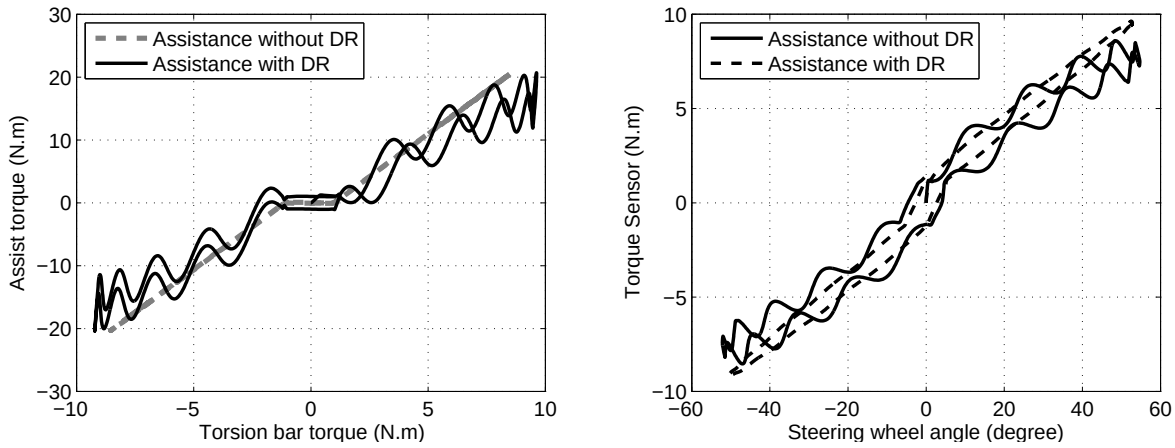

(a) (b)

Figure 5.19: Simulation of the proposed EPS controller applied to the high-fidelity vehicle model in a smooth steering maneuver (a) The produced assist torque versus torque sensor value in the presence of external disturbance with and without the DR module, (b) The required steering torque versus the steering wheel position in the presence of external disturbance with and without the DR module

and the steering torque when the DR module is on is slightly higher than the situation without DR since the controller is enforcing a linear response to the steering system.

In the second maneuver , in the presence of an external disturbance, the effectiveness of the DR module in a realistic steering maneuver has been studied. As shown in Fig. 5.19b, in the situation when the DR module is off, the Lissajous curve is contorted, meaning that the disturbances are transferred to steering wheel and the driver's hands (see fig. 5.20b). In the third situation (EPS on, DR on), these oscillations are significantly reduced because the EPS controller uses the estimated value of disturbance to attenuate the oscillations on the steering wheel. As shown in Fig. 5.19a, the produced assist torque, when the DR module is on, is highly nonlinear while the assist torque when the DR is off is bi-linear.

Fig. 5.20a shows the estimated value of disturbance in comparison with the external disturbance; similar to Fig. 5.18a, it should be noted that the friction forces are also included in the estimated value of disturbance. Figure 5.20b shows the torque sensor value

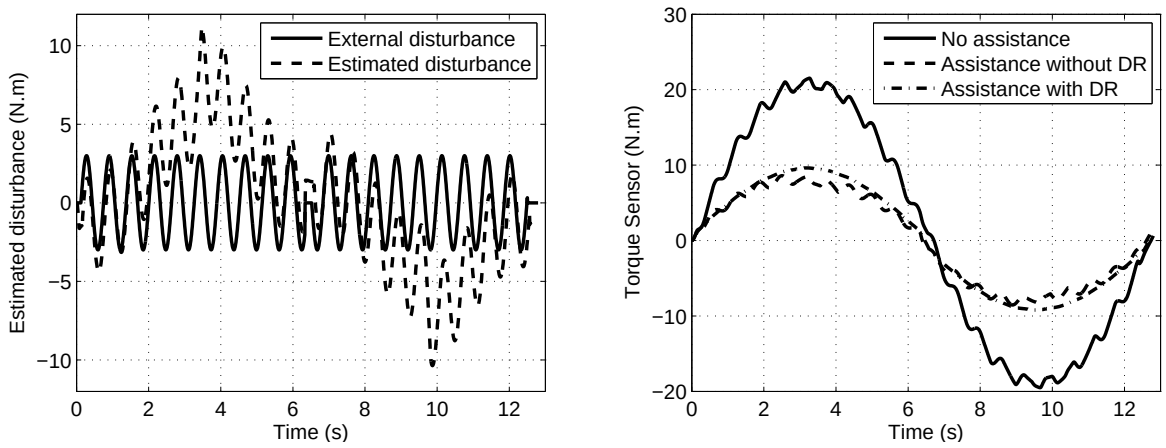

(a) (b)

Figure 5.20: (a) Comparison between the actual and estimated value of disturbance, (b) The required steering torque with and with out the proposed EPS controller

for all aforementioned situations. In the case with enabled DR module, the disturbance is successfully attenuated and the behavior of the system is linear.

5.6.3 Slalom Driving Maneuver with Measurement Noise

It is known that the Kalman filters can remove the noise from the measurement signals by considering a predefined model of the system. In this research, a similar scenario to the sinusoidal steering input with corrupted measurement signals are studied. Since the torque sensor is measuring the transferring torque through the torsion bar, it has more tendency to absorb noise; however, in this section, all of the observer outputs are corrupted by a Gaussian noise. Fig. 5.21 shows the corrupted and reconstructed torque sensor and yaw rate values. It can be seen that the reconstructed signals are noise-free and conveying the correct dynamics of the system.

As shown in Fig. 5.22, the performance of the controller (when the DR module is on and in the presence of measurement noise) is not degraded in comparison with the case without measurement noise.

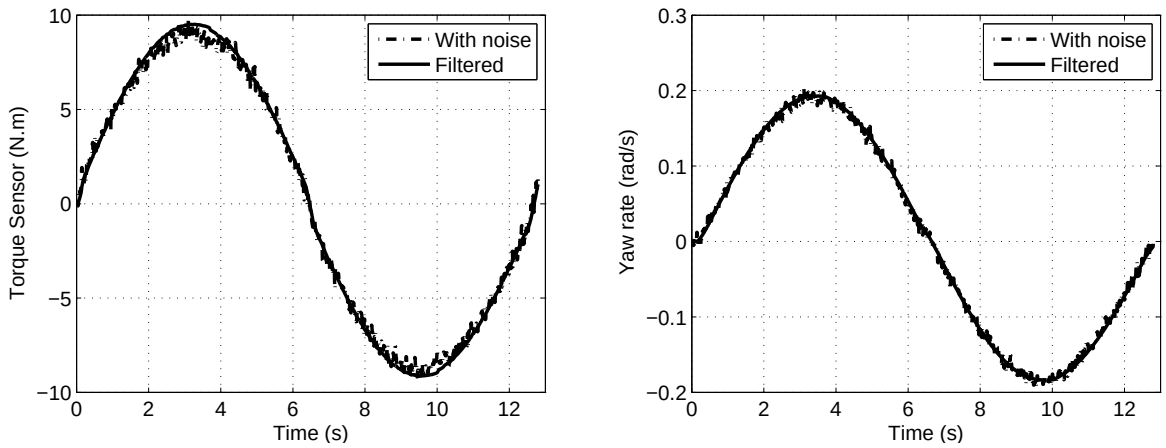

(a) (b)

Figure 5.21: Corrupted and reconstructed measurement signals (a) Torque sensor, (b) Vehicle yaw rate

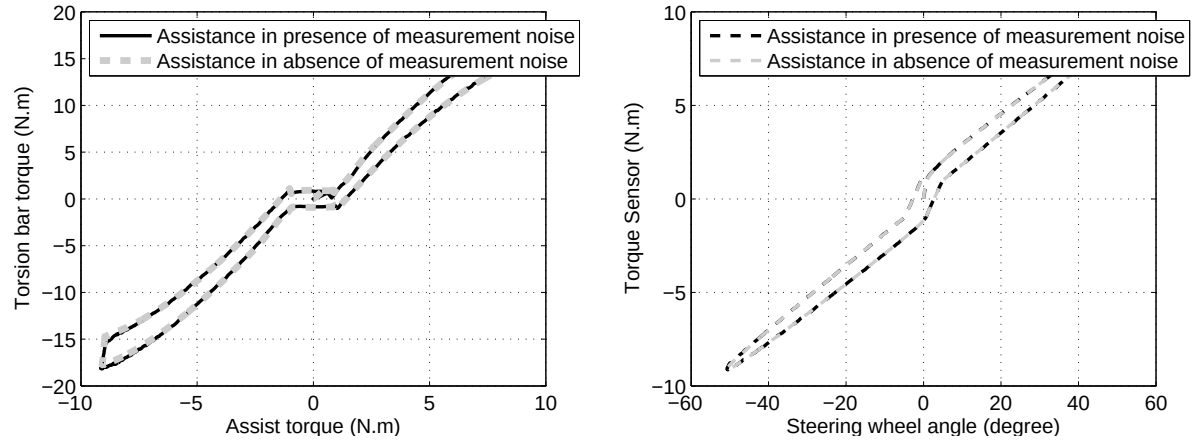

(a) (b)

Figure 5.22: Simulation of the proposed EPS controller applied to the high-fidelity vehicle model in a smooth steering maneuver (a) The produced assist torque versus torque sensor value in the presence of measurement noise with the DR module, (b) The required steering torque versus the steering wheel position in the presence of measurement noise with the DR module

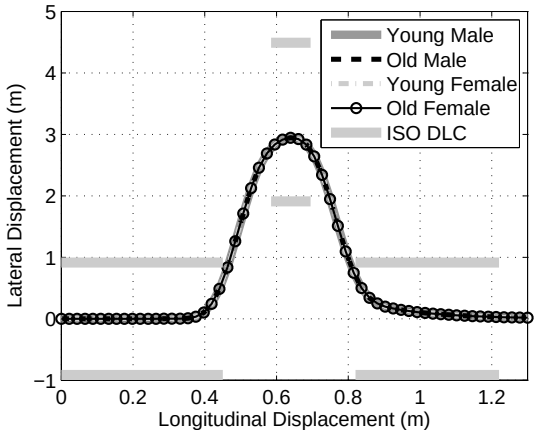

Figure 5.23: The vehicle trajectory of the four driver types performing an ISO double lane-change (DLC) maneuver.

Since the steering wheel angle is the input to the observer, the steering wheel angle is left noise free; however, in the case of a corrupted steering wheel angle measurement, a separate filter should be designed for this signal.

5.6.4 Double Lane-Change Maneuver with Driver-Specific EPS Controller

In this section, to study the performance of the driver-specific EPS controller, the tuned controllers are evaluated using the high-fidelity vehicle-driver model. The muscle parameters of the 3D driver model (as described in section 4.4 - steering with two hands) are adjusted to represent the corresponding group, i.e. young male, old male, young female, old female. Then each group performs a double lane change maneuver with the the high-fidelity vehicle model at the speed of 10 m/s.

As shown in Fig. 5.23, the vehicle lateral displacements of all groups are similar to each other and to the desired trajectory, and they are all within the ISO double-lane change maneuver constraints. Therefore, the resistive steering torque in all of the simulations are the same, since the driving conditions in all of the simulations are the same.

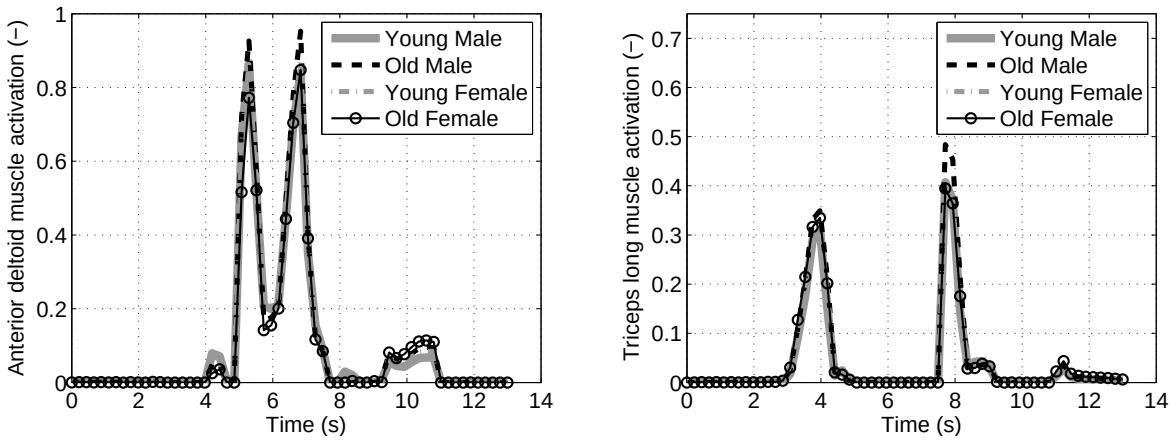

(a) (b)

Figure 5.24: Right hand's muscle activities during a double lane-change maneuver for the four driver types (a) Anterior portion of deltoid, (b) Long head of triceps

Figure 5.24 shows the predicted muscle activities of the anterior portion of deltoid and the long head of triceps of the driver's right arm for the four predefined driver types. Although other muscle activations are not presented here, a similar behavior can be seen in other muscles. As shown in this figure, the magnitude and trend of these patterns are very similar. Although young male drivers have higher physical strength than old female drivers, the portion of motor units that have been recruited by the central nervous system are the same. In conclusion, the drivers' muscle (physical) fatigue are equal, thereby satisfying the controller objective to provide equal assistance to all drivers.

It should be noted that the EPS controller has been tuned based on a simplified vehicle model and the 2D driver model, but the tuned controller is evaluated using the high-fidelity vehicle model steered with a 3D driver model with two hands on the steering wheel, which shows the same expected behavior. Therefore, it can be concluded that the simplified 2D driver model is a good and efficient model to be used in the design optimization procedures of the active steering systems.

5.7 Chapter Summary

In this chapter, first, drivers are categorized into four types: young male, old male, young female and old female. Then, the muscle dynamics of each group are identified and the muscle parameters are adjusted to represent each group. Second, two EPS characteristics curves are introduced, and a systematic way to tune the curves for the four defined driver types are presented.

Then, an observer-based disturbance rejection controller for electric power steering systems is proposed. To construct the EPS controller, the LQG control approach with separate observer and controller has been used. A Kalman filter augmented with a shaping filter is used to estimate the unmeasured states and the external disturbances to the steering system. Simultaneously, the estimated states and the disturbance is used in the LQR controller with a new formulation of control objective function to actively cancel the disturbances while magnifying the driver's steering torque.

The proposed EPS controller is evaluated in a software-in-the-loop simulation using a high-fidelity vehicle model to ensure the robust performance of the controller in a real-world condition. In the case with no external disturbance to the system, the disturbance observer estimates the steering's component frictions, which is deviating the system states from their linear response. Similarly, in the presence of an external disturbance, the identified disturbance is the combination of friction and external disturbance. Removing this identified disturbance from the system reduces the driver torque, thereby enforcing the linear response of control-oriented model to the system. Therefore, the proposed EPS controller improves the steering feel by reducing the required steering torque and reducing the oscillations due to road irregularities. Finally, the driver-specific EPS controllers are verified against the high-fidelity vehicle-driver model adjusted for that specific group. The results showed that the tuned EPS controller can equally assist drivers with different physical strength. The proposed LQG controller has strong robustness properties against measurement noise and external disturbance. The simulation results show that it can efficiently attenuate the interference caused by random road excitation and can competently work with corrupted measurements.

6

Conclusions and Future Work

In this chapter, the contributions of the conducted research (interaction of driver with steering system) to the study of steering tasks and the design of electric power steering (EPS) systems are discussed. Since the steering system is a device that interacts with a human, the large part of this research is focused on the neuromusculoskeletal dynamics of a driver and how it interacts with the steering system. EPS systems improve the steering experience by reducing the physical effort of drivers and at the same time by ensuring the stability of the vehicle and providing necessary information to drivers from the surrounding environment such as road friction and surface roughness. However, it is known that the steering feel is a subjective criteria and the steering feel satisfaction level is varied for different drivers with different driving habits and physical abilities.

In this thesis, the effects of musculoskeletal dynamics of the driver arm as well as the driver's cognition delay and response time (voluntary and involuntary) on steering tasks have been studied and possible guidelines to improve the steering feel have been investigated. Then, the findings in this area have been applied to an EPS controller to improve the steering feel.

In the following sections, the different research challenges that have been faced in this study will be discussed.

6.1 High-Fidelity Integrated Driver-Vehicle Interaction Model

Having a clear understanding about the dynamical system is crucial in designing control systems, since not only does it strengthen our knowledge about the system but also it reduces development time and cost. In this research, to facilitate the interpretation of the result, a high-fidelity vehicle model and a driver model, consisting of a central nervous system and a musculoskeletal arm model holding the steering wheel, are developed in silico to replicate the interaction between the driver and vehicle.

The high-fidelity model of vehicle consists of MacPherson and multilink suspension systems at the front and rear as well as a column-assist electric power steering system (for details see Chapter 3). The musculoskeletal arm model consists of the thorax, humerus, forearm and hand. The thorax is assumed to be fixed on the driver seat, and connected to the humerus using a three degree-of-freedom shoulder joint. The humerus connects to the forearm using a hinge joint allowing the flexion/extension of the elbow. The wrist joint is modeled by a universal joint simulating the lateral and vertical movements of the hand, which is firmly holding the steering wheel. The developed arm is covered by eight muscles around the shoulder and seven muscles around the elbow (for details see Chapter 4). The muscular functionality of the arm model is validated using electromyography of a driver performing on-center steering and sinusoidal steering maneuvers.

6.2 Motor Control Framework

The fully integrated driver-vehicle model requires a command center to monitor and coordinate the driver's arm movements to steer the steering wheel, and consequently to control the vehicle movements. This command center in humans is known as the central nervous system (CNS), which consists of brain and spinal cord. The CNS requires sensory information and visual feedback to sense the position and orientation of the body members relative to each other and in the global frame. Then, the CNS uses this information to coordinate the bodies to perform a desired motion by stimulating the appropriate motor control units.

In this thesis, a hierarchical approach is used to capture the complexity of neuromuscular dynamics and the central nervous system in the coordination of the driver upper limb activity. The proposed motor control framework has three layers: the first layer is responsible to find the proper steering wheel angle to follow a desired path (path-planning layer), the second layer is responsible for actuating the arm (force distribution controller), and the final layer is added to ensure better control precision and disturbance rejection of the motor control (stabilizer layer). The following sections discuss the challenges that have been addressed in the development of a human-like neuromusculoskeletal driver model in this research.

6.2.1 Path-Planning Controller and Driver's Steering Skill

To consider the predictive ability of a human driver in the proposed motor control framework, a model predictive controller (MPC) is employed in the path-planning layer to plan the vehicle's desired trajectory. In Chapter 4, the effects of prediction horizon and control horizon lengths on the predicted trajectory have been studied. The prediction horizon represents the driver's line of sight, and it is shown that the maximum steering angle predicted by MPC is proportional to the prediction horizon. In this research, the control horizon is used to regulate the computational load of the MPC, without altering the predicted trajectory.

As discussed in Chapter 4, the cerebellum contains an internal model of the motor control apparatus as well as the environment with which it is interacting. This model represents the internal cognition of driver from his/her body and the surrounding environment; in this case, the surrounding environment is the steering wheel and vehicle.

In this thesis, it is assumed that a skilled driver has a developed/detailed understanding of the vehicle behavior, while a novice driver considers the vehicle as a point-mass with a linear behavior. It is also hypothesized that the internal vehicle model is stored as a family of linearized vehicle models in the cerebellum, and the size of this set represents the driver's steering skill. Therefore, a bicycle model of the vehicle with a nonlinear tire model is used as the internal representation of vehicle in the cerebellum and to represent a skilled driver, the nonlinear vehicle model should be linearized at multiple operating points. However, in the simulations, the vehicle model only is linearized at the equilibrium point to manage the computational load.

6.2.2 Steering Wheel Coordination

The main responsibility of the CNS is the coordination of the driver's upper limb. The path-planning controller passes the desired steering wheel angle to the force distribution controller to find the required muscle activations to rotate the steering wheel to the desired position.

The driver's musculoskeletal arm is actuated with fifteen muscles while it only has one degree-of-freedom. This configuration represents an indeterminate dynamical system. To solve this indeterminacy problem a forward static optimization (FSO) approach is used, engaging a cost function to produce the physiologically possible motions. In this thesis, a muscle fatigue criterion enhanced with a muscle co-contraction ratio is used as the physiological cost function. Then, the optimal muscle activations are sent to Hill-type muscle models to calculate the muscle forces required to perform the desired steering motion.

6.2.3 Disturbance Rejection and Precision Control

Stretch reflex, joint stiffness modulation and voluntary disturbance rejection mechanisms are used by the CNS for the precision control and the attenuation of disturbances applied to the upper limb. If the steering wheel is perturbed with an external disturbance, the unexpected position of the hand or the steering wheel is quickly sensed by visual and proprioceptive sensory organs and is sent to the CNS. The muscle length and velocity errors are processed locally in the spinal cord and appropriate commands are sent to the corresponding motor control units. The response of this locally processed mechanism (or so-called stretch reflex) is involuntary and only activates when a muscle unexpectedly stretches.

The muscle length and velocity and other sensory information are also sent to the higher brain centers for further interpretation of the situation and to counteract the disturbance. This mechanism (or so-called voluntary disturbance rejection) is modeled using a closed-loop disturbance observer. The disturbance observer compares the actual steering wheel angle to its expected value; in the presence of any difference, a proportional-derivative controller on the error with a time delay is used to estimate the disturbance torque at the steering wheel. Then, the estimated disturbance torque is sent to the force distribution controller to provide necessary muscle activations to counteract the disturbance torque.

Joint stiffness modulation is the other mechanism used by the CNS to attenuate disturbances. In this case, the driver increases the shoulder and elbow rotational stiffness by co-contracting the muscles around the joints. In the presence of a disturbance, the deviation of joint angle from its expected value is less than when the muscles are not co-contracted. In this thesis, the muscle stiffness modulation is implemented by increasing the shoulder and elbow stiffness and damping coefficients proportional to the muscle co-contraction ratio.

6.2.4 Relaxed and Tensed Steering Conditions

It is observed that novice drivers or drivers in an unknown environment tend to co-contract their muscles to increase the steering accuracy and the steering impedance. In this thesis, to capture this dynamics, two different steering conditions are introduced: tensed and relaxed conditions.

In the relaxed condition, no muscle co-contraction is considered while the time delay of voluntary disturbance rejection is assumed to be very long. On the other hand, in the tensed steering condition, the muscle co-contraction ratio is assumed to be 30% for shoulder and elbow muscles, and the time delay to identify the perturbation for the voluntary disturbance rejection is assumed to be 0.3 s.

6.3 Electric Power Steering Controller

Electric Power Steering (EPS) systems are used to reduce the physical effort of the driver during steering tasks and to provide a good steering feel while ensuring the stability of the vehicle.

In this thesis, an observer-based disturbance rejection EPS controller is developed. This controller consists of a LQR and a Kalman filter with a new formulation to actively cancel disturbances while magnifying the driver's steering torque. To provide a better steering feel, the characteristic curves are tuned for predefined groups of drivers. In the design process of the EPS controller, the following challenges have been faced and addressed.

6.3.1 Control-Oriented Model and Two-Dimensional Driver Model

The developed high-fidelity vehicle model is a nonlinear multibody dynamical model, and is not suitable for model-based controllers. Therefore, to design a model-based EPS controller, a control-oriented model is developed and validated against the high-fidelity model. The control-oriented model conveys the necessary information about the lateral dynamics

of the vehicle as well as the EPS dynamics. The control-oriented model consists of a linear bicycle model of a vehicle equipped with a column-assist EPS system. In this model, the longitudinal velocity of the vehicle is assumed to be constant and the interaction between tire and road is simulated using a linear tire model.

Since the three-dimensional (3D) driver model is very complex and computationally expensive, it cannot be used efficiently in the optimization process. Therefore, in this thesis, a simplified two-dimensional (2D) driver model is developed to capture the important dynamics of the arm, and to reduce the simulation time.

In the 2D driver model, the elbow is assumed to be locked, and the shoulder only allows motion in the saggital plane. In this model, a pair of agonist and antagonist muscles is used to represent the group of muscles that are producing the clockwise and counterclockwise steering torques. Since the number of muscles in the 2D driver model are reduced to two, a PID controller with a splitter that separates the positive and negative torques is used instead of the FSO approach. Using this simplifications, the simulation time is significantly reduced.

6.3.2 Driver-Specific EPS Controller

In this research, four driver types are defined based on the driver's physical characteristics such as age and gender: young male, old male, young female and old female. The physical characteristics of each group is represented in the 2D driver model by adjusting the muscle model parameters. Then, in the design optimization procedures, the adjusted 2D driver model and a simplified vehicle model is used to tune the EPS characteristic curves to have a similar steering feel (activation patterns) and road feel for all drivers. The muscle fatigue calculated from the 2D driver model is used to quantify the steering feel. In other words, the EPS controller can equally assist and improve the steering feel for different populations.

6.3.3 Controller Robustness and Stability

Since drivers directly interact with an EPS system, the EPS system must be stable and robust to ensure safety. In this research, the LQG control strategy guarantees the stability of the system with infinite gain margin and the 60 degrees phase margin under linear conditions. However, the robustness of the LQG controller should be independently verified.

In this thesis, the robustness of the controller in the presence of external disturbances and measurement noise has been studied. The simulation results show that the EPS controller can efficiently attenuate the interference caused by road random excitation and can competently work with the corrupted measurements. The robustness of the controller against the changes in the system parameters such as mass and inertia of steering linkages has been investigated for an early version of this controller [91]. The simulation results show that the modified LQG controller is robust against small changes in system parameters.

6.3.4 EPS Controller Evaluation

Designing a complex product typically requires many trial and error experiments, which is a time-consuming and costly approach. A strategy that usually is adopted by car manufacturers to reduce the development time is to perform experiments using software-in-the-loop (SIL) simulations before testing on a real vehicle. SIL simulations provide a platform to consider the complexity of the real vehicles via computer simulations. In this thesis, the EPS controller is evaluated in SIL simulations using the high-fidelity driver-vehicle model. The high-fidelity vehicle model used in this thesis is verified against an experimentally validated ADAMS model, and the driver model is validated against the published research articles. SIL simulations using the high-fidelity integrated driver-vehicle model ensures the robust performance of the controller interacting with a human driver in a real-world condition.

6.4 Summary of Contributions

The research contributions of this thesis can be summarized as follows:

- Development of a high-fidelity integrated driver-vehicle model to study steering tasks
- Development of a high-fidelity model of a vehicle equipped with a column-assist electric power steering system in MapleSim. The model is verified against an experimentally validated ADAMS model.
- Development of a fully neuromusculoskeletal driver model, validated with the data published in the research articles, considering the bone and muscle geometry of the driver's arm in MapleSim
- Development of a simplified (2D) driver model to be used in the optimization procedures
- Improvement in the disturbance rejection control of the driver model by considering a disturbance observer, muscle stretch reflex and joint stiffness modulation
- Development of an observer-based disturbance rejection controller with new objective function formulation for electric power steering systems
- Quantifying the muscle fatigue to represent the steering feel
- Considering age and gender in the EPS control design to improve the steering feel for a predefined group of drivers
- Development of a systematic way to tune the EPS characteristics curves

6.5 Recommendations for Future Research

The research described in this thesis contributes to better understanding of neuromusculoskeletal modeling of driver and improvement of driver-assist technologies. There are several areas where further research would be beneficial:

- The next step that naturally follows the software-in-the-loop simulations (using the validated integrated driver-vehicle model) is to verify EPS controllers using Driver-in-the-loop simulations. A set of driver-in-the-loop simulations can be conducted to ensure the performance of tuned EPS controllers. For these simulations, a driving simulator can be used to implement the different EPS controllers to study different drivers within a predefined driver group. Electromyography activities of driver's upper limb muscles should be measured to verify the validity of the proposed hypotheses.

- An additional set of electromyography activities of driver upper limb can be used to further validate the driver's arm model. Since some of the parameters of driver model are adopted from the published data or optimization, further experiments can be designed to verify these parameters.

- A three-element Hill-type muscle model can be used instead of two-element muscle model to enhance the fidelity of muscle model and to physiologically replicate the joint stiffness induced by muscle co-contraction.

- Scapula and the muscles holding it are one of the major locations of shoulder injuries; therefore, the scapula should be added to the driver's arm model to study shoulder injuries during steering tasks; and more importantly, to develop a more accurate model.

- The 3D driver model can be used in the driver ergonomic studies to find the best position and orientation of steering wheel or driver seat as well as other driver-assist devices.

- The 3D driver model can be used as a stand-alone model to study human upper-extremity movements. For example, this model can be easily adjusted to hold other devices such as a rehabilitation robot. The interaction between the patient's hand and robot can be extensively investigated.

- The muscle fatigue calculated from the neuromuscular driver model can be used to dynamically adjust the EPS characteristic curve. For example, in a long and extreme

maneuver where a continues amount of activation is required, the assist gain can be increased to hold the fatigue at a constant level.

- A separate filter can be designed for the case with corrupted steering wheel angle measurements to improve the EPS controller's disturbance rejection performance as well as providing proper assistance.
- An adaptive approach can be used to learn a driver's characteristics and use this information to provide appropriate assistance to the driver.

References

[1] Muscle co-contraction modulates damping and joint stability in a three-link biomechanical limb. *Frontiers in neurorobotics*, 5:5, 2011.

[2] D. Abbink. *Neuromuscular Analysis of Haptic Gas Pedal Feedback During Car Following*. PhD thesis, Delft University of Technology, Delft, The Netherlands, 2006.

[3] U. Ackermann. *PDQ: Physiology*, volume 95. McGraw-Hill Europe, 2002.

[4] F. Adams. Power Steering Road Feel. In *SAE Technical Paper, Paper Number: 830998*, 1983.

[5] F. Anderson and M. Pandy. Dynamic Optimization of Human Walking. *Journal of Biomechanical Engineering*, 123(5):381, 2001.

[6] F. Anderson and M. Pandy. Static and Dynamic Optimization Solutions for Gait are Practically Equivalent. *Journal of Biomechanics*, 34(2):153–161, 2001.

[7] B. Armstrong and D. Canudas. Friction Modeling and Compensation. In *The Control Handbook*, chapter Friction M. CRC Press, 1996.

[8] A. Badawy, F. Bolourchi, and S. Gaut. The Design and Benefits of Electric Power Steering. In *SAE Technical Paper: 973041*, 1997.

[9] M. Beecham. Global Market Review of Automotive Steering Systems - Forecasts to 2013: 2007 edition: The Market. Technical report, Aroq Limited, 2007.

[10] R. E. Bellman. *Dynamic Programming*. Courier Dover Publications, 2003.

[11] T. S. Buchanan, D. G. Lloyd, K. Manal, and T. F. Besier. Neuromusculoskeletal Modeling: Estimation of Muscle Forces and Joint Moments and Movements From Measurements of Neural Command. *Applied Biomechanics*, 20(4):367–395, 2004.

[12] R. Chabaan. Optimal control and gain scheduling of electrical power steering systems. *IEEE Vehicle Power and Propulsion Conference*, pages 53–59, 2009.

[13] R. Chabaan and L. Wang. Control of electrical power assist systems : H$_i nfty$ design, torque estimation and structural stability. *JSAE Review*, 22:435–444, 2001.

[14] R. C. Chabaan. *H_∞ Control Design and Gain Scheduling of Electrical Power Assist Steering Systems to Improve System Robustness and Stability*. PhD thesis, Wayne State University, Detroit, MI, United States, 2009.

[15] X. Chen, X. Chen, and K. Zhou. Optimal control for electrical power-assisted steering system. In *Control Applications Conference, 2005*, pages 1403–1408, 2005.

[16] X. Chen, T. Yang, X. Chen, and K. Zhou. A Generic Model-Based Advanced Control of Electric Power-Assisted Steering Systems. *Control Systems Technology, IEEE Transactions on*, 16(6):1289–1300, 2008.

[17] Z. Chen, Y. L. Yang, and L. H. Chen. Study on Boosting Curve for Electric Power Steering System Based on ADAMS. *Advanced Materials Research*, 97 - 101:3308–3313, 2010.

[18] C. Chitu, J. Lackner, M. Horn, P. S. Pullagura, H. Waser, and M. Kohlböck. Controller design for an electric power steering system based on LQR techniques. *COMPEL: The International Journal for Computation and Mathematics in Electrical and Electronic Engineering*, 32(3):763–775, 2013.

[19] S. Cholakkal and C. Xiang. Fault tolerant Control of Electric Power Steering using Kalman-Filter Simulation Study. In *Electro/Information Technology Conference*, pages 128–133, 2009.

[20] H. Chun-hua. Modeling and Simulation of Automotive Electric Power Steering System. In *Intelligent Information Technology Application Symposium, 2008*, volume 3, pages 436–439, 2008.

[21] D. Cole. Neuromuscular dynamics and steering feel. In *Proceedings of SteeringTech*, TU Munich, Germany, 2008.

[22] D. Cole. Steering Feedback Mathematical Simulation of Effects on Driver and Vehicle. *ATZautotechnology*, 8, 2008.

[23] D. Cole, A. Pick, and A. Odhams. Predictive and linear quadratic methods for potential application to modelling driver steering control. *Vehicle System Dynamics*, 44(3):259–284, 2006.

[24] P. Crago, J. Houk, and Z. Hasan. Regulatory actions of human stretch reflex. *Journal of neurophysiology*, 39(5):925–35, 1976.

[25] D. Crolla and D. Chen. Vehicle handling behaviour: subjective v. objective comparisons. In *Fisita 1998*, pages 1–15, 1998.

[26] R. Crowninshield and R. Brand. A physiologically based criterion of muscle force prediction in locomotion. *Journal of biomechanics*, 14(11):793–801, 1981.

[27] C. Dannöhl, S. Müller, and H. Ulbrich. H_∞-control of a rack-assisted electric power steering system. *Vehicle System Dynamics*, 50(4):527–544, 2012.

[28] D. Davy and M. Audu. A dynamic optimization technique for predicting muscle forces in the swing phase of gait. *Journal of biomechanics*, 20(2):187–201, 1987.

[29] E. de Vlugt. *Identification of spinal reflexes*. PhD thesis, Delft University of Technology, Delft, Netherlands, 2004.

[30] E. de Vlugt, A. C. Schouten, and C. T. van der Helm. Quantification of Intrinsic and Reflexive Properties During Multijoint Arm Posture. *Journal of Neuroscience Methods*, 155(2):328–349, 2006.

[31] L. Dong, P. Kandula, Z. Gao, D. Wang, D. Lili, G. Zhiqiang, and W. Dexin. On a Robust Control System Design for an Electric Power Assist Steering System. In *American Control Conference*, pages 5356–5361, 2010.

[32] J. Doyle. Guaranteed margins for LQG regulators. *IEEE Transactions on Automatic Control*, 23(4):756–757, 1978.

[33] Y. Du, M. Lion, and P. Maiß er. Modelling and control of an electromechanical steering system in full vehicle models. *Proceedings of the Institution of Mechanical Engineers, Part I: Journal of Systems and Control*, 220(3):1–11, 2006.

[34] A. El-Shaer, S. Sugita, and M. Tomizuka. Fixed-Structure Controller Design of Electric Power Steering Systems. In *American Control Conference*, volume 94720, pages 445–450, St. Louis, MO, USA, 2009.

[35] A. El-Shaer and M. Tomizuka. Robust multi-objective control for systems involving human-in-the-loop passivity constraints with application to electric power steering. In *2010 IEEE/ASME International Conference on Advanced Intelligent Mechatronics*, pages 361–366, Montreal, Canada, 2010.

[36] D. G. Farrer. An Objective Measurement Technique for the Quantification of On-Centre Handling Quality. In *International Congress and Exposition*, Detroit, MI, USA, 1993.

[37] A. G. Feldman and M. F. Levin. The origin and use of positional frames of reference in motor control. *Behavioral and brain sciences*, 18:723–806, 1995.

[38] G. Ferries and R. Arbanas. Control/Structure Interaction in Hydraulic Power Steering Systems. In *American Control Conference*, volume 2, pages 1146 –1151 vol.2, 1997.

[39] E. Fiala. Seitenkrafte am Rollenden Luftreifen. *Zeitschrift, V.D.I.*, 96(29):973–979, 1954.

[40] G. Forkenbrock and D. Elsasser. An Assessment of Human Driver Steering Capability. Technical Report number: DOT HS 809875, NHTSA, 2005.

[41] E. Forster, U. Simon, P. Augat, and L. Claes. Extension of a state-of-the-art optimization criterion to predict co-contraction. *Journal of biomechanics*, 37(4):577–581, 2004.

[42] J.-P. Gauthier, B. Berret, and F. Jean. A biomechanical inactivation principle. *Proceedings of the Steklov Institute of Mathematics*, 268(1):93–116, May 2010.

[43] R. Gopura, K. Kiguchi, and E. Horikawa. A study on human upper-limb muscles activities during daily upper-limb motions. *International Journal of Bioelectromagnetism*, 12(2):54–61, 2010.

[44] M. V. Groll, S. Mueller, T. Meister, and R. Tracht. Disturbance compensation with a torque controllable steering system. *Vehicle System Dynamics*, 44(4):327–338, 2006.

[45] A. Hall and J. McPhee. Automation of Adams/Car K&C Correlation using MATLAB. *SAE Technical Paper 2014-01-0847*, 2014.

[46] A. Hall, T. Uchida, F. Loh, C. Schmitke, and J. McPhee. Reduction of a Vehicle Multibody Dynamic Model Using Homotopy Optimization. *Archive of Mechanical Engineering*, 60(1):23–35, 2013.

[47] R. Happee. Inverse dynamic optimization including muscular dynamics, a new simulation method applied to goal directed movements. *Journal of Biomechanics*, 27(1):953–960, 1994.

[48] D. E. Hardt. Determining Muscle Forces in the Leg During Normal Human WalkingAn Application and Evaluation of Optimization Methods. *Journal of Biomechanical Engineering*, 100(2):72, 1978.

[49] Z. Hasan. A model of spindle afferent response to muscle stretch. *Journal of Neurophysiology*, 49(4):989–1006, 1983.

[50] R. Hayama, Y. Liu, X. Ji, and T. Mizuno. Preliminary Research on Muscle Activity in Drivers Steering Maneuver for Drivers Assistance System Evaluation. *Proceedings of the FISITA 2012 World Automotive Congress*, 195:723–735, 2013.

[51] A. Hill. The Heat of Shortening and the Dynamic Constants of Muscle. *Proceedings of the Royal Society of London. Series B, Biological Sciences*, 126(843):pp. 136—-195, 1938.

[52] M. Hooman and R. Kazemi. Simulation of Different Types of Electric Power Assisted Steering (EPS) to Investigate Applied Torque Positions' Effects. In *SAE 2003 World Congress and Exhibition, Session: Steering and Suspension Technology Symposium*, Detroit, MI, USA.

[53] W. Hoult and D. Cole. A neuromuscular model featuring co-activation for use in driver simulation. *Vehicle System Dynamics*, 46(sup1):175–189, 2008.

[54] R. E. Hughes, M. E. Johnson, S. W. O'Driscoll, and K. N. An. Age-related changes in normal isometric shoulder strength. *The American journal of sports medicine*, 27(5):651–7, 1999.

[55] A. Huxley. Muscle Contraction and theories of Contraction. *Progress in Biophysics and Biophysical Chemistry*, 7:255–318, 1957.

[56] K. Jalali. *Stability Control of Electric Vehicles with In-wheel Motors*. PhD thesis, University of Waterloo, Waterloo, Ontario, Canada, 2010.

[57] W. Jianwei and W. Minxiang. Study on Assist Coefficient and Disturbance Resistance for EPS. In *Measuring Technology and Mechatronics Automation Conference*, volume 2, pages 132–135, 2009.

[58] S. Jonsson and B. Jonsson. Function of the muscles of the upper limb in car driving. *Ergonomics*, 18(4):375–388, 1975.

[59] S. Jonsson and B. Jonsson. Function of the muscles of the upper limb in car driving. IV: the pectoralis major, serratus anterior and latissimus dorsi muscles. *Ergonomics*, 18(6):643–649, 1975.

[60] S. Jonsson and B. Jonsson. Function of the muscles of the upper limb in car driving. V: The supraspinatus, infraspinatus, teres minor and teres major muscles. *Ergonomics*, 19(6):711–717, 1976.

[61] G. Kamen and G. E. Caldwell. Physiology and interpretation of the electromyogram. *Journal of clinical neurophysiology : official publication of the American Electroencephalographic Society*, 13:366–384, 1996.

[62] M. L. Kaplan and J. H. Heegaard. Predictive algorithms for neuromuscular control of human locomotion. *Journal of Biomechanics*, 34:1077–1083, 2001.

[63] S. Keen and D. Cole. Steering control using model predictive control and multiple internal models. In *Advanced Vehicle and Control Conference (AVEC)*, Taipei, Taiwan, 2006.

[64] S. Keen and D. Cole. Application of time-variant predictive control to modelling driver steering skill. *Vehicle System Dynamics*, 49(4):527–559, 2011.

[65] N. Kim and D. Cole. A model of driver steering control incorporating the driver's sensing of steering torque. *Vehicle System Dynamics*, 49(10):1575–1596, 2011.

[66] D. E. Kirk. *Optimal Control Theory - an Introduction*. Prentice-Hall, Inc., New York, 1971.

[67] J. Klötzl. Concept, construction and first results of a test bench for automotive power nets. In *Stuttgart International Symposium*, 2011.

[68] J. Knapczyk and M. Maniowski. Stiffness Synthesis of a Five-Rod Suspension for Given Load-Displacement Characteristics. *Proceedings of the Institution of Mechanical Engineers, Part D: Journal of Automobile Engineering*, 220(7):879–889, 2006.

[69] M. Kondo. Directional Stability (when Steering is added). *Journal of the Society of Automotive Engineers of Japan (JSAE)*, 7:5–6, 1953.

[70] M. Kondo and A. Ajimine. Drivers Sight Point and Dynamics of the Driver-Vehicle-System Related to It. In *SAE Technical Paper, Paper Number: 680104*, 1968.

[71] F. Lacquaniti and J. Soechting. Behavior of the stretch reflex in a multi-jointed limb. *Brain research*, 311(1):161–6, 1984.

[72] D. Lametti, G. Houle, and D. Ostry. Control of movement variability and the regulation of limb impedance. *Journal of neurophysiology*, 98:3516–3524, 2007.

[73] M. Lawson and X. Chen. Hardware-in-the-Loop Simulation of Fault Tolerant Control for an Electric Power Steering System. In *Vehicle Power and Propulsion Conference*, pages 1–6, 2008.

[74] M. H. Lee, S. K. Ha, J. Y. Choi, and K. S. Yoon. Improvement of The Steering Feel of an Electric Power Steering System by Torque Map Modification. *Journal of Mechanical Science and Technology*, 19(3):792–801, 2005.

[75] L. Li, L. He, J. Du, and T. Lin. An Electric Power Steering System Controller based on Disturbance Observer. In *IEEE International Conference on Integration Technology*, pages 446–449, Shenzhen, China, 2007. Ieee.

[76] X. Li, X.-P. Zhao, and J. Chen. Sliding mode control for torque ripple reduction of an electric power steering system based on a reference model. *Proceedings of the Institution of Mechanical Engineers, Part D: Journal of Automobile Engineering*, 222(12):2283–2290, 2008.

[77] Y. G. Liao and H. I. Du. Cosimulation of Multi-Body-Based Vehicle Dynamics and an Electric Power Steering Control System. *Proceedings of the Institution of Mechanical Engineers, Part K: Journal of Multi-body Dynamics*, 215(3):141–151, 2001.

[78] C. F. Lin. *Advanced Control System Design*. Prentice-Hall, Inc., Upper Saddle River, NJ, USA, 1994.

[79] T. Lin and J. Arora. Differential dynamic programming technique for constrained optimal control. *Computational Mechanics*, pages 27–40, 1991.

[80] Y. Liu, X. Ji, H. Ryouhei, M. Takahiro, and L. Lou. Function of shoulder muscles of driver in vehicle steering maneuver. *Science China Technological Sciences*, 55(12):3445–3454, 2012.

[81] Z. Liu, J. Yang, and D. Liao. The Optimization of Electric Power Assisted Steering to Improve Vehicle Performance. *Proceedings of the Institution of Mechanical Engineers, Part D: Journal of Automobile Engineering*, 217(8):639–646, 2003.

[82] R. Maas, T. Siebert, and S. Leyendecker. On the relevance of structure preservation to simulations of muscle actuated movements. *Biomechanics and modeling in mechanobiology*, 11(3-4):543–56, 2012.

[83] C. MacAdam. Application of an optimal preview control for simulation of closed-loop automobile driving. *IEEE Transactions on Systems, Man and Cybernetics*, 11(6):393–399, 1981.

[84] C. C. Macadam. Understanding and Modeling the Human Driver. *Vehicle System Dynamics*, 40(1-3):101–134, 2003.

[85] A. Marouf, M. Djemai, C. Sentouh, and P. Pudlo. Driver Torque and Road Reaction Force Estimation of an Electric Power Assisted Steering using Sliding Mode Observer with Unknown Inputs. In *Intelligent Transportation Systems Conference (ITSC)*, pages 354–359, 2010.

[86] C. Marsden, P. Merton, and H. Morton. Stretch reflex and servo action in a variety of human muscles. *The Journal of physiology*, 259:531–560, 1976.

[87] S. D. J. Matthew. *Active Roll Control of Articulated Heavy Vehicles*. PhD thesis, University of Cambridge, Cambridge, United Kingdom, 2000.

[88] P. Matthews. The human stretch reflex and the motor cortex. *Trends in neurosciences*, pages 87–91, 1991.

[89] N. Mehrabi and J. McPhee. Evaluation of a Musculoskeletal Arm Model for Automobile Drivers using Electromyography. In *7th World Congress of Biomechanics*, Boston, MA, 2014.

[90] N. Mehrabi and J. McPhee. Steering feel improvement for different driver types using model-based control. In *Proceedings of the ASME 2014 International Design Engineering Technical Conferences*, Buffelo, USA, 2014.

[91] N. Mehrabi, J. McPhee, and N. L. Azad. Optimal Disturbance Rejection Control Design for Electric Power Steering Systems. In *50th IEEE Conference on Decision and Control and European Control Conference*, pages 6584–6589, 2011.

[92] N. Mehrabi, R. Sharif Razavian, and J. McPhee. A three-dimentional musculoskeletal driver model to study steering tasks. In *ASME 2013 International Design Engineering Technical Conference & Computers and Information in Engineering Conferences*, 2013.

[93] N. Mehrabi, R. Sharif Razavian, and J. McPhee. A Physics-based Driver Model with Application to Steering Disturbance Rejection. *Submitted to Vehicle System Dynamics*, 2014.

[94] N. Mehrabi, M. Sharif Shourijeh, and J. McPhee. Study of Human Steering Tasks using a Neuromuscular Driver Model. *Advanced Vehicle and Control Conference*, 2012.

[95] M. P. Mileusnic, I. E. Brown, N. Lan, and G. E. Loeb. Mathematical models of proprioceptors. I. Control and transduction in the muscle spindle. *Journal of neurophysiology*, 96(4):1772–88, 2006.

[96] T. Milner. Adaptation to destabilizing dynamics by means of muscle cocontraction. *Experimental brain research. Experimentelle Hirnforschung. Expérimentation cérébrale*, 143(4):406–16, 2002.

[97] T. Milner and C. Cloutier. The effect of antagonist muscle co-contraction on damping of the wrist joint during voluntary movement. *Proceedings of 17th International Conference of the Engineering in Medicine and Biology Society*, 2, 1995.

[98] T. Mizuno, R. Hayama, S. KAWAHARA, L. Lou, Y. Liu, and X. Ji. Research on Relationship between Steering Maneuver and muscle activities. *eb-cat.ds-navi.co.jp*, (1010):13–18, 2013.

[99] Y. Morita, K. Torii, N. Tsuchida, M. Iwasaki, H. Ukai, N. Matsui, T. Hayashi, N. Ido, and H. Ishikawa. Improvement of Steering Feel of Electric Power Steering System with Variable Gear Transmission System using Decoupling Control. In *Advanced Motion Control Conference*, pages 417–422, 2008.

[100] Y. Morita, K. Torii, N. Tsuchida, H. Ukai, M. Iwasaki, N. Matsui, J. Hayashi, N. Ido, and H. Ishikawa. Decoupling Control of Electric Power Steering System with Variable Gear Transmission System. In *IEEE Industrial Electronics Conference*, pages 5264–5269, 2006.

[101] Y. Morita, A. Yokoi, M. Iwasaki, H. Ukai, N. Matsui, N. Ito, N. Uryu, and Y. Mukai. Controller Design Method for Electric Power Steering System with Variable Gear Transmission System using Decoupling Control. In *Industrial Electronics Conference*, pages 3065–3070, 2009.

[102] MSC ADAMS Online Help. MSC Software, http://www.mscsoftware.com, 2011.

[103] A. Nagano and K. Gerritsen. Effects of Neuromuscular Strength Training on Vertical Jumping Performance A Computer Simulation Study. *Journal of Applied Biomechanics*, 17:113–128, 2001.

[104] R. Neptune. Optimization algorithm performance in determining optimal controls in human movement analyses. *Journal of biomechanical engineering*, 121:249–252, 1999.

[105] R. Neptune and M. Hull. Evaluation of performance criteria for simulation of submaximal steady-state cycling using a forward dynamic model. *Journal of biomechanical engineering*, 120:334–341, 1998.

[106] NEWYORK(CNNMoney). No defect found in {Toyota Corolla} Steering. *http://money.cnn.com/2011/05/24/autos/nhtsa corolla investigation closed/index.htm*, May 2011.

[107] K. Norman. Objective Evaluation of On-Center Handling Performance. In *SAE Technical Paper, Paper Number: 840069*, 1984.

[108] M. Parmar and J. Hung. A Sensorless Optimal Control System for an Automotive Electric Power Assist Steering System. *IEEE Transactions on Industrial Electronics*, 51(2):290–298, 2004.

[109] S. Peilin, G. Shixiang, M. Lidong, W. Hongmin, P. Shi, S. Gao, L. Miao, and H. Wang. Optimal Controller Design for Electric Power Steering System Based on LQG. In *Information Engineering and Computer Science Conference*, pages 1–4. Ieee, 2009.

[110] H. Peng and M. Tomizukoa. Automation, Preview control for vehicle lateral guidance in highway. *Journal of Dynamic Systems, Measurement, and Control*, 115:679–686, 1993.

[111] E. Pennestri, R. Stefanelli, P. P. Valentini, L. Vita, and E. Pennestrì. Virtual musculo-skeletal model for the biomechanical analysis of the upper limb. *Journal of biomechanics*, 40(6):1350–61, 2007.

[112] A. Pick. *Neuromuscular dynamics and the vehicle steering task*. Phd, University of Cambridge, Cambridge, United Kingdom, 2004.

[113] A. Pick and D. Cole. Neuromuscular dynamics and the vehicle steering task. In *The 18th International Association for Vehicle System Dynamics Symposium*, number October, Kanagawa, Japan, 2003.

[114] A. Pick and D. Cole. Measurement of Driver Steering Torque Using Electromyography. *Journal of Dynamic Systems, Measurement, and Control*, 128(4):960, 2006.

[115] A. Pick and D. Cole. Neuromuscular dynamics in the driver-vehicle system. *Vehicle System Dynamics: International Journal of Vehicle Mechanics and Mobility*, 44(sup1):624–631, 2006.

[116] A. Pick and D. Cole. Driver steering and muscle activity during a lane-change manoeuvre. *Vehicle System Dynamics*, 45(9):781–805, 2007.

[117] A. Pick and D. Cole. Dynamic properties of a driver's arms holding a steering wheel. *Proceedings of the Institution of Mechanical Engineers, Part D: Journal of Automobile Engineering*, 221(12):1475–1486, 2007.

[118] A. Pick and D. Cole. A mathematical model of driver steering control including neuromuscular dynamics. *Journal of Dynamic Systems, Measurement, and Control*, 130(3):031004, 2008.

[119] J. W. Rankin and R. R. Neptune. Musculotendon lengths and moment arms for a three-dimensional upper-extremity model. *Journal of Biomechanics*, 45(9):1739–1744, 2012.

[120] H. Röhrle, R. Scholten, and C. Sigolotto. Joint forces in the human pelvis-leg skeleton during walking. *Journal of Biomchanics*, 17(6):409–424, 1984.

[121] M. Rothhämel, J. IJkema, and L. Drugge. A method to find correlations between steering feel and vehicle handling properties using a moving base driving simulator. *Vehicle System Dynamics*, 49(12):1837–1854, 2011.

[122] M. Rothhämel, J. IJkema, and L. Drugge. Finding correlation between steering feel assessments and the driver's performance using a moving base driving simulator. *FAST-zero'11*, pages 1–6, 2011.

[123] M. Rothhämel, J. IJkema, and L. Drugge. Influencing driver chosen cornering speed by means of modified steering feel. *Vehicle System Dynamics*, 00:1–16, 2013.

[124] D. Sampson, D. Cebon, and T. St. Active Roll Control of Single Unit Heavy Road Vehicles. *Vehicle System Dynamics: International Journal of Vehicle Mechanics and Mobility*, 40(4), 2003.

[125] J. Schuppen, M. Thoma, M. Krstic, B. Brogliato, H. S. Chang, M. Fu, J. Hu, and S. Marcus. Nonlinear Model Predictive Control, Theory and Algorithms. pages 43–66, 2011.

[126] M. Seron. Receding horizon control, Course notes, University of Newcastle, Australia, 2004.

[127] M. Sharif Shourijeh. *Optimal Control and Multibody Dynamic Modelling of Human Musculoskeletal Systems*. PhD thesis, University of Waterloo, Waterloo, Ontario, 2013.

[128] M. Sharif Shourijeh and J. McPhee. Optimal Control and Forward Dynamics of Human Periodic Motions Using Fourier Series for Muscle Excitation Patterns. *Journal of Computational and Nonlinear Dynamics*, 9(2):21005, 2013.

[129] M. Sharif Shourijeh, N. Mehrabi, and J. McPhee. Using Static Optimization in Forward Dynamic Simulation of Human Musculoskeletal Systems. *Submitted to Computer methods in biomechanics and biomedical engineering*, 0(0):1–9, 2014.

[130] R. Sharp, P. Symonds, and D. Casanova. A Mathematical Model for Driver Steering Control, with Design, Tuning and Performance Results. *Vehicle System Dynamics*, 33(5):289–326, 2000.

[131] R. Sharp and V. Valtetsiotis. Optimal preview car steering control. *Selected papers from 20th International Congress of Theoretical and Applied Mechanics, Supplement to Vehicle System Dynamics*, 35:101–117, 2001.

[132] M. C. Shin, S. H. Kim, G. H. Cho, and C. N. Chu. Development of a steering-system model considering viscous friction and its verification. *Proceedings of the Institution of Mechanical Engineers, Part D: Journal of Automobile Engineering*, 0(0):1–20, 2013.

[133] A. Skrzek, Z. Ignasiak, and S. Kozie. Differences in muscle strength depend on age, gender and muscle functions. *Isokinetics and Exercise Sciences*, 20:229–235, 2012.

[134] K. Tahara, S. Arimoto, M. Sekimoto, and Z.-W. Luo. On control of reaching movements for musculo-skeletal redundant arm model. *Applied Bionics and Biomechanics*, 6(1):11–26, 2009.

[135] K. Tahara, Z.-W. Luo, S. Arimoto, and H. Kino. Sensory-motor control mechanism for reaching movements of a redundant musculo-skeletal arm. *Journal of Robotic Systems*, 22(11):639–651, 2005.

[136] T. Tamura, A. Maroonian, and R. Fuchs. Active Compensation of Friction in Electric Power Steering. In *Proceedings of the FISITA 2012 World Automotive Congress*, volume 198 of *Lecture Notes in Electrical Engineering*, pages 213–225. Springer Berlin Heidelberg, 2013.

[137] T. Tamura, A. Maroonian, M. Higashi, and R. Fuchs. Modeling and Simulation for Dynamic Analysis of Column Type Electric Power Steering. *JTEKT Engineering Journal*, (1010E):19–25, 2013.

[138] D. Thelen and F. Anderson. Using computed muscle control to generate forward dynamic simulations of human walking from experimental data. *Journal of biomechanics*, 39(6):1107–1115, 2006.

[139] D. Thelen, F. Anderson, and S. Delp. Generating dynamic simulations of movement using computed muscle control. *Journal of Biomechanics*, 36(3):321–328, 2003.

[140] D. Tian, G. Yin, G. Xie, T. Daqing, Y. Guofu, and X. Gang. Model and H_$infty$ Robust Control Design for Electric Power Steering System. In *Intelligent Mechatronics and Automation Conference*, pages 779–783, 2004.

[141] L. Ting, K. van Antwerp, J. Scrivens, L. McKay, T. Welch, J. Bingham, and S. DeWeerth. Neuromechanical tuning of nonlinear postural control dynamics. *Chaos (Woodbury, N.Y.)*, 19(2):26111, 2009.

[142] E. Todorov. Direct cortical control of muscle activation in voluntary arm movements: a model. *Nature neuroscience*, 3(4):391–8, 2000.

[143] K. Tsuji, K. Kataoka, Y. Kusaka, T. Teratani, and T. Abe. EPS System Analysis using Multi Domain Simulation for Power Network Design in a Vehicle. *2007 Power Conversion Conference - Nagoya*, pages 1340–1345, 2007.

[144] B. R. Umberger, K. G. M. Gerritsen, and P. E. Martin. A Model of Human Muscle Energy Expenditure. *Computer Methods in Biomechanics and Biomedical Engineering*, 9(5):342, 2006.

[145] A. Ungoren and H. Peng. An adaptive lateral preview driver model. *Vehicle System Dynamics*, 43(4):245–259, 2005.

[146] B. Van Bolhuis and C. Gielen. A comparison of models explaining muscle activation patterns for isometric contractions. *Biological cybernetics*, 81(3):249–61, 1999.

[147] F. van der Helm, A. Schouten, E. de Vlugt, and G. Brouwn. Identification of Intrinsic and Reflexive Components of Human Arm Dynamics During Postural Control. *Journal of Neuroscience Methods*, 119(1):1–14, 2002.

[148] A. van Soest, M. Bobbert, T. Iijima, K. Shimizu, and N. Asanuma. The Contribution of Muscle Properise in the Control of Explosive Movments. *Biological Cybernetics*, 69:195–204, 1993.

[149] S. Wang, C. Yin, J. Zhao, W. Shaohua, Y. Chunfang, and Z. Jinbo. Design and Full-Vehicle Tests of EPS Control System. In *Computer Science-Technology and Applications Conference*, volume 2, pages 101–104. Ieee, 2009.

[150] D. Weir and D. McRuer. Dynamics of driver vehicle steering control. *Automatica*, 6:87–98, 1970.

[151] D. Wilkie. The mechanical properties of muscle. *British medical bulletin*, 12:177–182, 1956.

[152] J. Winters and L. Stark. Analysis of fundamental human movement patterns through the use of in-depth antagonistic muscle models. *IEEE transactions on bio-medical engineering*, 32:826–839, 1985.

[153] J. Winters and L. Stark. Muscle models: what is gained and what is lost by varying model complexity. *Biological cybernetics*, 55:403–420, 1987.

[154] J. Winters and L. Stark. Estimated mechanical properties of synergistic muscles involved in movements of a variety of human joints. *Journal of biomechanics*, 21:1027–1041, 1988.

[155] J. Y. Wong. *Theory of Ground Vehicles*. John Wiley & Sons, 2001.

[156] G. Wu, F. C. van der Helm, H. (DirkJan) Veeger, M. Makhsous, P. Van Roy, C. Anglin, J. Nagels, A. R. Karduna, K. McQuade, X. Wang, F. W. Werner, and B. Buchholz. ISB recommendation on definitions of joint coordinate systems of various joints for the reporting of human joint motion - Part II: shoulder, elbow, wrist and hand. *Journal of Biomechanics*, 38(5):981–992, 2005.

[157] Z. Xue-Ping, L. Xin, C. Jie, and M. Jin-Lai. Parametric Design and Application of Steering Characteristic Curve in Control for Electric Power Steering. *Mechatronics*, 19(6):905–911, 2009.

[158] G. T. Yamaguchi, D. W. Moran, and J. Sit. a computationally efficient method for solving the redundant problem in biomechanics. *Journal of Biomchanics*, 28(8):999–1005, 1995.

[159] G. T. Yamaguchi and F. E. Zajac. Restoring unassisted natural gait to paraplegics via functional neuromuscular stimulation: a computer simulation study. *IEEE transactions on bio-medical engineering*, 37:886–902, 1990.

[160] N. Yuhara, S. Horiuchi, T. Iijima, K. Shimizu, and N. Asanuma. An Advanced Steering System with Active Kinesthetic Feedback for Handling Qualities Improvement. *Vehicle System Dynamics*, 27(5-6):327–355, 1997.

[161] F. Zajac. Muscle and Tendon: Properties, Models, Scaling, and Application to Biomechanics and Motor Control. *CRC Critical Reviews in Biomedical Engineering*, 19(4):359–411, 1989.

[162] J. Zakotnik, T. Matheson, and V. Dürr. Co-contraction and passive forces facilitate load compensation of aimed limb movements. *The Journal of neuroscience: the official journal of the Society for Neuroscience*, 26:4995–5007, 2006.

[163] A. Zaremba and R. Davis. Dynamic Analysis and Stability of a Power assist Steering System. In *American Control Conference*, volume 6, pages 4253–4257, 1995.

[164] Q. Zeng and J. Huang. The Development of Control Unit in Automotive Electric Power Steering System. In *Information Processing Conference*, volume 1, pages 242–245, 2009.

[165] W. Zhao, G. Shi, and Y. Lin. Study on mixed H_∞/H_2 control for enhancing the tracking performance of EPS. In *IEEE International Conference on Automation and Logistics*, pages 628–633, Jinan, China, 2007.

[166] W. Zhao and C. Wang. Mixed H_2/H_∞ Road Feel Control of EPS based on Genetic Algorithm. *SCIENCE CHINA Technological Sciences*, pages 1–9, 2010.

[167] X. Zhao, X. Shi, J. Chen, and X. Li. Dynamic correction of the steering-characteristic curve and application to an EPS control system. *International journal of automotive technology*, 12(2):243–249, 2011.

[168] B. Zhou, S. Y. Bei, and J. B. Zhao. Computer-Aided Design of Curved Assistance Characteristic of EPS System. *Applied Mechanics and Materials Conference*, 39:598–601, 2010.

[169] A. K. Zschocke and A. Albers. Links between subjective and objective evaluations regarding the steering character of automobiles. *International Journal of Automotive Technology*, 9:473–481, 2008.

APPENDICES

A

State-Space Formulation of Control-Oriented Model

To construct the state-space representation of the control-oriented model (see Fig. 3.5), the state variables are defined as $\boldsymbol{x} = \begin{bmatrix} \beta & i & \omega_z & \theta_r & \dot{\theta}_r & \theta_{sw} & \dot{\theta}_{sw} \end{bmatrix}^T$, and the inputs to the EPS system are defined as driver torque (u_τ), terminal voltage of electric motor (u_v) and disturbance torque (u_d) at the intermediate shaft (pinion). The state space equations of the system can be described by,

$$\begin{aligned} \dot{\boldsymbol{x}} &= A\boldsymbol{x} + B_v u_v + B_\tau u_\tau + B_d u_d \\ \boldsymbol{y} &= C\boldsymbol{x} = \begin{bmatrix} T_{tb} & \theta_{sw} & i & \dot{\theta}_m & a_y & r \end{bmatrix} \end{aligned} \tag{A.1}$$

where A, B_v, B_τ, B_d and C are the system, input and output matrices of the system. Here, it is assumed that the torque sensor value, steering wheel angle, motor current, angular velocity of motor shaft, yaw rate and lateral acceleration of vehicle are measurable and included in the output $\mathbf{y}$.

By rewriting the differential equations (3.12 - 3.15) into the state-space matrix format, the system matrix (A) can be desribed by Eq. (A.4), and input matrices can be described as follow:

$$B_\tau = \begin{bmatrix} 0 \\ 0 \\ 0 \\ 0 \\ 0 \\ 0 \\ {J_{sw}}^{-1} \end{bmatrix}, B_{uv} = \begin{bmatrix} 0 \\ L^{-1} \\ 0 \\ 0 \\ 0 \\ 0 \\ 0 \end{bmatrix}, B_{rf} = \begin{bmatrix} 0 \\ 0 \\ 0 \\ 0 \\ {J_r}^{-1} \\ 0 \\ 0 \end{bmatrix} \tag{A.2}$$

where the input matrices related to driver torque, friction force, and terminal voltage are B_τ, B_{rf}, and B_{uv}, respectively. The output matrices C and D can be described by:

$$C = \begin{bmatrix} 0 & 0 & 0 & -K_{tb} & 0 & K_{tb} & 0 \\ 0 & 0 & 0 & 0 & 0 & 1 & 0 \\ 0 & 0 & 0 & 0 & G & 0 & 0 \\ 0 & 1 & 0 & 0 & 0 & 0 & 0 \\ 0 & 0 & 1 & 0 & 0 & 0 & 0 \\ -\frac{(C_{\alpha f}+C_{\alpha r})}{m} & 0 & -\frac{(C_{\alpha f}L_f - C_{\alpha r}L_r)}{mV_x} & \frac{C_{\alpha f}}{G_{steering}m} & 0 & 0 & 0 \end{bmatrix}, D = \begin{bmatrix} 0 \end{bmatrix} \tag{A.3}$$

$$A = \begin{bmatrix} -\frac{C_{\alpha f}+C_{\alpha r}}{m v_x} & 0 & -\left(m v_x + \frac{C_{\alpha f}\, L_f}{v_x} - \frac{C_{\alpha r}\, L_r}{v_x}\right) m^{-1} {v_x}^{-1} & \frac{C_{\alpha f}}{G_{steering}\, m v_x} \\ 0 & -\frac{R}{L} & 0 & 0 \\ -\frac{C_{\alpha f}\, L_f - C_{\alpha r}\, L_r}{I_{zz}} & 0 & -\left(\frac{{L_f}^2 C_{\alpha f}}{v_x} + \frac{{L_r}^2 C_{\alpha r}}{v_x}\right) {I_{zz}}^{-1} & \frac{C_{\alpha f}\, L_f}{G_{steering}\, I_{zz}} \\ 0 & 0 & 0 & 0 \\ -\frac{C_T}{J_r} & \frac{Ke\, G}{J_r} & -\frac{C_T\, L_f}{v_x\, J_r} & -\left(K_{tb} + r_p\, Kr - \frac{C_T}{G_{steering}}\right) {J_r}^{-1} \\ 0 & 0 & 0 & 0 \\ 0 & 0 & 0 & \frac{K_{tb}}{J_{sw}} \end{bmatrix}$$

$$\begin{bmatrix} -\frac{Ke\, G}{L} & 0 & 0 \\ 0 & 0 & 0 \\ 1 & 0 & 0 \\ -\frac{Cr\, r_p + Cc + C_T\, b}{J_r} & \frac{K_{tb}}{J_r} & \frac{C_T\, b}{J_r} \\ 0 & 0 & 1 \\ \frac{C_T\, b}{J_{sw}} & -\frac{K_{tb}}{J_{sw}} & -\frac{Csw + C_T\, b}{J_{sw}} \end{bmatrix} \tag{A.4}$$

B

Upper Extremity Muscle Path Parameters

In this thesis, the upper extremity model of driver including torso, humerus, forearm and hand holding a steering wheel is developed in MapleSim. The muscle path parameters used in the 3D musculoskeletal arm model are adopted from the published research articles [111, 43, 159, 139], and are summarized in Table B.1. The muscle origin and insertion coordinates are given with respect to the local reference frames as shown in Figure 4.1b.

Table B.1: List of muscle origin/insertion points used in the 3D arm model

#	muscle	max iso. force (N)	first connection (origin)**	coordinate (mm)			second connection (insertion)**	coordinates (mm)		
				x	y	z		x	y	z
1	Coracobrachialis (CORB)	63	torso	20	30	35	humerus	174	21	0
2	Deltoid (DELT1)*	240	torso	-30	40	15	humerus	106	-24	-11
3	Deltoid (DELT2)*	200	torso	-9	64	25	humerus	119	-9	9
4	Deltoid (DELT3)*	200	torso	-45	35	-10	humerus	95	-9	9
5	Latissimus dorsi (LAT)	360	torso	-35	90	-125	humerus	50	0	-13
6	Pectoralis major (PECM)	210	torso	45	95	-125	humerus	-14	1	2
7	Supraspinatus (SUPSP)	98	torso	-20	90	35	humerus	-14	17	27
8	Biceps brachii (BICshort)	47	torso	0	0	15	ulna	38	0	10
9	Biceps brachii (BIClong)	90	torso	0	15	10	ulna	38	0	10
10	Infraspinatus (INFRA)*	210	torso	-15	80	-40	humerus	28	-19	27
11	Anconeus (ANC)*	40	humerus	265	5	-19	humerus	42	12	-29
12	Triceps brachii (TRIlong)*	135	torso	-25	20	-20	radius	38	27	-20
13	Triceps brachii (TRImed)*	108	humerus	78	11	-10	ulna	38	27	-20
14	Brachialis (BRA)	167	humerus	176	-8	16	radius	33	5	10
15	Brachioradialis (BRD)	45	humerus	246	-27	0	radius	283	-12	0

* These muscles consider via-points to preserve the muscle path and functionality

** Coordinates given with respect to the local reference frames in Figure 4.1b.